universität wien

DISSERTATION / DOCTORAL THESIS

Titel der Dissertation /Title of the Doctoral Thesis

„Probing the Strong Interaction with Kaonic Atom X-Ray Measurements at Low Energies“

verfasst von / submitted by

Marlene Tüchler, BSc MSc

angestrebter akademischer Grad / in partial fulfilment of the requirements for the degree of

Doktorin der Naturwissenschaften (Dr. rer. nat.)

Wien, 2023 / Vienna 2023

Studienkennzahl lt. Studienblatt / degree programme code as it appears on the student record sheet:	UA 796 605 411
Dissertationsgebiet lt. Studienblatt / field of study as it appears on the student record sheet:	Physik
Betreut von / Supervisor:	Hon.-Prof. Dipl.-Phys. Dr. Eberhard Widmann Privatdoz. Dr. Johann Zmeskal

This work is dedicated to everyone living with chronic illness.

Abstract

The antikaon-nucleon interaction in the low-energy regime of quantum chromodynamics is, to this day, not fully understood and experimental input is needed to constrain the theoretical descriptions. Kaonic atoms provide an ideal system to study this interaction at zero relative energy. The strong interaction between the kaon and nucleons induces an energy shift and broadening of the width of the low-n states in the kaonic atom, which can be directly measured via X-ray spectroscopy. The goal of the SIDDHARTA-2 experiment, located at the DAΦNE collider complex at LNF in Italy, is the measurement of the $(2p \rightarrow 1s)$ X-ray transition in kaonic deuterium.
In 2021, the experiment successfully performed its commissioning with a reduced setup called SIDDHARTINO. The aim of this commissioning phase were the characterisation of the background, the optimisation of the setup, and performance studies of the X-ray detectors, all of which are presented in this work. It concluded with a successful revised measurement of kaonic helium-4, which continued after the installation of the complete SIDDHARTA-2 setup, now including the full X-ray detection system and veto systems for active background suppression. This work presents the analysis of the kaonic helium-4 data obtained with SIDDHARTINO and SIDDHARTA-2, including a detailed analysis of the performance of the X-ray detectors and veto systems. The $(3d \rightarrow 2p)$ transition in kaonic helium-4 was again measured with a statistical precision below 1 eV, with a transition energy of $(6463.44 \pm 0.95 \pm 2.00)$ eV, a $2p$ level shift of $(0.44 \pm 0.95 \pm 2.00)$ eV, and a $2p$ width of (0.6 ± 10.1) eV. This provides the most precise result for kaonic ^{4}He obtained with silicon drift detectors; only the measurement performed by the E62 collaboration using superconducting microcalorimeters achieved a higher precision. Moreover, several transitions from higher levels in intermediate-mass kaonic atoms produced in the solid structures of the setup were measured for the first time. The energies of transitions in kaonic carbon, kaonic nitrogen, kaonic oxygen, and kaonic aluminium are reported in this work. The initial beam time of SIDDHARTA-2 was completed with a first run with a deuterium target. The preliminary analysis of this data and the resulting X-ray spectrum obtained with the deuterium target are presented.

Zusammenfassung

Die Antikaon-Nukleon-Interaktion der niederenergetischen Quantenchromodynamik ist bis heute nicht vollständig verstanden und experimentelle Daten sind notwendig, um die theoretischen Beschreibungen einzuschränken. Kaonische Atome bieten ein ideales System, um diese Wechselwirkung bei verschwindender relativer Energie zu studieren. Die starke Wechselwirkung zwischen dem Kaon und den Nukleonen führt zu einer Energieverschiebung und Verbreiterung der Zustände mit niedrigem n im kaonischen Atom, die durch Röntgenspektroskopie direkt gemessen werden können. Das Ziel des SIDDHARTA-2-Experiments, welches sich in dem Beschleunigerkomplex DAΦNE in Frascati, Italien, befindet, ist die Messung des $(2p \rightarrow 1s)$-Röntgenübergangs in kaonischem Deuterium.
In 2021 führte das Experiment seine Kommissionierung mit einem reduzierten Aufbau, genannt SIDDHARTINO, durch. Der Zweck dieser Phase waren die Charakterisierung des Hintergrunds, die Optimierung des Aufbaus, sowie die Untersuchung des Verhaltens der Röntgendetektoren, welche in dieser Arbeit beschrieben werden. Die Kommissionierung endete mit einer erfolgreichen erneuten Messung von kaonischem Helium-4, welche nach der Installation des vollständigen SIDDHARTA-2-Aufbaus fortgeführt wurde. Der Aufbau beinhaltete nun das komplette Röntgendetektionssystem und Veto-Systeme zur aktiven Unterdrückung von Untergrund. In dieser Arbeit wird die Analyse der mit SIDDHARTINO und SIDDHARTA-2 gesammelten Daten zu kaonischem Helium-4, inklusive einer detaillierten Analyse des Verhaltens der Röntgendetektoren und Veto-Systeme, präsentiert. Der $(3d \rightarrow 2p)$-Röntgenübergang in kaonischem Helium-4 wurde mit einer statistischen Unsicherheit von weniger als 1 eV gemessen, mit einer Übergangsenergie von $(6463.44 \pm 0.95 \pm 2.00)$ eV, einer Energieverschiebung des $2p$-Levels von $(0.44 \pm 0.95 \pm 2.00)$ eV, und einer $2p$-Breite von (0.6 ± 10.1) eV. Dieses Resultat repräsentiert die präziseste Messung von kaonischem ^{4}He, die mit Siliziumdriftdetektoren erreicht wurde; nur die Messung der E62-Kollaboration mit supraleitenden Mikrokalorimetern erzielte eine höhere Präzision. Außerdem wurden mehrere Übergänge aus höheren Levels in mittelschweren kaonischen Atomen, welche in den festen Strukturen des Aufbaus produziert wurden, zum ersten Mal gemessen. Die Energien von Übergängen in kaonischem Kohlenstoff, kaonischem Stickstoff, kaonischem Sauerstoff, und kaonischem Aluminium werden in dieser Arbeit präsentiert. Die erste SIDDHARTA-2-Strahlzeit wurde mit einer erstmaligen Messung mit einem Deuterium-Target beendet. Diese Arbeit gibt einen Einblick in die vorläufige Analyse der Daten zu kaonischem Deuterium und dem sich daraus ergebenden Spektrum.

Acknowledgements

First of all, I would like to thank my supervisors. My sincere appreciation goes to Eberhard Widmann for his guidance, support and advice during the last years. I would like to express my heartfelt gratitude to Hannes. His guidance, mentorship, trust and support - in research, but also beyond the scope of the lab -, were invaluable and crucial for the success of this work and will never be taken for granted.

Furthermore, I want to express my gratitude towards my mentor Catalina, who always provided me with guidance, empowerment, support and a role model.

My gratitude also extends to the DK-PI for its financial, advisory and communal support. In particular, I would like to express my gratitude towards my mentor Jochen Schieck.

I would also like to thank the exceptional team at SMI. Thank you to all my colleagues - I want to especially mention Doris, Julia, Fiona, Leo and Herbert. Moreover, I would like to thank my fellow students and PDs for making this time the best it could ever have been.

In addition, I want to thank the collaboration team of SIDDHARTA-2 for their teamwork and support. My colleagues welcomed me warmly every time and I hold the time I spent in Frascati dear to my heart.

I could not write my acknowledgements without mentioning my incredible group of friends. I know for a fact that I could not have finished my doctorate without the support of Sigrid, Carina, Vici, Constanze and Priya. Thank you for celebrating with me, fighting with me, providing invaluable advice, and unconditional understanding and love. I am in awe of all of you.

Lastly, I want to thank my family for their unconditional support, guidance, and love through all the (many) ups and downs of the last years. I could not have done it without you.

Contents

1 Introduction

The strong interaction impacts our world from its smallest structures on the quark level up to the structure of neutron stars. Despite being one of the four fundamental forces in nature, there are still gaps in our understanding in many facets of the strong interaction. In particular the low-energy regime of quantum chromodynamics (QCD) requires further elucidation and thus continues to be the focal point of extensive research. For decades, exotic atoms have been recognised as ideal tools to further the understanding of nuclear and particle physics. Since kaons are the lightest mesons containing a strange quark, kaonic atoms in particular enable a direct study of the low-energy regime of QCD in the strangeness sector, for which a perturbative theoretical approach is not possible. The investigation of the antikaon-nucleon interaction in kaonic atoms can shed light on the complex processes involved in chiral symmetry breaking, which is of significance in the formation of the hadron masses. Due to the low relative energies of the bound kaon and nucleus in the kaonic atom, an extrapolation to zero relative energies is not necessary as is the case for scattering experiments. The antikaon-nucleon interaction can thus be observed directly and experimental input can be provided to constrain theoretical models and to reach a cohesive theoretical description.

Given the ideal conditions in form of a low-momentum kaon source provided by the DAΦNE (Double Annular Phi factory for Nice Experiments) collider, a research program dedicated to the study of the strong interaction effects in kaonic atoms formed at INFN-LNF (Istituto Nazionale di Fisica Nucleare - Laboratori Nazionali di Frascati) in Italy. A succession of several experiments investigated light kaonic atoms, starting with the DEAR (DAΦNE Exotic Atom Research) collaboration in the 1990s, and leading up to the current Silicon Drift Detectors for Hadronic Atom Research by Timing Application-2 (SIDDHARTA-2) experiment. The aim of the SIDDHARTA-2 collaboration is the measurement of the influence of the strong interaction on the ground state of kaonic deuterium via X-ray spectroscopy. From a combination of the results on kaonic hydrogen obtained by the antecedent SIDDHARTA experiment [1] and the SIDDHARTA-2 results on kaonic deuterium, the isospin-dependent antikaon-nucleon scattering lengths can be obtained for the first time. They provide crucial experimental input and a test bed for the existing theoretical models describing the antikaon-nucleon interaction.

In 2021, the SIDDHARTA-2 experiment started its commissioning phase with a reduced setup called SIDDHARTINO, which concluded with a first successful run with a helium-4 target. Since the planned measurement of kaonic deuterium is experimentally challenging due to the low expected X-ray yield and a high-radiation background environment, the commissioning phase provided

the important opportunity to assess the system's performance and optimise the setup. Following this phase were the installation of the full SIDDHARTA-2 setup in 2022 and several runs with helium-4. The data acquisition campaign of 2022 was finalised with a first run with a deuterium target.
This work focuses in part on the characterisation of two main components of the apparatus: the X-ray detection system in the form of silicon drift detectors (SDDs), and the Veto-2 system as part of a multi-stage veto system for active background suppression. Their performance during the kaonic helium and kaonic deuterium measurements was studied and the results are presented and discussed in this thesis.
The second emphasis of this work lies in the analysis of the data collected with the SIDDHARTINO and SIDDHARTA-2 experiments. A crucial aspect for X-ray spectroscopy of light kaonic atoms is the reduction of background in the X-ray spectra. In the SIDDHARTA-2 analysis, several techniques for background reduction were implemented, which are described in this work in detail. From the analysis of the kaonic helium data, a new, highly precise result was obtained for the $(3d \rightarrow 2p)$ transition in kaonic helium-4 which had last been measured by the SIDDHARTA experiment [2], [3] and, with unprecedented precision, the E62 experiment [4]. Moreover, several transitions from higher levels in kaonic atoms produced in the solid materials of the setup were observed. The transition energies of kaonic carbon, kaonic nitrogen, kaonic oxygen, and kaonic aluminium transitions are reported in this work for the first time. Lastly, the first X-ray spectrum obtained with a deuterium target by SIDDHARTA-2 and a first step towards its analysis are presented.

2 Kaonic Atoms

2.1 Formation

A kaonic atom is formed when a negatively charged kaon (K^-) is slowed down to a kinetic energy of a few tens of eV and eventually captured by an atomic nucleus via the Coulomb interaction. Due to the high mass of the K^- of 493.7 MeV as compared to the electron mass of 511 keV [5], the kaon is captured into an orbit with high principal quantum number $n \simeq \sqrt{\frac{\mu}{m_e}} n_e$, with $\mu = m_N m_K/(m_N + m_K)$ being the reduced mass of the system, m_N the mass of the nucleus, m_K the mass of the kaon, m_e the electron mass, and n_e the principal quantum number of the outermost electron shell. For kaonic hydrogen $n \sim 25$, while for kaonic deuterium $n \sim 27$. In a leading-order approximation, the binding energies B_n and Bohr radii r_B in the kaonic atom can be described by the Bohr formula:

$$B_n = \frac{\mu c^2 \alpha^2 Z^2}{2n^2}, \quad r_B = \frac{\hbar c}{\mu c^2 \alpha Z}, \tag{1}$$

with c being the vacuum speed of light, $\hbar$ the reduced Planck's constant, α the fine structure constant, and Z the atomic number of the kaonic atom. Due to the $1/\mu$ dependence of the Bohr radius, the kaon, while in a highly excited state, occupies approximately the same orbit as the substituted electron close to the nucleus, making hadronic atoms highly sensitive probes of the strong interaction.

After the capture, a complex quantum cascade process begins, in which multiple different processes of de-excitation of the kaonic atom are involved. The contribution of these processes depends on the atomic number Z of the kaonic atom. For kaonic atoms with $Z > 2$, the dominant processes are Auger emission and radiative decay, while for light kaonic atoms (hydrogen and helium), the effects of Coulomb de-excitation and Stark mixing are governing the cascade [6]. Fig. 1 schematically illustrates the atomic cascade for kaonic hydrogen.

Collisions of the kaonic hydrogen atoms lead to Coulomb de-excitation, a non-radiative process: the energy difference $\Delta E_{n,n^*}$ for a transition from state n to state n^* is converted into kinetic energy. Coulomb de-excitation occurs in higher-n states and competes with the process of external Auger emission of electrons.

The Stark effect describes the shifting or splitting of atomic states for an atom in an external electric field. States of the same n but different angular momenta l mix according to the selection rules $\Delta l = \pm 1, \Delta m = 0$, with m denoting the magnetic quantum number [7]. The mixing of l-states with $(l-1)$-states increases the probability of nuclear absorption from higher-n levels; therefore,

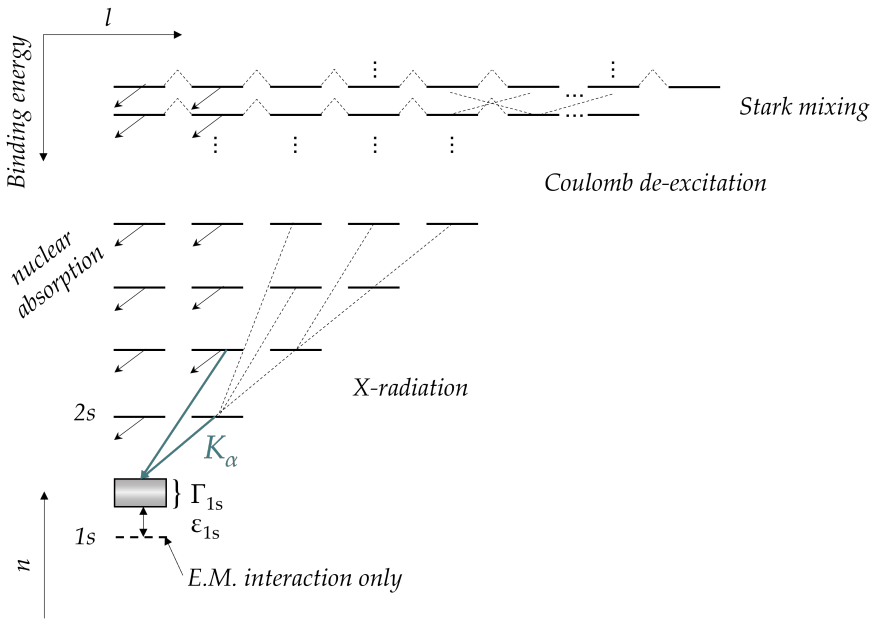

Figure 1: Schematic of the main mechanisms involved in the cascade process for kaonic hydrogen.

Stark mixing is the main cause of reduction of the X-ray yield in $Z \leq 2$ kaonic atoms. It dominates over all other de-excitation processes except radiative transitions, which prevail for low-n levels and during which characteristic X-rays are emitted.
After the kaon has reached the ground state of the kaonic atom, the quantum cascade terminates and the kaon is absorbed by the nucleons.

2.2 The Strong Interaction in Kaonic Atoms

As previously described, when captured into a kaonic atom, the kaon is located in close proximity to the nucleus due to its high mass compared to the emitted electron. Since the K^- is a hadron, it is subject to the strong interaction with the nucleus, in addition to the electromagnetic interaction. In kaonic hydrogen, the strong interaction induces an energy shift ε_{1s} and a broadening of the width Γ_{1s} to the atom's ground state (see Fig. 1), which are observable via X-ray spectroscopy of the kaonic atom. ε_{1s} is given by the difference between the measured energy of the $2p \rightarrow 1s$ transition in the kaonic atom, $E^{\text{measured}}_{2p\rightarrow 1s}$, and the value $E^{\text{E.M.}}_{2p\rightarrow 1s}$ extracted from solving the Klein-Gordon equation, only taking electromagnetic effects into account:

$$\varepsilon_{1s} = E^{\text{measured}}_{2p\rightarrow 1s} - E^{\text{E.M.}}_{2p\rightarrow 1s} \tag{2}$$

The decay width of the ground state, $\Gamma_{1s} = \hbar/\tau_{1s}$ with τ_{1s} denoting the $1s$

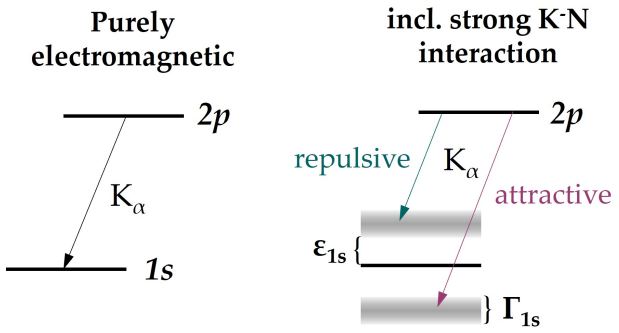

Figure 2: Schematic depiction of the effect of the strong interaction on the ground state in kaonic deuterium. On the left, the purely electromagnetic case is shown. On the right, the strong interaction induced a shift ε_{1s} and broadened width Γ_{1s}.

state's mean lifetime, is accessible via the Lorentzian linewidth of the measured X-ray transition. The binding energies in kaonic atoms are in the order of a few keV, which enables the study of the $\overline{\mathrm{K}}$N interaction almost at threshold. Although the strong interaction between the $\overline{\mathrm{K}}$ and the nucleons is strongly attractive, a negative, and thus *repulsive-type* shift ε_{1s} has been observed in kaonic hydrogen atoms (see the description of past experiments, Sec. 4.2). Fig. 2 depicts the two cases of an attractive- and a repulsive-type shift, contrasted with the case without any strong interaction effects. A repulsive-type shift ($\varepsilon_{1s} < 0$) corresponds to smaller binding energies compared to the purely electromagnetic case. For an attractive interaction, the shift has to be $\varepsilon_{1s} > 0$, corresponding to higher binding energies than for pure Coulomb interaction. The repulsive nature of the ground state shift can be explained by the presence of resonances closely below the $\mathrm{K}^-\mathrm{p}$ threshold. One of them, the $\Lambda(1405)$, has a mass only 26 MeV/c^2 below the threshold [5] and is commonly considered to be an isospin $I = 0$, strangeness $S = -1$ $\overline{\mathrm{K}}$N bound state [8]. These resonances, in particular the $\Lambda(1405)$ resonance, induce a strong coupling of the $\overline{\mathrm{K}}$N to the $\Sigma\pi$ channel and therefore heavily influence the $\overline{\mathrm{K}}$N dynamics [9]. The antikaon-nucleon scattering lengths are, for example, highly energy dependent and the $\overline{\mathrm{K}}$N interaction is strong and absorptive [10]. The coupling to sub-threshold channels also results in a decrease of binding energies in the kaonic atom and thus lesser-bound states, compatible with a repulsive-type shift of the ground state. The $\Lambda(1405)$ has been the subject of interest both theoretically and experimentally for decades to shed light on the complex dynamics of the antikaon-nucleon interaction at and below threshold (see for example [11]–[15]).

3 Low-Energy Antikaon-Nucleon Interactions

The theory of the strong interaction, Quantum Chromodynamics (QCD), is a colour SU(3) gauge quantum field theory. The study of low-energy baryon-meson interactions can shed light on the breaking of chiral symmetry in QCD, which happens in two ways: explicitly, due to the non-zero quark masses which result in a non-invariant Lagrangian under chiral transformations; and spontaneously, due to the non-zero quark condensate which leads to the creation of eight pseudoscalar mesons, called the Nambu-Goldstone bosons. In QCD with three quark flavours u, d, and s, the pions, kaons, and the η-meson are considered to be the Nambu-Goldstone bosons. A consequence of the breaking of chiral symmetry in QCD is the generation of the hadron masses. In this section, an overview of the theoretical concepts and methods used to describe low-energy QCD and, in particular, the meson-baryon interactions are provided.
Firstly, a brief outline of scattering theory is given to introduce the basic notions like the T-matrix formalism, scattering amplitudes, and scattering lengths, which are important concepts in the description of the $\overline{\mathrm{K}}\mathrm{N}$ interaction.
Secondly, the most prevalent theoretical approaches treating the low-energy antikaon-nucleon interaction are presented. In the region with a large strong coupling constant, the strong interaction is described via Chiral Perturbation Theory (χPT), an effective field theory. Effective field theories enable the local description, calculation, and prediction of physical phenomena at certain energy scales without the exact knowledge of the fundamental theory. They include all the relevant degrees of freedom and symmetries to formulate an effective Lagrangian, and to reproduce physical quantities with finite errors. Chiral perturbation theory was originally developed to describe the interaction between mesons and was later expanded to include the meson-baryon interactions [16]. For the strongly attractive antikaon-nucleon interaction, it was shown that a perturbative treatment within χPT was not possible due to the presence of the $\Lambda(1405)$ resonance closely below the $\overline{\mathrm{K}}\mathrm{N}$ threshold, as well as the strong coupling of the $\overline{\mathrm{K}}\mathrm{N}$ to the $\Sigma\pi$ channel [9].
Therefore, several approaches to describe the low-energy antikaon-nucleon interaction were developed. One approach is the use of so-called non-perturbative coupled-channels techniques, where the individual interactions of the $\overline{\mathrm{K}}$ with all nucleons in the nucleus are re-summed to construct an effective Lagrangian. Another method is the implementation of purely phenomenological optical potentials, whose parameters are adjusted to correctly reproduce experimental data [17]. An overview of both approaches and their prediction for the kaonic deuterium observables is given in this section.

3.1 An Introduction to Scattering Theory

Multiple scattering theory is a useful formalism to treat the low-energy antikaon-nucleon interaction. A scattering process typically describes an incident particle in initial state $|\Psi_i\rangle$ scattered on a potential V, resulting in the scattered state $|\Psi_s\rangle$. The initial state is an eigenstate of the free particle Hamiltonian $\mathrm{H}_0 = \frac{P^2}{2m}$ with momentum operator P and mass m. The aim of scattering theory is to solve the energy-eigenstate problem given by the Schrödinger equation

$$(E - \mathrm{H}_0 - \mathrm{V})|\Psi\rangle = 0, \tag{3}$$

where $|\Psi\rangle$ is the eigenstate of the complete Hamiltonian $\mathrm{H} = \mathrm{H}_0 + \mathrm{V}$. When the scattered state is defined as $|\Psi_s\rangle = |\Psi\rangle - |\Psi_0\rangle$, then Eq. 3 can be written as

$$|\Psi\rangle = |\Psi_0\rangle + (E - \mathrm{H}_0)^{-1}\mathrm{V}|\Psi\rangle, \tag{4}$$

which is known as the *Lippman-Schwinger equation* [18]. Using a Green's function G_0, Eq. 4 takes the form

$$|\Psi\rangle = |\Psi_0\rangle + \mathrm{G}_0\mathrm{V}|\Psi\rangle, \tag{5}$$

with the formal solution

$$|\Psi\rangle = (1 - \mathrm{G}_0\mathrm{V})^{-1}|\Psi_0\rangle. \tag{6}$$

An iterative solution to the Lippman-Schwinger equation is given by the Born series, where $|\Psi_s\rangle = (\mathrm{G}_0\mathrm{V} + \mathrm{G}_0\mathrm{V}\mathrm{G}_0 + \mathrm{G}_0\mathrm{V}\mathrm{G}_0\mathrm{V}\mathrm{G}_0\mathrm{V} + \dots)|\Psi_0\rangle$. Factoring out G_0 gives

$$|\Psi_s\rangle = \mathrm{G}_0\mathrm{T}|\Psi_0\rangle, \tag{7}$$

with the transfer matrix (T-matrix) $\mathrm{T} = \mathrm{V}(1 - \mathrm{G}_0\mathrm{V})^{-1}$ [18]. The T-matrix formalism is shown for the $\overline{\mathrm{K}}\mathrm{N}$ interaction in the framework of coupled-channels in the following Sec. 3.2.

3.1.1 The Scattering Amplitude and Scattering Length

For now, only single-channel elastic scattering is considered. The scattering amplitude $f(\theta, \varphi)$ is a complex quantity describing the scattering of the particle in various directions (here in polar coordinates). Assuming the initial particle is described via a plane wave, the scattering amplitude represents a modification of the outgoing spherical wave dependent on θ and φ. In forward direction ($\theta = 0$), it correlates to the total cross section of the scattering process σ_{tot}:

$$\sigma_{\text{tot}} \propto \frac{4\pi}{k} f(0), \tag{8}$$

with the wave vector of the incident particle k [19]. In momentum representation, the T-matrix relates to the scattering amplitude f_k as follows:

$$\langle k_s|\mathrm{T}|k\rangle = -\frac{\hbar^2}{4\pi^2 m} f_k(\theta, \varphi), \tag{9}$$

where k_s denotes the wave vector of the scattered particle. Eq. 9 shows that the matrix elements of the T-matrix are equivalent to the scattering amplitude [20], which will also be seen in Sec. 3.2, where a description of the calculation of the forward scattering amplitude of the antikaon-nucleon interaction from the T-matrix elements is provided. Furthermore, it can be shown that the scattering amplitude is the Fourier-transform of the scattering potential [21]. If the symmetry of the scattering potential allows for it, it can be useful to utilise the conservation of angular momentum in the description of a scattering process. In a partial wave expansion, the scattered wave is expressed as a series of Legendre polynomials depending on the angular momentum, describing partial waves with partial scattering amplitudes. For low-energy interactions, typically only the first term in the expansion, the s-wave component, is considered. Since for low energies $k \to 0$, the scattering length a of single-channel elastic scattering is defined via the total cross section of s-wave scattering $\sigma_{\text{tot},l=0}$

$$\sigma_{\text{tot},l=0}(k \to 0) = 4\pi a^2. \tag{10}$$

This relation suggests an interpretation of the scattering length as an effective scattering radius [21], and it is closely coupled to the nature of the scattering potential. If $a < 0$, the scattering potential is attractive; for repulsive interactions, $a > 0$.
In the case of multiple open scattering channels, however, the scattering length becomes a complex number: $a = A - iB$, with A and B being real numbers [22], [23]. In light kaonic atoms, additional, highly absorptive scattering channels are present below threshold, and $\overline{\mathrm{K}}\mathrm{N} \to \mathrm{Y}\pi$ scattering has to be considered, where Y describes a hyperon with strangeness $S = -1$. A hyperon is a baryon containing a strange quark, but no heavy charm, top, or bottom quark. The imaginary part of the scattering length is directly proportional to the absorptive cross section $\overline{\mathrm{K}}\mathrm{N} \to \Sigma\pi$, which necessitates that $B > 0$ [22], [24]. The $\overline{\mathrm{K}}\mathrm{N}$ scattering length is a measure to describe the dynamics of the antikaon-nucleon interaction at threshold. Its derivation in a coupled-channels framework is shown in Sec. 3.2.

3.2 The Chiral Unitary Approach with Coupled Channels

The goal of the coupled-channels approach is the construction of an effective Lagrangian which accurately describes the low-energy antikaon-nucleon interaction while including the low-energy chiral symmetries. The inter-channel couplings are derived from a chiral effective Lagrangian involving all the following meson-baryon interactions: $\pi\Lambda$, $\pi\Sigma$, $\overline{\mathrm{K}}\mathrm{N}$, $\eta\Lambda$, $\eta\Sigma$, and $\mathrm{K}\Xi$ with correct combinations of charges and isospins. The chiral Lagrangian

$$\mathcal{L}_{\phi B} = \langle \bar{B}(i\gamma_\mu D^\mu - M_0)B\rangle + \frac{D}{2}\langle \bar{B}\gamma_\mu\gamma_5[u^\mu, B]_+\rangle + \frac{F}{2}\langle \bar{B}\gamma_\mu\gamma_5[u^\mu, B]\rangle, \quad (11)$$

with $D_\mu B := \partial_\mu B + \frac{1}{2}[[u^\dagger, \partial_\mu u], B]$, D and F being axial coupling constants, and $\langle \dots \rangle$ being the trace in flavour space. The Nambu-Goldstone bosons are represented with the meson matrix ϕ via $u^2 := \exp(i\phi/F_0)$ and $u^\mu := iu^\dagger\partial^\mu u - iu\partial^\mu u^\dagger$, with F_0 being the meson decay constant. The baryons Σ, Λ, Ξ, and N are included via the matrix B [25]. The coupled-channels meson-baryon interaction in SU(3) can be written as $\hat{V}_{ij} = \langle i|\hat{V}|j\rangle$, with the interaction matrix elements $\hat{V}_{ij}$, final channel i, and initial channel j. $\hat{V}_{ij}$ is a function of the centre-of-mass energy of the meson-baryon system $\sqrt{s}$, the scattering angles $\Omega = \{\theta, \varphi\}$, and the degrees of freedom for the baryon spin σ_i and σ_j:

$$V_{ij}(\sqrt{s}) = \frac{1}{8\pi}\sum_\sigma \int d\Omega \hat{V}_{ij}(\sqrt{s}, \Omega, \sigma_i, \sigma_j). \quad (12)$$

The leading-order contribution to meson-baryon scattering is given by the Weinberg-Tomozawa term [26], [27], which is pictured in Fig. 3 *a* and is derived from the covariant derivative $D_\mu B$, resulting in

$$V_{ij}^{\mathrm{WT}}(\sqrt{s}) = \frac{C_{ij}^{\mathrm{WT}}}{8f_i f_j}\mathcal{N}_i\mathcal{N}_j(2\sqrt{s} - M_i - M_j), \quad (13)$$

with M_i denoting the baryon mass, f_i the meson decay constant and $E_i = \sqrt{M_i^2 + q_i^2}$, where q_i is the centre-of-mass three-momentum of channel i. C_{ij}^{WT} are constants derived from the SU(3) Clebsch-Gordan coefficients, and $\mathcal{N}_i$ is a normalisation factor [28].

The next contribution to the meson-baryon interaction are the Born terms (see Fig. 3 *b* and *c*). They arise from axial vector currents proportional to D and F from hyperon decays. The direct Born terms (Fig. 3 b) are of the form

$$\begin{aligned} &V_{ij}^{\text{Born, direct}}(\sqrt{s}) = \\ &= -\sum_{k=1}^{8} \frac{C_{\bar{i}i,k}^{\mathrm{Born}} C_{\bar{j}j,k}^{\mathrm{Born}}}{12 f_i f_j}\mathcal{N}_i\mathcal{N}_j \frac{(\sqrt{s} - M_i)(\sqrt{s} - M_j)(\sqrt{s} - M_k)}{s - M_k^2}, \end{aligned} \quad (14)$$

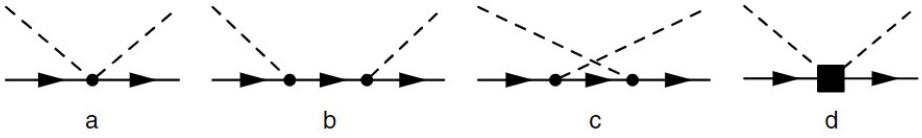

Figure 3: Feynman diagrams for the meson-baryon scattering. *a*: Weinberg-Tomozawa term, *b*: direct Born term, *c*: crossed Born term, and *d*: NLO terms. *From [13].*

with k being an intermediate baryon channel, and $C_{\bar{i}i,k}^{\mathrm{Born}}$ involving D and F [28].
To include contributions up to the order $(O)(q^2)$ in the meson-baryon momentum space, next-to-leading order (NLO) contact terms are added (see Fig. 3 *d*) involving low-energy constants which relate to the baryon masses [25]:

$$V_{ij}^{\mathrm{NLO}}(\sqrt{s}) = \frac{\mathcal{N}_i\mathcal{N}_j}{f_i f_j}[C_{ij}^{\mathrm{NLO1}} - 2C_{ij}^{\mathrm{NLO2}}(E_iE_j + \frac{q_i^2 q_j^2}{3\mathcal{N}_i\mathcal{N}_j})], \tag{15}$$

where C_{ij}^{NLO1} and C_{ij}^{NLO2} include the low-energy constants [28].
For the calculation of observables of the $\mathrm{K^-p}$ interaction, the meson-baryon coupled-channels T-matrix is related to the forward scattering amplitudes f_{ij} as follows:

$$f_{ij}(\sqrt{s}) = \frac{1}{8\pi\sqrt{s}} T_{ij}(\sqrt{s}), \tag{16}$$

with T_{ij} denoting a matrix element of T. The T-matrix is related to the meson-baryon interaction V derived above via

$$\mathrm{T} = (\mathrm{V}^{-1} - \mathrm{G})^{-1}, \tag{17}$$

where G is a diagonal matrix in which the diagonal elements describe the meson-baryon loop functions [28]. From Eq. 16, the $\mathrm{K^-p}$ elastic scattering length $a_{\mathrm{K^-p}}$ is given via

$$a_{\mathrm{K^-p}} = f_{11}(\sqrt{s} = m_{\mathrm{K^-}} + m_{\mathrm{p}}), \tag{18}$$

where $m_{\mathrm{K^-}}$ and m_{p} denote the masses of the $\mathrm{K^-}$ and proton, respectively [28]. In spectroscopy experiments of light kaonic atoms, the observables are the energy shift ε and the broadened width Γ of the ground state induced by the strong interaction. For kaonic hydrogen, this shift and width are related to the *s*-wave antikaon-proton scattering length $a_{\mathrm{K^-p}}$ via an *improved Deser-Trueman-Baumann-Thirring-type formula*. This formula was originally derived for pionic atoms. The energy shift in the pionic atom naturally occurred from the Schrödinger equation including the Coulomb potential and the potential for the short-range pion-nucleon interaction. The total level shift was then determined with an R-matrix formalism from a comparison of the energy shift to the matrix element describing the forward scattering of pions

on protons [29]. For the case of the kaonic hydrogen, the Deser-type equation without isospin-breaking corrections was formulated as

$$\varepsilon_{1s} - \frac{i}{2}\Gamma_{1s} = -\alpha^3 \mu_c^2 a_{\mathrm{K^-p}}, \tag{19}$$

with ε_{1s} and Γ_{1s} denoting the ground state shift and width of $\mathrm{K^-p}$, α being the fine structure constant, and μ_c the reduced mass of the $\mathrm{K^-p}$ system [30]. In contrast to pionic atoms, the isospin-breaking corrections in kaonic atoms are large, and the Deser-Trueman-Baumann-Thirring-type formula was corrected by deriving an effective non-relativistic Lagrangian able to describe the spectrum of kaonic deuterium with isospin corrections $\delta \sim m_d - m_u$ (m_d and m_u being the masses of down and up quarks, respectively) up to $\mathcal{O}(\delta^4)$ [30]. The corrected equation now reads [30], [31]

$$\varepsilon_{1s} + \frac{i}{2}\Gamma_{1s} = 2\alpha^3 \mu^2 a_{\mathrm{K^-p}}[1 - 2\alpha\mu(\ln\alpha - 1)a_{\mathrm{K^-p}} + ...]. \tag{20}$$

While for kaonic hydrogen the improved Deser-Trueman formula produces precise results, it has been shown that for kaonic deuterium the outcome is less accurate. Complete three-body calculations using $\overline{\mathrm{K}}\mathrm{N}$-interaction potentials with coupled-channels techniques are required for $\mathrm{K^-d}$. The energy shift and width in kaonic deuterium are obtained from a solution of the Schrödinger equation using a variational method. A Coulomb potential and a $\overline{\mathrm{K}}\mathrm{N}$ interaction potential [32] are included. From the obtained solutions, the kaonic deuterium s-wave scattering length $a_{\mathrm{K^-d}}$ is extracted [33]. From a combination of $a_{\mathrm{K^-p}}$ and $a_{\mathrm{K^-d}}$, the isospin-dependent ($I = 0, 1$) antikaon-nucleon scattering lengths a_0 and a_1 are separately accessible via

$$a_{\mathrm{K^-p}} = \frac{1}{2}(a_0 + a_1), \tag{21}$$

$$a_{\mathrm{K^-n}} = a_1, \tag{22}$$

and

$$a_{\mathrm{K^-d}} = \frac{4(m_\mathrm{N} + m_\mathrm{K})}{2m_\mathrm{N} + m_\mathrm{K}} Q + C, \tag{23}$$

where $a_{\mathrm{K^-n}}$ is the kaon-neutron s-wave scattering length, C a correction for higher-order terms from three-body interactions, and

$$Q = \frac{1}{2}(a_{\mathrm{K^-p}} + a_{\mathrm{K^-n}}) = \frac{1}{4}(a_0 + 3a_1). \tag{24}$$

The extraction of the isospin-dependent $\overline{\mathrm{K}}\mathrm{N}$ scattering lengths a_0 and a_1 provides crucial constraints for the theoretical models describing the low-energy $\overline{\mathrm{K}}\mathrm{N}$ interaction. Several theoretical models applying coupled-channels methods exist with the aim to correctly reproduce the existing kaonic hydrogen data as obtained by the SIDDHARTA collaboration and to provide an

accurate description of the antikaon-nucleon interaction at low energies. The following approaches are presented in Fig. 4: Prague (P) [34], Kyoto-Munich (KM) [28], Bonn (B2, B4) [35], Barcelona (BCN) [36], and Murcia (M_I, M_{II}) [37]. The top panels of Fig. 4 show the results of these models for the real and imaginary parts of the K^-p elastic scattering amplitude as a function of energy. The SIDDHARTA data point clearly constrains the models at and above the K^-p threshold with the exception of the Bonn approaches, whereas below threshold the models show the biggest discrepancies. This is due to a lack of experimental data in this region. At the bottom panels, the K^-n elastic scattering amplitudes from the different theoretical approaches are presented. They are in considerable disagreement over the entire energy range, indicating that experimental input from a kaonic deuterium measurement is needed for a uniform theoretical description.

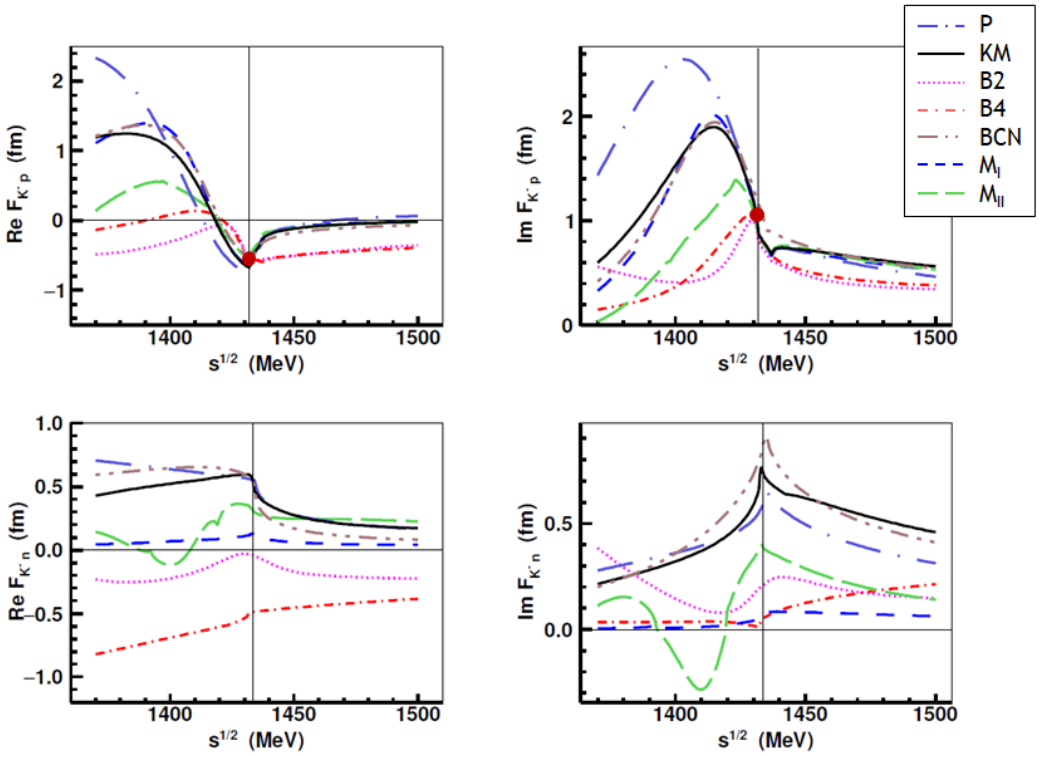

Figure 4: *Top:* Elastic *s*-wave scattering amplitudes for K^-p as predicted by the P (dot-long-dashed, purple), KM (continuous, black), B2 (dotted, magenta), B4 (dot-dashed, red), BCN (dot-dot-dashed, brown), M_I (dashed, blue), and M_{II} (long-dashed, green) models. The SIDDHARTA data point is denoted in red; the thin vertical lines represent the K^-N thresholds. *Bottom:* K^-n elastic *s*-wave scattering amplitudes resulting from the discussed models. *From [38].*

3.3 Optical Models

A different approach to describe the antikaon-nucleon interaction at low energies is using so-called optical models. These models consider the antikaon-nucleon interaction as a multichannel-scattering process and introduce a "refractive index" for the scattering of the hadron on the nucleus. This "refractive index" is described by ways of a complex phenomenological optical potential V, which typically is of the form

$$V_{\mathrm{opt}} = -\frac{2\pi}{\mu}\left(1+\frac{\mu}{m}\right)\bar{a}\rho(r), \tag{25}$$

where μ describes the reduced mass of the hadron-nucleus system, m the nucleon mass, $\bar{a}$ is an average complex hadron-nucleon scattering length, and $\rho(r)$ is the nucleon density distribution [17]. The real part of the optical potential describes the attractive part of the interaction and enables the expression of the binding energy between the hadron and the nucleus. The imaginary part on the other hand describes the absorptive part of the interaction and relates to the decay width. Inserting this potential into the Klein-Gordon equation in addition to a Coulomb potential and solving this equation allows for the extraction of the energy shift and width of the energy level. For sufficiently low density, the optical potential relates to the hadron-nucleon forward scattering amplitude $f(kq;kq)$ via

$$2m_{\mathrm{h}}V_{\mathrm{opt}}(q) = -4\pi\sum_{p} n(k)f(kq;kq), \tag{26}$$

where k and q are the momenta of the hadron and the scatterers in the target, respectively; $n(k)$ denotes the number of scatterers, and m_{h} the mass of the hadron [39]. The effects of the strong interaction in kaonic atoms do not allow for a perturbative treatment, which is mirrored by the fact that the real part of the optical potential typically appears attractive despite the observed repulsive energy shifts. This effect is a result of the magnitude of the imaginary part of the potential, which is similar or larger than that of its real part. In the low-density limit, a repulsive potential is expected [17], [39]. This behaviour of the potential can be explained by the presence of the $\Lambda(1405)$ resonance below the $\mathrm{K^-p}$ threshold [40]. To describe this effect where the real part of the potential seems to incorporate both absorptive and repulsive components, a density-dependent optical potential $V_{\mathrm{opt}}^{\mathrm{DD}}$ was proposed [8]:

$$2\mu V_{\mathrm{opt}}^{\mathrm{DD}}(r) = -4\pi\left(1+\frac{\mu}{m}\right)\left[b + B\left(\frac{\rho(r)}{\rho(0)}\right)^{\alpha}\right]\rho(r), \tag{27}$$

with μ denoting the reduced mass of the $\mathrm{K^-}$-nucleus system, m the mass of the nucleon, $\rho(r)$ the normalised nuclear-matter density distribution . b and B are complex coefficients. The exponent α, b, and B are obtained from a fit to the

available K^- data [8]. In this way, within the nucleus and on its surface, the real part of the density-dependent optical potential was found to be attractive, and solutions were found which satisfied the low-density limit [8].

3.4 Theoretical Predictions for Kaonic Deuterium

The varying theoretical predictions for the $1s$ shift, width, and the K^-d scattering length a_{K^-d} are summarised in Table 1 and Fig. 5. The SIDDHARTA-2 experiment aims to achieve a precision of 30 eV for the kaonic deuterium $1s$ shift and 80 eV for the width, and hence provides an opportunity to rule out some of the theoretical predictions.

Table 1: Calculations for the kaonic deuterium $1s$ shift ε_{1s}, width Γ_{1s}, and scattering length a_{K^-d} for from different theoretical approaches.

ε_{1s} (eV)	Γ_{1s} (eV)	a_{K^-d} (fm)	Reference
-769	674	$-1.42 + i1.09$	Gal (2007) [41]
-779	650	$-1.46 + i1.08$	Döring *et al.* (2011) [42]
-787	1011	$-1.48 + i1.22$	Shevchenko (2012) [43]
-887	757	$-1.58 + i1.37$	Mizutani *et al.* (2013) [44]
-670	1016	$-1.42 + i1.60$	Weise *et al.* (2017) [33]
-803	2280	$-0.59 + i2.70$	Liu *et al.* (2017) [45]

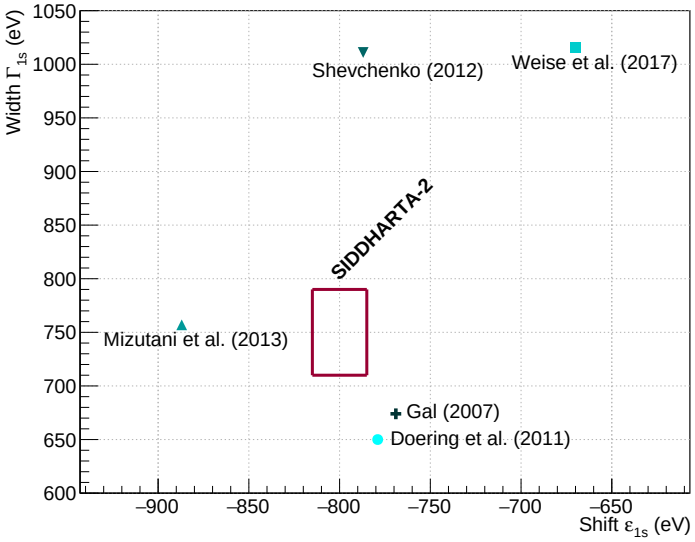

Figure 5: Theoretical predictions for the kaonic deuterium $1s$ shift and width for various theoretical models. The SIDDHARTA-2 experiment aims for a precision of 30 eV for the shift and 80 eV for the width, respectively. The position of the red rectangle is arbitrary.

4 Introduction to Light Kaonic Atom Experiments

4.1 DAΦNE

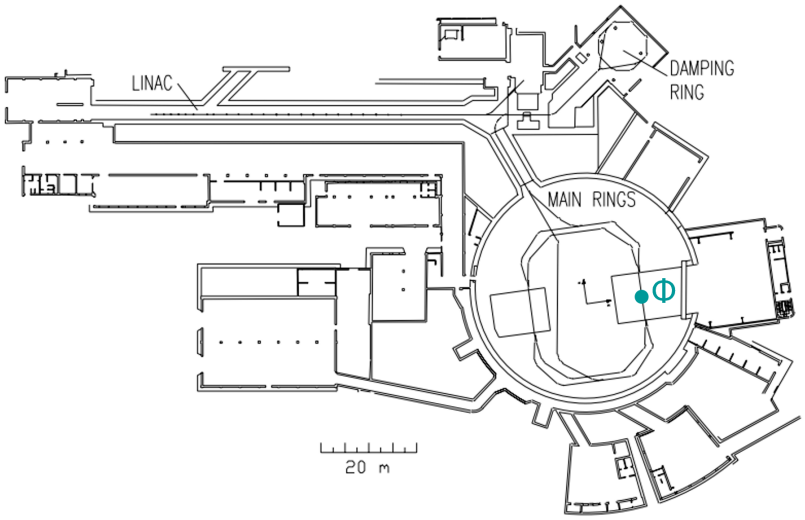

Figure 6: Schematic drawing of the DAΦNE accelerator complex at LNF. *Adapted from [46].*

DAΦNE is a double-ring electron-positron collider located at INFN-LNF in Italy. The collider complex is comprised of a LINAC (linear accelerator), an accumulator, and the main synchrotron collider rings (see Fig. 6). A particle accelerator's ability to produce a certain number of interactions is measured by its luminosity $\mathcal{L}$. It is defined via the number of events per time dN/dt and the cross section σ_b: dN/dt= $\mathcal{L} \cdot \sigma_b$ and has the dimension of $[(\text{area} \cdot \text{time})^{-1}]$. Often of more interest for the experiment is the integrated luminosity, i.e. the integral of $\mathcal{L}$ over the sensitive time. The integrated luminosity has the dimension $[\text{area}^{-1}]$ and is typically given in the unit barn with 1 b = 10^{-28} m^2. In 2008, the collision scheme of DAΦNE was updated to a Crab-Waist configuration to improve its luminosity by a factor of three, as proven during its delivery of luminosity to the SIDDHARTA experiment in 2009 with a peak luminosity of 4.53×10^{32} $\text{cm}^{-2}\text{s}^{-1}$ [47]–[49]. The main beam parameters of DAΦNE after its update are summarised in Table 2. Typical operation cycles of electron and positron injection, observed in May 2022, are shown in Fig. 7. The top panel shows the electron and positron currents and the bottom panel shows the beam luminosity measured by the SIDDHARTA-2 luminosity monitor, explained in more detail in section 5.1.

DAΦNE operates at the centre-of-mass energy of the ϕ-meson at 1.02 GeV [50], producing the ϕ-mesons through e^+e^- annihilation almost at rest. Pairs of

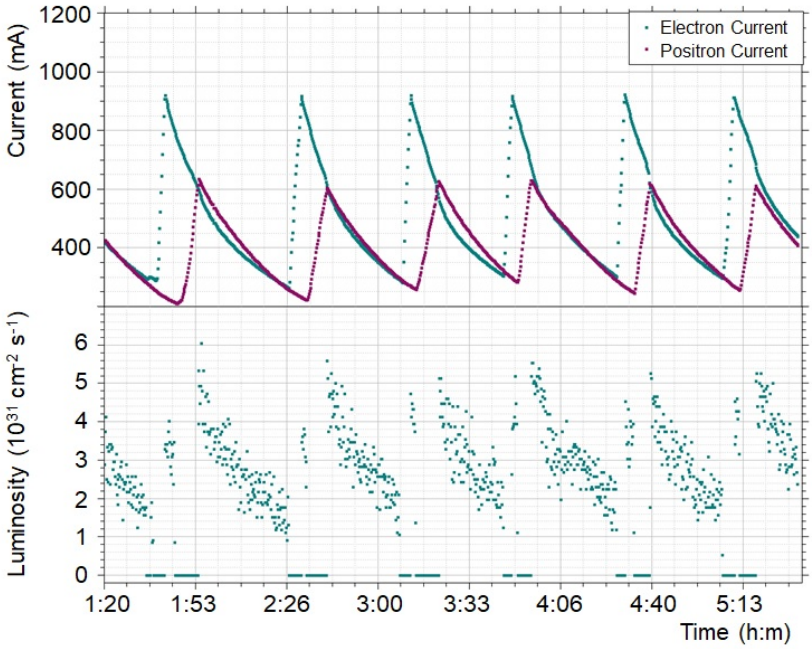

Figure 7: *Top:* Typical cycles of electron and positron currents. The data were taken on May 16, 2022. *Bottom:* Instantaneous luminosity during beam cycle.

charged kaons K^+K^- are produced in the subsequent ϕ-decay with a branching ratio of $(49.2 \pm 0.5)\%$. Other possible decay channels of the ϕ-meson are to neutral kaon pairs $K^0_L K^0_S$ with a branching ratio of $(34.0 \pm 0.4)\%$ or to a ρ-meson with one or three pions with a branching ratio of $(15.24 \pm 0.33)\%$ [50]. The charged kaons are emitted almost back-to-back except for a boost in direction towards the centre of the collider rings due to the crossing angle of the e^+- and e^--beams of 40 to 60 mrad. DAΦNE is a unique source for low-momentum, nearly monochromatic kaons, with only a small momentum of 127 MeV/c and a momentum spread of $\delta p/p < 0.1\%$ [51].

Table 2: Main parameters of the DAΦNE beams after the update to the Crab-Waist collision scheme [49], [51].

DAΦNE Parameters	
Peak luminosity ($cm^{-2}s^{-1}$)	4.63×10^{32}
Number of bunches	105
e^- current (mA)	1520
e^+ current (mA)	1000
Bunch length (cm)	$1.5 - 2.0$
Radio Frequency (MHz)	368.7
Crossing angle (mrad)	50

4.2 Past Kaonic Atom Experiments

Light kaonic atoms have been studied intensely in past decades via various experimental methods. The disagreement of the obtained results, however, led to the so-called "kaonic hydrogen puzzle" in the 1980s. While this question was finally answered by the KpX experiment, kaonic atoms are still a focal point of low-energy QCD studies, since theoretical models for this regime are in need of constraint via experiment input. The kaonic deuterium measurement of SIDDHARTA-2 will, in combination with the results of its predecessor SIDDHARTA, be a next step towards a uniform description of the $\overline{\mathrm{K}}\mathrm{N}$ interaction.

4.2.1 KpX

In the late 1990s, the KpX (E228) experiment was performed at the High Energy Accelerator Research Organization (KEK) Proton Synchroton at the K3 beam line. Its goal was to measure X-ray transitions in kaonic hydrogen atoms. Previous measurements of this kind produced the kaonic atoms in a liquid target, which decreased the X-ray yield significantly due to the Stark effect. KpX employed a gaseous hydrogen target for the first time, with a pressure of 4 atm and a temperature of 100 K. For the reduction of background, several measures were employed: Cherenkov counters identified the kaons. A system of two Multiwire Proportional Chambers (MWPCs) and hodoscope detectors was used to tag pions with a certain momentum to eliminate high-energy γ-ray background. For the detection of the X-rays, Si(Li) detectors operated in hydrogen gas were used. The KpX experiment observed the kaonic hydrogen K_α line with unprecedented precision. The X-ray spectrum is shown in Fig. 8. The $1s$ shift and width were determined as follows [52]:

$$\varepsilon_{1s} = (-323 \pm 63_{\mathrm{stat}} \pm 11_{\mathrm{syst}})\ \mathrm{eV}, \tag{28}$$

$$\Gamma_{1s} = (407 \pm 208_{\mathrm{stat}} \pm 100_{\mathrm{syst}})\ \mathrm{eV}. \tag{29}$$

These results contradicted the previously performed experiments on light kaonic atoms [53]–[55], which all suggested an attractive-type $1s$ shift. The KpX data was in agreement with low-energy scattering experiments [56]–[58], and solved this "kaonic hydrogen puzzle".
The KpX experiment not only led to the resolution of the "kaonic hydrogen puzzle", but also eliminated the discrepancies between theoretical predictions and experimental data for the energy shift of the $2p$ level in kaonic helium-4, the so-called "kaonic helium puzzle". The average value of the shift found in three experiments [59]–[61] differed from the theoretical predictions [62], [63] by more than five standard deviations. KpX used a superfluid ^{4}He target and

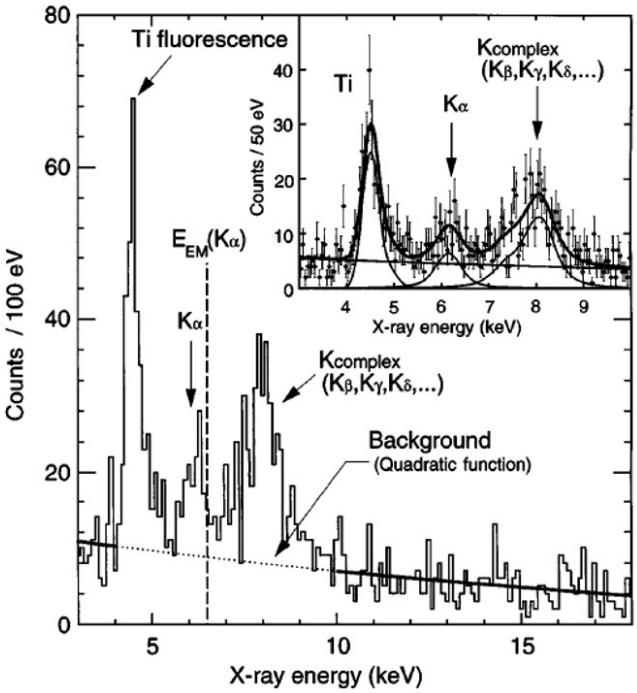

Figure 8: Kaonic hydrogen spectrum obtained by KpX, with the fitting results shown in the inset. *From [52].*

silicon drift detectors for the detection of the kaonic ^{4}He X-rays. The energy of the kaonic helium-4 ($3d \to 2p$) transition was measured and reported to be $(6467 \pm 3_{\text{stat}} \pm 2_{\text{syst}})$ eV [64]. The $2p$ level shift was found to be

$$\varepsilon_{2p} = (2 \pm 2_{\text{stat}} \pm 2_{\text{syst}}) \text{ eV}. \tag{30}$$

This new precise measurement was in agreement with the theoretical predictions and led to the solution of the "kaonic helium puzzle". The observed X-ray spectra are shown in Fig. 9.

4.2.2 DEAR

The DEAR experiment was located at one of the interaction points (IPs) of the DAΦNE collider at INFN-LNF. It aimed to measure X-ray transitions in kaonic hydrogen atoms, taking advantage of the conditions at DAΦNE in the form of low-momentum, monochromatic kaons and no contamination of other photons and particles, i.e. pions. Its apparatus consisted of three main systems - a kaon detector, a cryogenic target cell for kaonic atom production, and an X-ray detection system composed of Charge-Coupled Devices (CCDs). The cylindrical target cell was made of aluminium and fibre glass structures, with Kapton sidewalls and entrance window. Surrounding the target cell were 16 CCD chips. The kaon detector consisted of two plastic scintillators above and

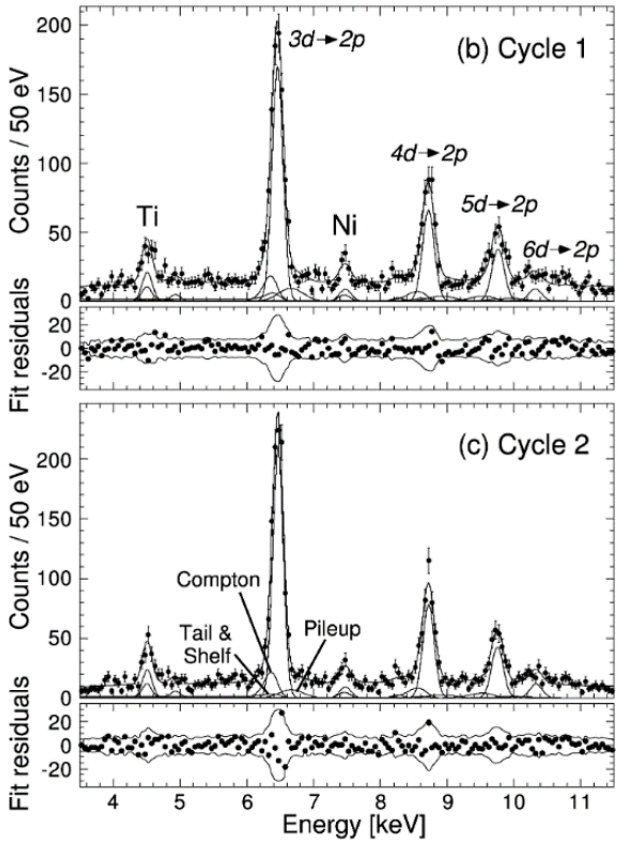

Figure 9: Kaonic helium-4 X-ray spectra with fit functions and residuals obtained by KpX for cycle 1 (*top*), and cycle 2 (*bottom*) *Adapted from [64].*

below the interaction point [65]. Its purpose was the definition of a kaon trigger via the requirement of a coincidence in signals in both scintillators, taking advantage of the back-to-back emission of the charged kaons. The experiment was confronted with high levels of both hadronic and electromagnetic background which in part were decreased by passive shielding with lead. For kaonic hydrogen, DEAR collected data for an integrated luminosity of 58.4 pb^{-1}. The ground state shift and width were extracted from the CCD spectra and were found to be

$$\varepsilon_{1s} = (-193 \pm 37_{\text{stat}} \pm 6_{\text{syst}}) \text{ eV}, \tag{31}$$

$$\Gamma_{1s} = (249 \pm 111_{\text{stat}} \pm 30_{\text{syst}}) \text{ eV}. \tag{32}$$

Two independent analyses were performed with varying treatment of the background; the values above represent the weighted mean of the results of both approaches. Fig. 10 shows the kaonic hydrogen spectra obtained by both analyses (panels *a)* and *b)*) [65]. The DEAR results show smaller errors and differ from those of KpX by more than one σ, but confirmed the repulsive-type shift and hence the solution of the "kaonic hydrogen puzzle".

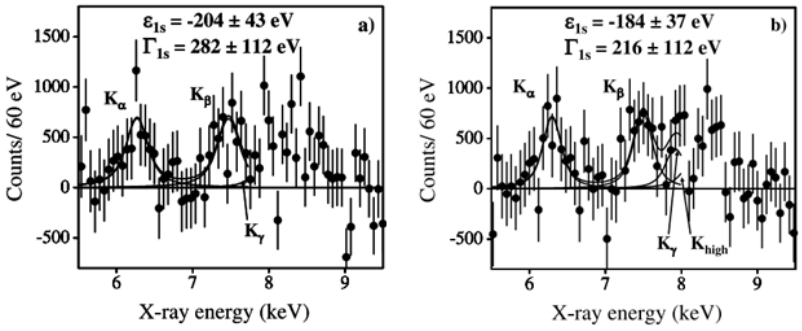

Figure 10: Fitted K^-p spectra obtained by different treatment of the background in two independent analyses by the DEAR collaboration. *Adapted from [65].*

4.2.3 SIDDHARTA

The SIDDHARTA experiment, installed at the interaction point of DAΦNE at LNF after the update to the new collision scheme, aimed to improve the precision of the kaonic hydrogen measurement previously performed by DEAR. To improve the energy resolution and further suppress the background, SDDs were used for X-ray detection instead of CCDs; in contrast to CCDs, SDDs are triggerable and can provide timing information. This information was used to define a time window in coincidence with the K^+K^- signals from the kaon detector to select only kaonic X-ray signals. This played a crucial role in the suppression of asynchronous background, which was the main source of background for DEAR. Hence, the signal-to-background ratio (S/B) improved by a factor of ten compared to the DEAR ratio. The SIDDHARTA experimental apparatus is pictured in Fig. 11.
As described previously for the DEAR experiment, the kaon detector consisted of two plastic scintillators placed below and above the interaction point. A cylindrical target cell with Kapton sidewalls and entrance window inside the vacuum chamber was surrounded by 144 SDDs with an energy resolution of $\sim$ 180 eV (FWHM) at 8 keV and a timing resolution of below 1 μs [1]. In 2009, data were collected for an integrated luminosity of $\sim$ 340 pb^{-1} with a hydrogen target, $\sim$ 100 pb^{-1} with a deuterium target, $\sim$ 17 pb^{-1} with helium-3, and $\sim$ 20 pb^{-1} with a helium-4 target [2], [66], [67]. The kaonic hydrogen and deuterium spectra observed by SIDDHARTA are shown in Fig. 12. The $1s$ shift and width in kaonic hydrogen were determined to be

$$\varepsilon_{1s} = (-283 \pm 36_{\text{stat}} \pm 6_{\text{syst}}) \text{ eV}, \tag{33}$$

$$\Gamma_{1s} = (541 \pm 89_{\text{stat}} \pm 22_{\text{syst}}) \text{ eV}, \tag{34}$$

providing the most precise measurement of the kaonic hydrogen K-series X-ray transitions to-date [1]. In the kaonic deuterium spectrum, the K-series transition lines are not visible due to the lower K^-d X-ray yield [68], [69].

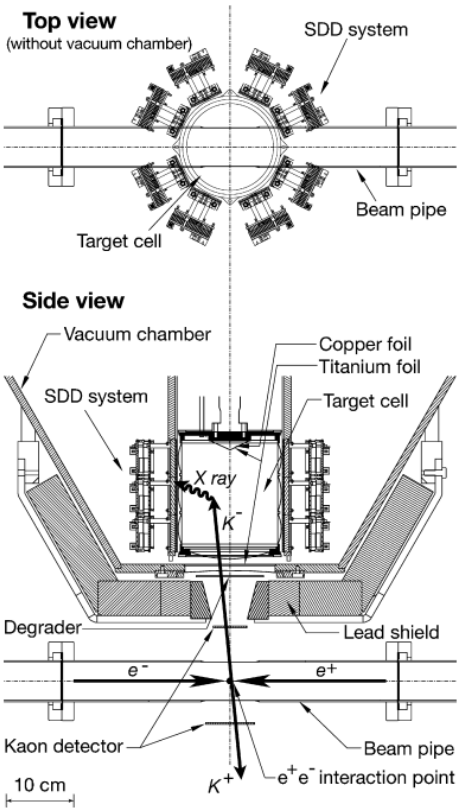

Figure 11: Schematic of the SIDDHARTA experimental apparatus at the DAΦNE collider. *From [1].*

Moreover, SIDDHARTA performed the first measurement of kaonic helium-4 X-rays using a gaseous target. The $(3d \to 2p)$ transition energy was determined to be $6463.6 \pm 5.8 \pm 2.0$ eV. The energy shift and width of the $K^{-4}He$ $2p$ level were found to be

$$\varepsilon_{2p} = (0 \pm 6_{\text{stat}} \pm 2_{\text{syst}}) \text{ eV}, \tag{35}$$

$$\Gamma_{2p} = (14 \pm 8_{\text{stat}} \pm 5_{\text{syst}}) \text{ eV}, \tag{36}$$

with the X-ray spectrum shown in Fig. 13 *(a)* [2], [3]. These new values confirmed the results of the KpX collaboration and thus the solution of the "kaonic helium puzzle".
In addition to the measurement of kaonic helium-4, SIDDHARTA collected data with a gaseous helium-3 target. The $(3d \to 2p)$ transition was observed for the first time in kaonic helium-3 at an energy of $(6223.0 \pm 2.4_{\text{stat}} \pm 3.5_{\text{syst}})$ eV (see Fig. 13 *(b)*) [67]. The $2p$ level shift [67] and width [3] of kaonic helium-3 were determined to be

$$\varepsilon_{2p} = (-2 \pm 2_{\text{stat}} \pm 4_{\text{syst}}) \text{ eV}, \tag{37}$$

$$\Gamma_{2p} = (6 \pm 6_{\text{stat}} \pm 7_{\text{syst}}) \text{ eV}. \tag{38}$$

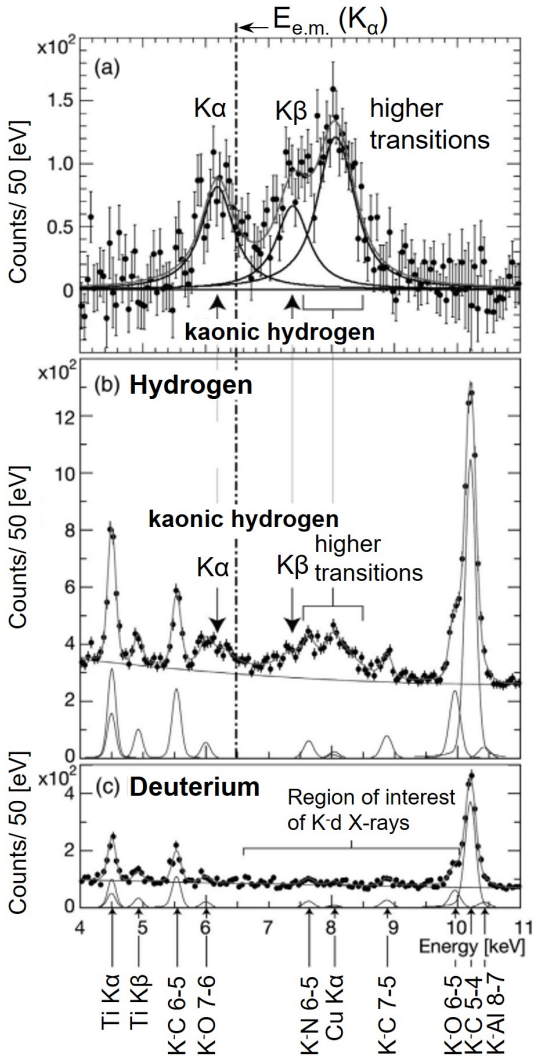

Figure 12: Global fit of the SIDDHARTA kaonic hydrogen and deuterium spectra. *(a)* Residuals of the kaonic hydrogen spectrum after subtraction of the background. *(b) and (c)* Kaonic hydrogen and deuterium X-ray spectra shown with the fit components. The dot-dashed line indicates the electromagnetic value of the K^-p K_α transition energy. *Adapted from [1].*

4.2.4 E62

The E62 collaboration at the Japan Proton Accelerator Research Complex (J-PARC), located in Tokai, Japan, performed a high-precision measurement of kaonic helium-3 and helium-4 X-ray transitions using superconducting microcalorimeters in 2018. A transition-edge sensor (TES) spectrometer with an energy resolution of 5.5 to 5.7 eV at 6.9 keV [4] was used for the detection of

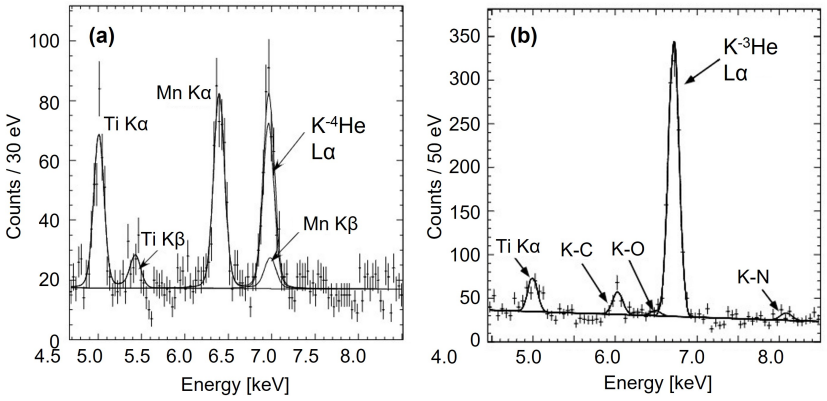

Figure 13: *(a):* X-ray energy spectrum for the kaonic helium-4 data obtained by SIDDHARTA. *From [2]. (b):* SIDDHARTA kaonic helium-3 X-ray energy spectrum. *From [67].*

the kaonic X-rays instead of SDDs. The working principle of a transition-edge sensor is based on the strong dependence of the electrical resistance on the temperature at the superconducting phase-transition. An incoming X-ray results in the generation of thermal energy, which can then be measured with high resolution. The experiment was located at the K1.8BR beam line and acquired data for 198 h for the liquid ^{4}He target and 149 h for the liquid ^{3}He target with a proton beam intensity of 51 kW. The charged kaons had a momentum of 900 MeV/c [4]. E62 employed an array of TES pixels for X-ray detection which was cooled down to 70 mK. The pixel structure of the detector was utilised to suppress background from charged particles which would induce a signal in several neighbouring pixels. The resulting X-ray energy spectra for both helium-3 and helium-4 targets are shown in Fig. 14.

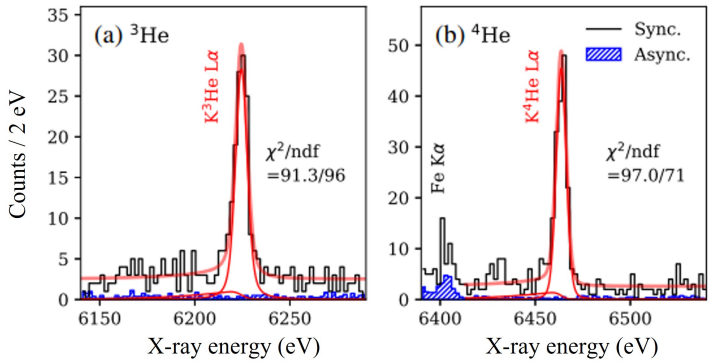

Figure 14: Fitted X-ray energy spectra obtained by E62 with a helium-3 target (*(a)*) and a helium-4 target (*(b)*). The asynchronous background is shown in blue. *Adapted from [4].*

The obtained energies of the $(3d \rightarrow 2p)$ transitions in kaonic helium-3 and helium-4 were determined to be $(6224.5 \pm 0.4_{\text{stat}} \pm 0.2_{\text{syst}})$ eV, and $(6463.7 \pm 0.3_{\text{stat}} \pm 0.1_{\text{syst}})$ eV, respectively [4]. The shift and width of the $2p$ level in

kaonic ^{3}He were found to be

$$\varepsilon_{2p,^3\mathrm{He}} = (-0.2 \pm 0.4_{\mathrm{stat}} \pm 0.3_{\mathrm{syst}})\ \mathrm{eV}, \tag{39}$$

$$\Gamma_{2p,^3\mathrm{He}} = (2.5 \pm 1.0_{\mathrm{stat}} \pm 0.4_{\mathrm{syst}})\ \mathrm{eV}, \tag{40}$$

and for kaonic ^{4}He

$$\varepsilon_{2p,^4\mathrm{He}} = (0.2 \pm 0.3_{\mathrm{stat}} \pm 0.2_{\mathrm{syst}})\ \mathrm{eV}, \tag{41}$$

$$\Gamma_{2p,^4\mathrm{He}} = (1.0 \pm 0.6_{\mathrm{stat}} \pm 0.3_{\mathrm{syst}})\ \mathrm{eV}, \tag{42}$$

representing the most precise measurements of the $(3d \rightarrow 2p)$ transition in both helium isotopes [4].

5 The SIDDHARTA-2 Experiment

The SIDDHARTA-2 experiment is located at the DAΦNE e^+e^- interaction point at INFN-LNF. As the successor of the SIDDHARTA experiment, its aim is to measure the ground state shift and width in kaonic deuterium atoms to enable the extraction of the isospin-dependent ($I = 0, I = 1$) $\overline{\mathrm{K}}\mathrm{N}$ scattering lengths a_0 and a_1. The X-ray spectroscopy of kaonic deuterium poses significant experimental challenges: the kaonic deuterium K_α X-ray yield is expected to be at least one order of magnitude lower than in kaonic hydrogen [68]–[71]. Additionally, the ground state width Γ_{1s} is expected to be larger than for $\mathrm{K}^-\mathrm{p}$ by a factor of two [33], [41]–[44]. Due to these challenges, the signal-to-background ratio of SIDDHARTA-2 has to be improved by at least a factor of ten from the SIDDHARTA ratio. Therefore, the experimental apparatus of SIDDHARTA-2 features several updates to achieve this increase of the signal-to-background ratio:

- a lightweight, cryogenic gaseous target cell,
- a system of newly developed, large-area X-ray detectors in the form of SDDs, and
- a two-stage veto system consisting of the Veto-1 and Veto-2 systems for the suppression of synchronous background.

The components of the apparatus are described in more detail in the following subsections.

5.1 The Experimental Apparatus

The SIDDHARTA-2 apparatus was installed at DAΦNE in 2019. A schematic drawing of the setup is shown in Fig. 15. A cylindrical vacuum chamber is placed above the IP of the DAΦNE collider, evacuated to a pressure of $\sim 10^{-7}$ mbar by a turbomolecular pump (Leybold TurboVac 350i) and a scroll pump. Like in previous experiments, a pair of 1.5 mm thick plastic scintillators read out by Photomultiplier Tubes (PMTs) placed approximately 12 cm below and above the IP acts as kaon trigger (KT) system by detecting the back-to-back charged kaon pairs. The KT scintillator has a size of $(100.0 \times 100.0 \times 1.5)$ mm^3. For a continuous monitoring of the beam quality and background levels, a luminosity monitor, the luminometer, is installed left and right of the beam pipe at the IP. It consists of two plastic scintillators with PMT read-out and has been realised and characterised by collaborators from the Jagiellonian University in Poland [73] (see Fig. 16). The luminometer provides Time-of-Flight (ToF) measurements to distinguish the charged kaons from Minimum Ionizing

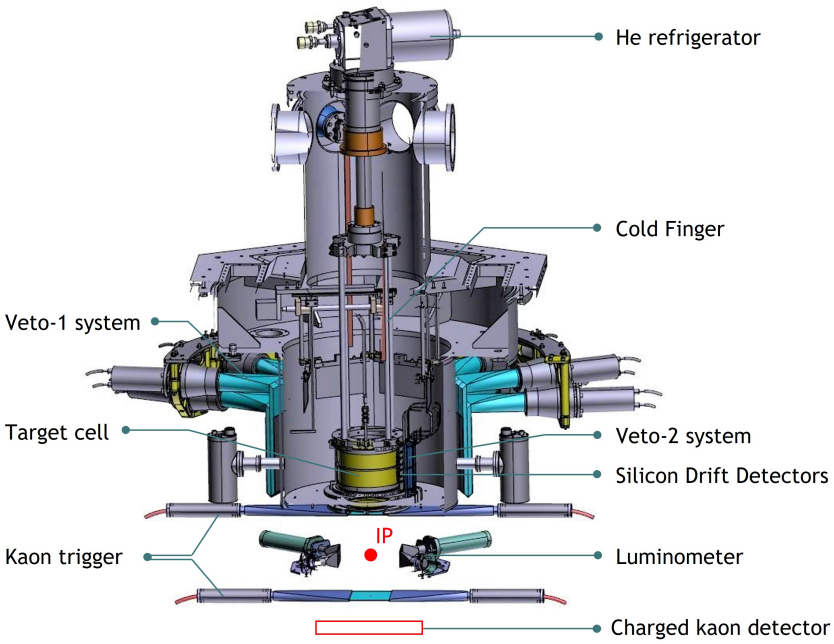

Figure 15: Schematic drawing of the SIDDHARTA-2 experimental apparatus. Its main components are the cryogenic target cell, the X-ray detection system, and the two-stage veto system for background suppression. *Adapted from [72].*

Particles (MIPs) on the horizontal plane. The beam luminosity is then derived from the ratio between the number of detected kaons and the product of the time of data acquisition, the cross section of the $e^+e^- \rightarrow \phi$ process, and the branching ratio of the $\phi \rightarrow K^+K^-$ decay [73].
A thin degrader is placed in front of the kaon entrance window of the vacuum chamber, slowing the kaons down in order to stop them in the target gas. It consists of several layers of Mylar foil, gradually increasing in thickness on one side to counteract the momentum boost of the kaons in direction of the centre of the collider ring. The degrader thickness was optimized during a commissioning run of SIDDHARTA (see Sec. 8.2). Inside the vacuum chamber, the kaonic atoms are formed in a cylindrical target cell which is kept at cryogenic temperatures (approximately 20 K to 30 K) by a closed-cycle helium refrigeration system (Oerlikon Leybold Vacuum Coolpower 10MD).
Surrounding the target cell, 48 arrays of SDDs are mounted for the detection of X-rays. Directly behind the SDDs the inner barrel of the two-stage veto system, the Veto-2, is installed. The other stage, the Veto-1, is installed outside of the vacuum chamber. As an additional measure for background minimisation another plastic scintillator with PMT read-out, the charged kaon detector, is placed below the bottom part of the kaon trigger. Its position in the apparatus is indicated by the red box in Fig. 15. A teflon absorber of 5 mm thickness coats the $(200 \times 200 \times 5)$ mm^3 scintillator on the top. The charged kaon detector rejects background events where a K^+ reached the target cell instead of

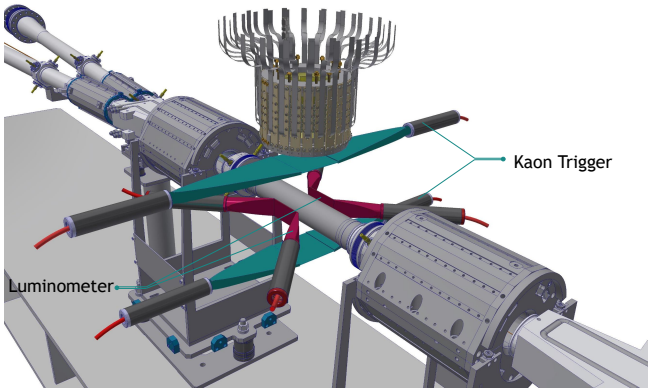

Figure 16: Schematic drawing of the target cell (yellow), kaon trigger (cyan) and luminometer (magenta) around the DAΦNE beam pipe interaction point. *Adapted from [72].*

a K^-. If a K^- stops in the charged kaon detector, a prompt emission of MIPs can be identified by timing information. A detailed description is given in Sec. 9.3.1.
On the middle flange of the vacuum chamber are the feedthroughs for the SDDs' and Veto-2's electronics. Lead walls next to and a lead table below the setup passively reduce background from beam losses and bremsstrahlung.

5.1.1 The Target Cell

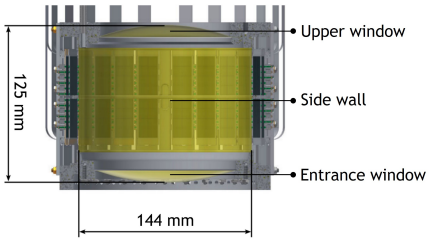

Figure 17: Schematic drawing of the SIDDHARTA-2 cryogenic target cell with a height of 125 mm and a diameter of 144 mm, surrounded by the SDD arrays. *Adapted from [51].*

The SIDDHARTA-2 target cell was constructed at the Stefan Meyer Institute (SMI) in Vienna. It has a cylindrical shape with a diameter of 144 mm and a height of 125 mm (see Fig 17). To allow for maximum transmission of X-rays to the SDDs, its sidewalls are made of two sheets of 75 µm Kapton polyimide ($C_{22}H_{10}N_2O_5$) foil glued together with epoxy adhesive, resulting in a total thickness of $\sim$ 150 µm, while its entrance window is made of 125 µm Kapton. Hence, approximately 87% of 8 keV X-rays are transmitted through the target cell sidewalls [74]. The upper window consists of titanium, and the remaining solid frames are made of high purity aluminium.

Since the reduction of the X-ray yield due to the Stark effect is an experimental challenge for the SIDDHARTA-2 experiment, a delicate balance has to be struck regarding the target gas density in terms of kaon stopping power and the influence of Stark mixing. The higher the gas density, the higher is the probability for an atom to feel the electric field of its neighbours, and thus for the Stark effect to facilitate the absorption of the kaon from a higher level [71], [75]. To achieve this balance, the target is kept at a cryogenic temperature of ~ 25 K, which allows for a pressure of ~ 1 bar.

5.1.2 The X-Ray Detection System

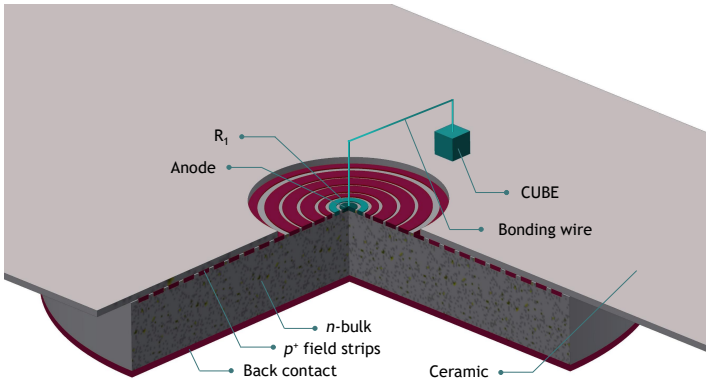

Figure 18: Schematic of the SDD chip structure. An n-type bulk is fully depleted by the potential created by the voltages applied to the p-type back contact and the p-type concentric strips on the other side. *Adapted from [76].*

Silicon Drift Detectors

Silicon drift detectors are semiconducting detectors initially proposed in the 1980s [78], [79] and now widely used for X-ray spectroscopy. An SDD chip consists of a fully depleted n-type silicon bulk. On one side of the chip, concentric rings of p^+-type strips are implemented with an n^+ collecting anode in the centre of the rings. On the other side, a non-structured p^+-type junction acts as radiation entrance window (see Fig. 18). A negative voltage with respect to the collecting anode is applied to the back contact. The p^+-rings on the other side are also biased negatively with progressively increasing bias from the first ring around the anode, R_1, to the outermost one, R_N. In this way, the n-bulk gets fully depleted and an electric potential is formed (see Fig. 19). When a particle enters the detector volume through the back contact, electron-hole pairs are created in the bulk and, due to the shape of the applied potential, the holes are guided towards the entrance window, while the electrons are collected at the anode. There they are converted into an analogue output signal. Each signal also provides a timestamp depending on the drift time of the electrons

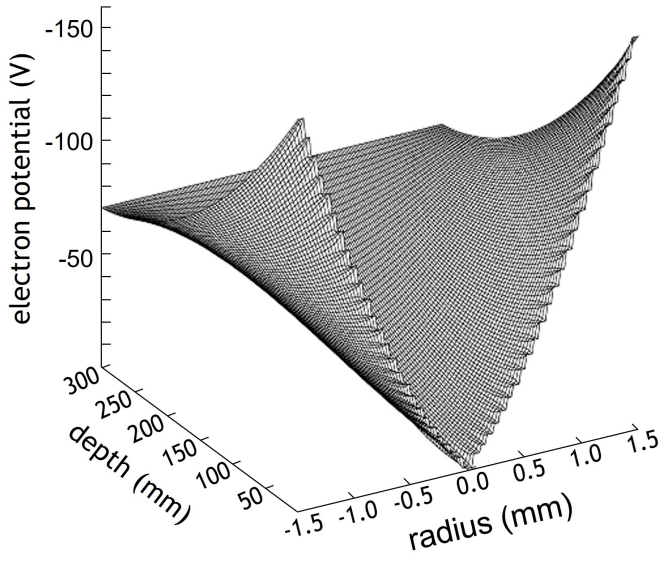

Figure 19: Shape of the potential created in an SDD chip, leading the electrons to the collecting anode. *Adapted from [77].*

to the anode. This is possible due to the small anode capacitance of the SDDs, which results in a lower rise time and higher amplitude of the signal and thus good resolutions in time and energy. For the kaonic hydrogen measurement of SIDDHARTA, an n-channel Junction-Gate Field-Effect Transistor (JFET) was implemented directly at the anode of the SDD chip to reduce intrinsic noise. For SIDDHARTA-2, new monolithic SDD chips were developed in a collaboration of Fondazione Bruno Kessler (FBK), Politechnico di Milano, INFN-LNF and SMI. Instead of the JFET, a Complementary Metal Oxide Semiconductor (CMOS) low-noise charge-sensitive preamplifier called *CUBE* is implemented [80]. The CUBE is not installed not directly at the anode, but at the chip's ceramic carrier structure and bonded to the anode with a 2 mm wire. The advantage of this configuration compared to the JFET configuration is the ability to cool the SDDs down to lower temperatures, which improves the timing capabilities and energy resolution, resulting in an average leakage current of 25 pA/cm^2 [80]. Previously, the optimal working temperature of the SDDs was $\sim$ 170 K, whereas now they can be operated at $\sim$ 120 K, improving the drift times from approximately 1 µs to $\sim$ 300 ns. Moreover, an issue faced during the SIDDHARTA beam time can be avoided with the new CMOS technology: during beam injection, when the background rates are high, the SDDs used to "latch-up" and needed to be manually recovered, which led to additional dead-time.

The SDD arrays for SIDDHARTA-2, shown in Fig. 20, consist of eight 450 µm thick cells, arranged in a 2×4 matrix. Each cell has an active area of (8×8) mm^2. They are mounted on a ceramic alumina carrier structure, whose geometry was optimized for a close packing of SDDs around the target cell to improve the active-to-total-area ratio to 80% [81]. For a periodic calibration

of the SDDs, two X-ray tubes are installed on opposite sides of the vacuum chamber (see Fig. 15), activating Ti and Cu foils mounted on the target cell. The fluorescence X-rays are detected by the SDDs and used for energy calibration. The SDD calibration process and characterisation are discussed in detail in Sec. 7.

Figure 20: SIDDHARTA-2 SDD array consisting of a 2×4 matrix of 450 µm thick SDD chips. The geometry of the ceramic carrier allows for a close packing around the target cell.

SFERA Boards

The SDDs' output signals are processed by dedicated Application Specific Integrated Circuit (ASIC) chips called SDD Front-End Readout ASIC (SFERA), developed by Politechnico di Milano. A SFERA consists of a 16-channel integrated circuit providing analogue shaping as well as peak detection of the signals of two SDD arrays. Each channel provides a 9th-order semi-Gaussian filter, pile-up rejection, a baseline-holder and a peak-sensing device. A peak stretcher holds the peak value of the SDD signal to be processed further by the SDD data acquisition (DAQ) system, which is described in Sec. 5.1.4. For every SDD hit, a real-time Low-Threshold (LT) signal is produced to trigger the SDD DAQ. Additionally, the DAQ is provided with the SDD's address and, in the case that the X-ray energy was higher than the maximum of the range of interest, with a High Threshold (HT) signal. The outputs are then connected to a multiplexer [82]. The SFERA block diagram and SDD read-out can be found in Appendix A (Fig. 85).

5.1.3 The Veto Systems

1. **The Veto-1 System**
   The purpose of the Veto-1 system is the suppression of synchronous background in the form of kaon stops not in the target gas, but in the surrounding setup material. This distinction can be achieved via timing information of the subsequently emitted MIPs in relation to the kaon trigger, since a kaon stop in a solid is much faster than in the target gas. Fig. 21 shows a GEANT4 (Geometry and Tracking 4) Monte Carlo (MC) simulated time spectrum of particles detected by a scintillator mounted outside the vacuum chamber with respect to the kaon trigger. The black

line corresponds to the time difference between a K^+K^- signal in the kaon trigger and a $\pi^\pm$ in the scintillator. The green and red curves show events in which either a K^+ or K^-, respectively, was detected in the bottom scintillator of the kaon trigger. Events in which neither charged kaon was detected in the bottom kaon trigger scintillator are shown in blue. In order to distinguish between kaon stops in the gas and stops in a solid, i.e. to resolve the left shoulder in the time spectrum from the main peak, a time resolution of < 1 ns is necessary.

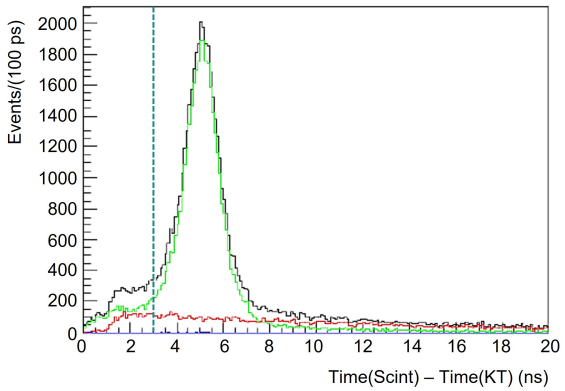

Figure 21: GEANT4 simulated timing spectrum for a scintillator installed outside the vacuum chamber. The green and red curves describe events in which a K^- or K^+ was detected in the bottom KT scintillator; the blue distribution shows events in which no charged kaon was detected. In black, the sum of these distributions is shown. The main peaks represents particles originating from the K^- absorption in gas. The dashed line represents the threshold between the kaon stops in gas and kaon stops in the slid structures. *Adapted from [83].*

The Veto-1 system consists of twelve units surrounding the outside of the vacuum chamber. Each unit is comprised of plastic scintillators read out by PMTs. To achieve the necessary time resolution to distinguish background from signal, the scintillators have to be read out on both ends. Since space around the vacuum chamber is limited, the units were designed in a complex shape (Fig. 22). The $(260 \times 110 \times 10)$ mm^3 plastic scintillator (EJ-200) of each unit is segmented into three strips of equal size. On one side, they are directly coupled to a PMT via a fishtail light guide. On the other end, the scintillators are cut into a 45° angle and coupled to aluminised mirrors, reflecting the light into three light guides. They are again connected to a PMT via a fishtail light guide. All parts are individually wrapped in mylar and the entire unit is made light-tight by black tape.
The Veto-1 system has been characterised at Paul Scherrer Institute (PSI) using a pion beam with a momentum of 170 MeV/c [83]. Two

fast plastic scintillators placed upstream of the Veto-1 prototype were used to define a trigger. A position scan was performed on the surface of the Veto-1 detector while data was acquired with a Time-to-Digital Converter (TDC). In this way, a time resolution of (746±53) ps (FWHM) was achieved. The detection efficiency was determined as the ratio between the number of particles detected in the Veto-1 prototype and the fast plastic scintillators. It was found to be $(96 \pm 2)\%$ [83].

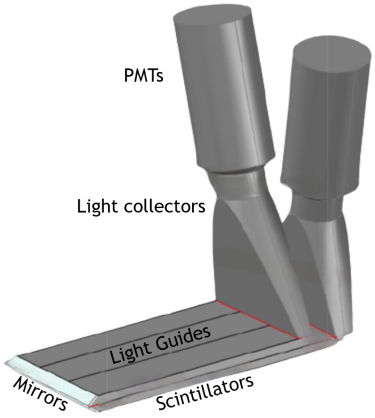

Figure 22: Veto-1 detector unit consisting of three strips of plastic scintillator, coupled to PMTs via light guides. *Adapted from [83].*

2. The Veto-2 System

Table 3: Absorption processes of the K^- on the nucleons with branching ratios [84]–[86].

Absorption process	Branching Ratio
$K^-n \to \Sigma^0\pi^-$	0.216
$K^-n \to \Sigma^-\pi^0$	0.216
$K^-n \to \Lambda\pi^-$	0.568
$K^-p \to \Sigma^+\pi^-$	0.446
$K^-p \to \Sigma^-\pi^+$	0.199
$K^-p \to \Sigma^0\pi^0$	0.303
$K^-p \to \Lambda\pi^0$	0.052

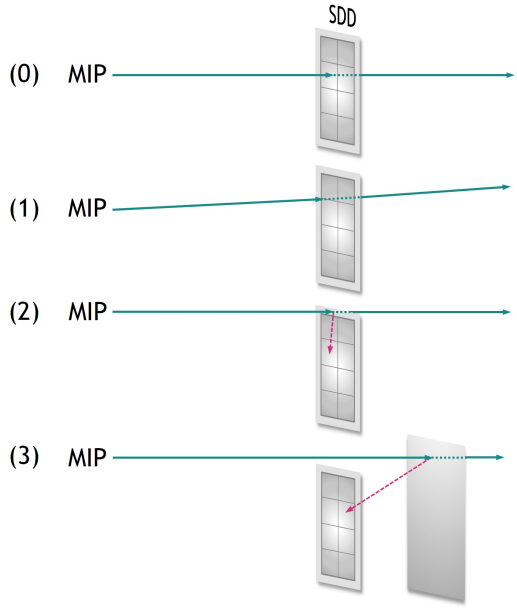

Figure 23: Motivation for the Veto-2 system. (0) Most frequently, the MIP passes the SDD through the centre of its active area, producing a large signal outside the ROI. (1) The MIP hits the SDD on the edge of its active area. (2) Delta rays (magenta) reach the SDD when the MIP traverses the ceramic carrier structure. (3) Backscattered electrons or secondary X-rays (magenta) from the surrounding setup hit the SDD. For cases (1) - (3), a signal in the ROI can be produced.

Table 4: Baryonic decay channels after nuclear kaon absorption with branching ratios [5].

Decay Channel	**Branching Ratio (%)**
$\Sigma^0 \rightarrow \Lambda\gamma$	100
$\Sigma^- \rightarrow n\pi^-$	9.848 ± 0.005
$\Sigma^+ \rightarrow p\pi^0$	51.57 ± 0.30
$\Sigma^+ \rightarrow n\pi^+$	48.31 ± 0.30
$\Lambda \rightarrow p\pi^-$	63.9 ± 0.5
$\Lambda \rightarrow n\pi^0$	35.8 ± 0.5

When the kaon is absorbed by the nucleons, MIPs - mainly protons and pions - as well as neutrons and gamma rays are emitted as decay products of the absorption and decay channels listed in Tables 3 and 4. Depending on where these MIPs traverse the SDDs, a background signal in the region of interest (ROI) of SIDDHARTA-2 from 6 - 15 keV can be produced, mimicking a K^-d X-ray. Fig. 23 shows the different cases for which this can occur. To reject those signals, the spatial correlation between signals in the SDDs and signals in the Veto-2 counters is used. Therefore, the Veto-2 system is mounted directly behind the SDDs to

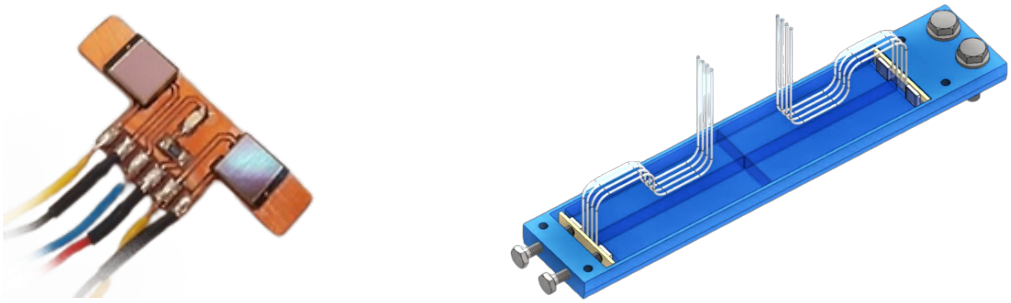

(a) Print board with two (4×4) mm^2 SiPMs. A blue LED is mounted in-between them for in-situ calibration of the system.

(b) Schematic view of a Veto-2 unit consisting of four scintillators and SiPMs, together with two LEDs. *From [76].*

Figure 24: Components of the Veto-2 detector system.

achieve the necessary spatial resolution.

The Veto-2 system consists of 24 units of four detectors each, resulting in 96 read-out channels. Each detector is comprised of a $(50 \times 12 \times 5)$ mm^3 plastic scintillator (EJ-200, peak emission wavelength 425 nm [87]) and a (4×4) mm^2 Near-Ultraviolet (NUV) Silicon Photomultiplier (SiPM) by AdvanSiD. They consist of 9340 40 µm microcells, with a geometrical fill factor of 60%, a typical breakdown voltage of 26 V, and a peak sensitivity wavelength of 420 nm to match the scintillators' emission [88]. The SiPMs, held in place by nylon screws, are coupled to the scintillators via optical grease (Saint Gobain BC-630). Four channels are placed together in a 3D-printed, black box made of acrylonitrile butadiene styrene (ABS) (see Fig. 24b). The SiPMs on one side of the unit share the same print board, and have a blue light-emitting diode (LED) placed in-between them for in-situ calibration of the detectors, as shown in Fig. 24a. The LEDs have a dominant emission wavelength of 465 nm [89] and are operated in pulsed mode. A group of eight LEDs is supplied by one pulse generator with bias voltage; a 22 Ω resistor is installed serially to each LED. The pulsers were developed at SMI and provide a positive voltage pulse with a frequency of 100 Hz and an adjustable width of either 28 or 126 ns for the LEDs and a Transistor-Transistor Logic (TTL) and Nuclear Instrumentation Module (NIM) pulse as start signal. The Veto-2 calibration procedure is described in depth in Sec. 6.3. The SiPMs' signals are transported to the front-end electronics over twisted-pair cables with a length of ~ 70 cm.

Silicon Photomultipliers

SiPMs were developed at the beginning of the twenty-first century and are today widely used in research and industry due to their favourable properties [90]. They provide a high internal gain comparable to PMTs at low bias voltages, are able to detect single photons and are not in-

fluenced by magnetic fields. A SiPM consists of an array of parallely connected microcells (Fig. 25a), each comprised of a single-photon avalanche photodiode (SPAD) operated at reverse bias voltages above the breakdown voltage (Geiger-mode), and a quenching resistor. The structure of a SPAD is based on "*pin*" diodes, i.e. junctures of a n-doped, an intrinsically p-doped (p_i) and a p-doped layer. SPADs have an additional highly doped layer as multiplication zone, in which the avalanche effect responsible for the SiPM's internal gain takes place. A typical configuration of a blue-light sensitive SPAD is n^+-p^+-p_i-p^+ (Fig. 25b).
When photons hit a microcell i, the SPAD goes into breakdown and a signal with an amplitude A_i is produced. This pulse height depends on the capacitance C of the microcell and the applied overvoltage, i.e. the voltage above the breakdown voltage V_B: $A_i \sim C(V - V_B)$. A SiPM can be seen as a digital detector, since the final output signal has an amplitude A of the sum of all pulses of pixels in breakdown: $A = \sum_i A_i$ [90].

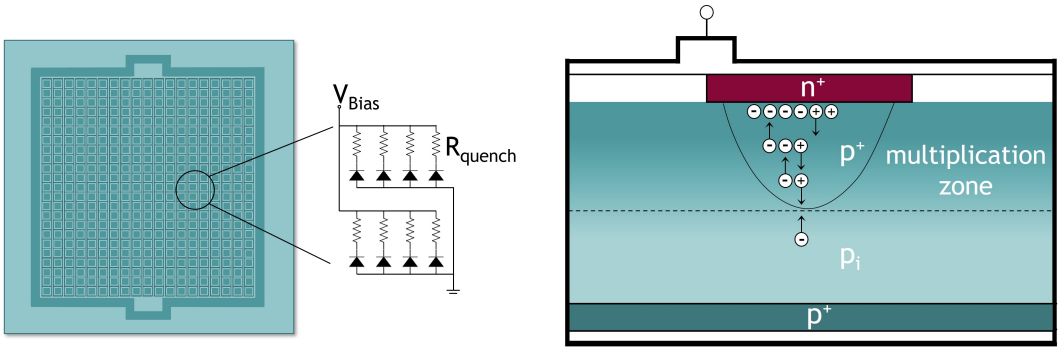

(a) Schematic of the array structure of a SiPM. Each Pixel contains a SPAD and a quenching resistor.

(b) Typical n^+-p^+-p_i-p^+ structure of a SPAD with the multiplication zone for internal gain.

Figure 25: Structural schematics of a SiPM and one of its building blocks, the SPAD.

After the discharge, the microcell is quickly restored to its initial state by the quenching resistor and hence prepared for the detection of the next photon. Table 5 lists typical values of the most important operation properties of SiPMs.

Table 5: Typical values for the defining properties of SiPMs.

SiPM Properties	
Internal gain	$10^5 - 10^7$ [90]
Breakdown Voltage (V)	$25 - 50$ [91]
Photon Detection Efficiency (%)	up to 50 [91]
Response Time (ns)	< 1 [91]
Dark Count Rate (kHz mm^2)	10-100 (at room temperature) [91]

Amplification Boards

For the supply of the bias voltage as well as the amplification and processing of the SiPMs' signals, dedicated front-end electronic boards were developed at SMI (Fig. 26) [92]. They feature 16 input channels and a total of 32 output channels: 16 analogue outputs together with 16 digital output channels. The SiPMs are biased via the input channels by so-called High-Voltage (HV) modules, able to supply voltages of up to 70 V. The overvoltage for each SiPM can be manually adjusted on the HV modules with a potentiometer. The modules were modified into constant voltage sources instead of constant current sources; the reason for this and details are described in Sec. 6.2.2. Per input channel, two outputs are available: the amplified analogue SiPM signal pulse provided as a differential signal, and a digital Low-Voltage Differential Signal (LVDS) in the form of a NIM pulse, representing the Time-over-Threshold (ToT) of the analogue signal. The gain for the analogue pulse and the voltage threshold for the ToT signal are both adjustable remotely over Universal Serial Bus (USB) using a Graphical User Interface (GUI) loaded onto the on-board arduino chip. Once adjusted, the configuration can be saved onto the Electrically Erasable Programmable Read-Only Memory (EEPROM) chip and loaded even after disconnecting the boards from their power supply. The GUI is shown in Fig. 27.

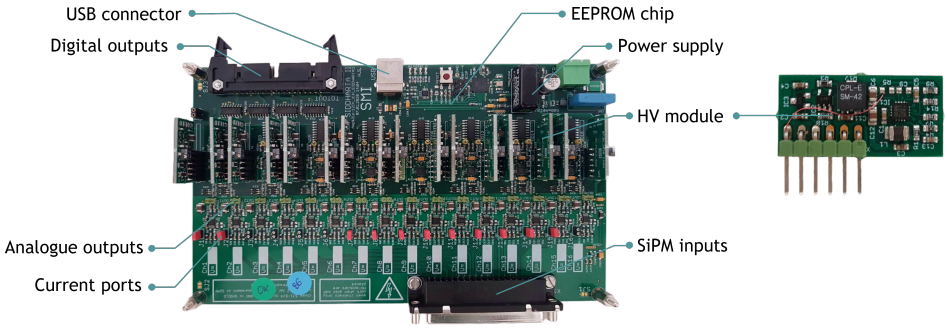

Figure 26: 16-channel Veto-2 amplification board for SIDDHARTA-2. On the right, a single HV module is shown.

5.1.4 The Data Acquisition System

The SIDDHARTA-2 DAQ system consists of a National Instruments (NI) Peripheral Component Interconnect (PCI) bus and handles the communication of the SFERAs and kaon trigger, the timing information, and is responsible for the final construction of an event. Fig. 28 sketches the DAQ flow for one bus; in total, six buses are used. The SDDs and kaon trigger do not share a universal trigger. Hence, two independent FPGA (Field Programmable Gate Array) loops are employed. One is responsible for the kaon trigger, while the

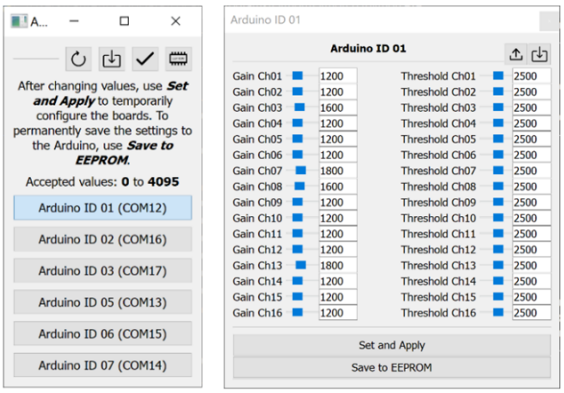

Figure 27: GUI to configure the values for gain and threshold for each channel of the Veto-2 amplification board *From [93].*

other waits for an LT signal on the SDDs' Digital Output (D.O.) line (shown in cyan in Fig. 28) and triggers the SDD DAQ as soon as an LT signal is detected. In this instance, the trigger time is subtracted from the FPGA on-board clock counter value, resulting in the drift time (DT). Then, the timing information is transferred to the ADC (Analogue-to-Digital Converter) board, and the Acknowledge (ACK) signal is set to high. Next, the digital address readout by the same ADC board is clocked, the ACK is set to low again and a Master Reset (MR) is set. Finally, the loop is back in edge-sensing waiting mode. For the FPGAs, the models NI PCI-7813 and NI PCIe-7822 are used. The SDDs' analogue outputs (A.O.) are sampled ten times by the ADC (NI PCI-6115) to avoid any influence of digital noise. The signals of the Veto-1 and Veto-2 are acquired by a VME (Versa Module Eurocard) TDC. For the Veto-2, the digital ToT signal is recorded by a CAEN V1190A 128 channel multihit TDC.

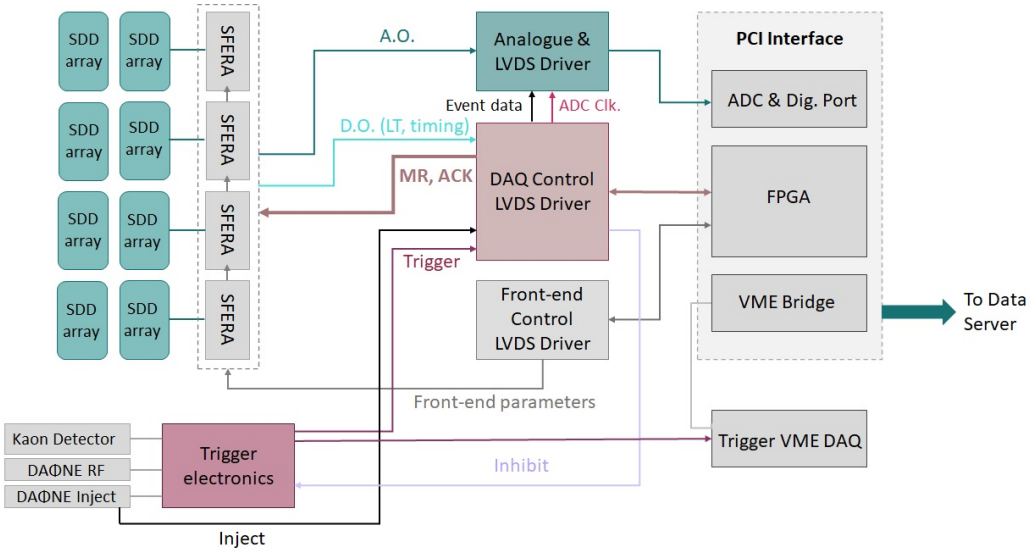

Figure 28: Data flow chart for one bus of the SIDDHARTA-2 DAQ.

6 The Veto-2 System

The motivation for the implementation and the setup of the Veto-2 system have already been described in the previous section 5.1.3. Here, the characteristics of the system, which have been studied in the laboratory at SMI in Vienna, as well as updates to the design, necessary due to the challenging conditions in the DAΦNE hall, will be described.

6.1 Characterisation at SMI

The first version of the Veto-2 system was built in 2018 at SMI. Before installation in the SIDDHARTA-2 apparatus at LNF, it was tested and characterised in Vienna in the framework of a master thesis [94]. The most important characteristics are discussed in the following subsections.

6.1.1 Time Resolution

Figure 29: Irradiation positions on the scintillator (SiPM on the left, top view) to determine the time resolution of the Veto-2 system.

The time resolution of the Veto-2 system was determined by irradiating the Veto-2 SiPM-scintillator tiles with a 450 nm wavelength laser diode. The laser was operated in a pulsed mode at a frequency of 230 Hz. The procedure is described in detail in [94], [95]. In this way, the scintillators were irradiated on several different positions (see Fig. 29) and the time delay between the laser pulse and the SiPM signal was measured for each position. A Gaussian fit was applied to the obtained timing distributions, and the Full Width at Half Maximum (FWHM) of the distribution represented the detector's local time resolution for this position (see Fig. 30). A comparison of the resolutions for the different positions on one scintillator tile provided a measure of quality in terms of construction of the Veto-2 detector.
Since the scintillators are read out on only one side, the path length of the light through the scintillator has to be taken into account in the determination of the time resolution. In this way, the average time resolution of the Veto-2 system was found to be (293 ± 45) ps [94]. In Sec. 5.1.3 it was mentioned that a time resolution of < 1 ns is necessary to distinguish between kaon stops in the target gas and in the solid materials present in the setup, and hence to

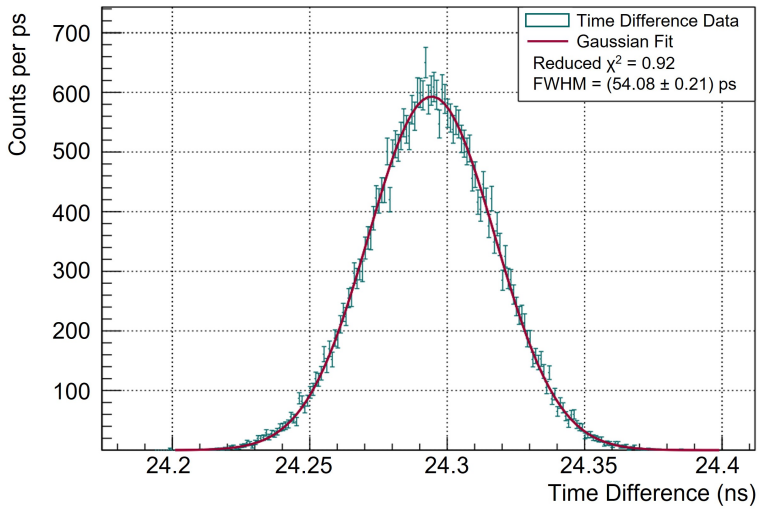

Figure 30: Time difference between laser pulse and SiPM signal for the central position on one scintillator, with Gaussian fit to determine the local time resolution for this position.

eliminate another component of the synchronous background. Since the Veto-2 system fulfils this requirement, it can be used analogously to the Veto-1 system in addition to its original purpose of suppressing MIP related background, as presented in Sec. 9.3.2.

6.1.2 Detection Efficiency

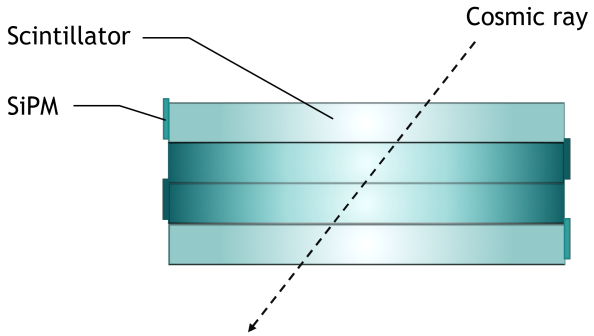

Figure 31: Configuration of scintillators to measure the Veto-2 detection efficiency with cosmic rays.

The detection efficiency of the Veto-2 system was measured at SMI using cosmic rays. Four scintillator tiles with SiPM readout were stacked vertically as shown in Fig. 31. On the condition of a coincidence in signals in the two outermost detectors, the number of events in the two inner ones was counted.

The pulse height spectra of all four detectors were acquired over a period of four days (see Fig.). A detailed description of the setup, data acquisition and analysis is given in [94], [95]. Since the amplified analogue SiPM signals induced by cosmic rays (and MIPs as expected for the SIDDHARTA-2 experiment) are expected to have large pulse heights of a few hundreds of mV, a threshold of 400 mV was set for the outermost detectors of the stack to determine the detection efficiency. For the inner detectors, the threshold was set at 300 mV to account for the possibility of imperfect alignment of the detectors. Fig. 32 shows the four obtained pulse height spectra, where only the 400-mV threshold to the outermost detectors was applied. With this setup, detection efficiencies of $(99.05 \pm 0.14)\%$ and $(99.14 \pm 0.14)\%$ were determined for the two inner Veto-2 detectors [94], [95].

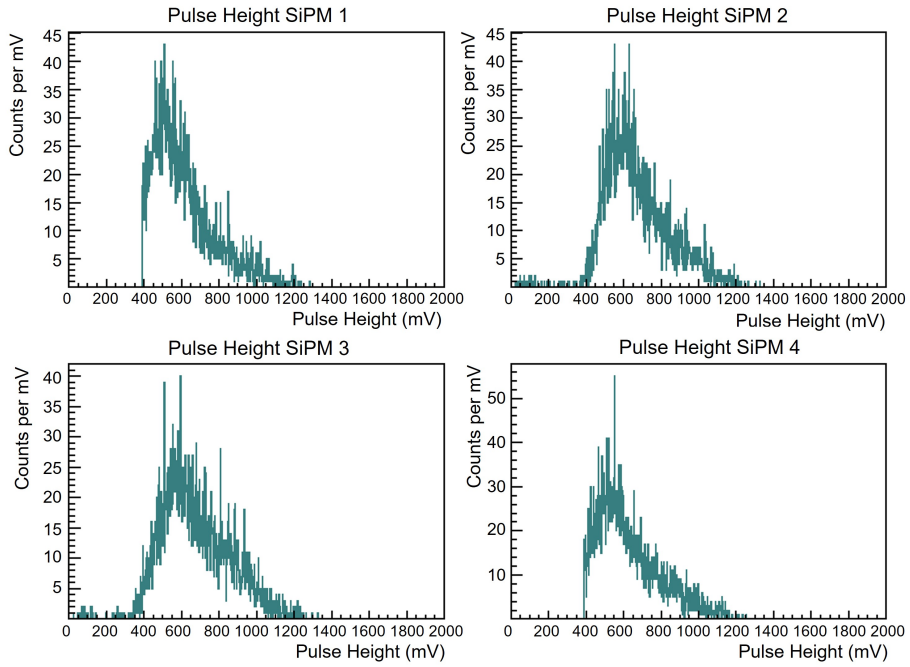

Figure 32: Pulse height spectra of the four SiPMs obtained with cosmic rays. SiPMs 1 and 4 are the two outermost ones, with a visible threshold at 400 mV. The SiPMs 2 and 3 are the inner detectors. *Adapted from [94].*

6.2 Dealing with Radiation Damage

After the construction and characterisation of the first version of the Veto-2 system, three detector units (i.e. twelve detector channels) were installed in the SIDDHARTA-2 apparatus at DAΦNE in April 2019 for commissioning. During this time, the beam quality was still under optimisation and a high

level of background and particle losses by the beams were prevalent. After approximately six months, the Veto-2 detectors' response had visibly changed, i.e. the pulse height of the analogue SiPM signals had significantly decreased, whereas the dark current had increased without change of the gain settings. The detectors were removed from the setup and brought back to SMI for characterisation of the changes and identification of their cause, where it was concluded that the detectors had suffered from radiation damage in the collider environment.

6.2.1 Characterisation of Damage

1. *I-V* **Curves**

   During their operation in the SIDDHARTA-2 apparatus, a steep increase in dark currents was observed for all Veto-2 detectors, without any changes on the gain settings on the amplification boards. Therefore, the Veto-2 detectors were removed from the apparatus and returned to Vienna for observation. To quantify this increase, the current-voltage curves were measured for twelve Veto-2 channels previously installed at LNF, as well as three new detectors which were never in the DAΦNE collider hall.

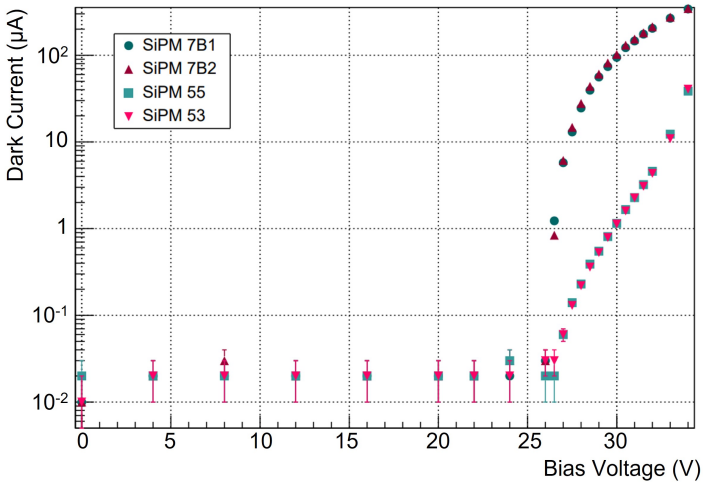

Figure 33: *I-V* curves for two damaged Veto-2 detectors (SiPM 7B1 and SiPM 7B2) as well as two intact ones (SiPMs 53 and 55), measured in Feb 2020. The leakage current at equal bias voltage for the damaged detectors is visibly higher compared to the intact ones.

For increasing bias voltage V, the dark current I was measured for each SiPM; the bias voltage was supplied by a Keithley 617 Programmable Electrometer voltage supply, and the current measurement was performed with a Fluke 287 multimeter. Conservatively, the resolution

of the multimeter was assigned as systematic uncertainty to the current measurements; the accuracy of the electrometer of 10 mV was taken into account for the applied voltages. The analysis of all data obtained during the work on this thesis was performed with the ROOT framework [96], [97] and C++.

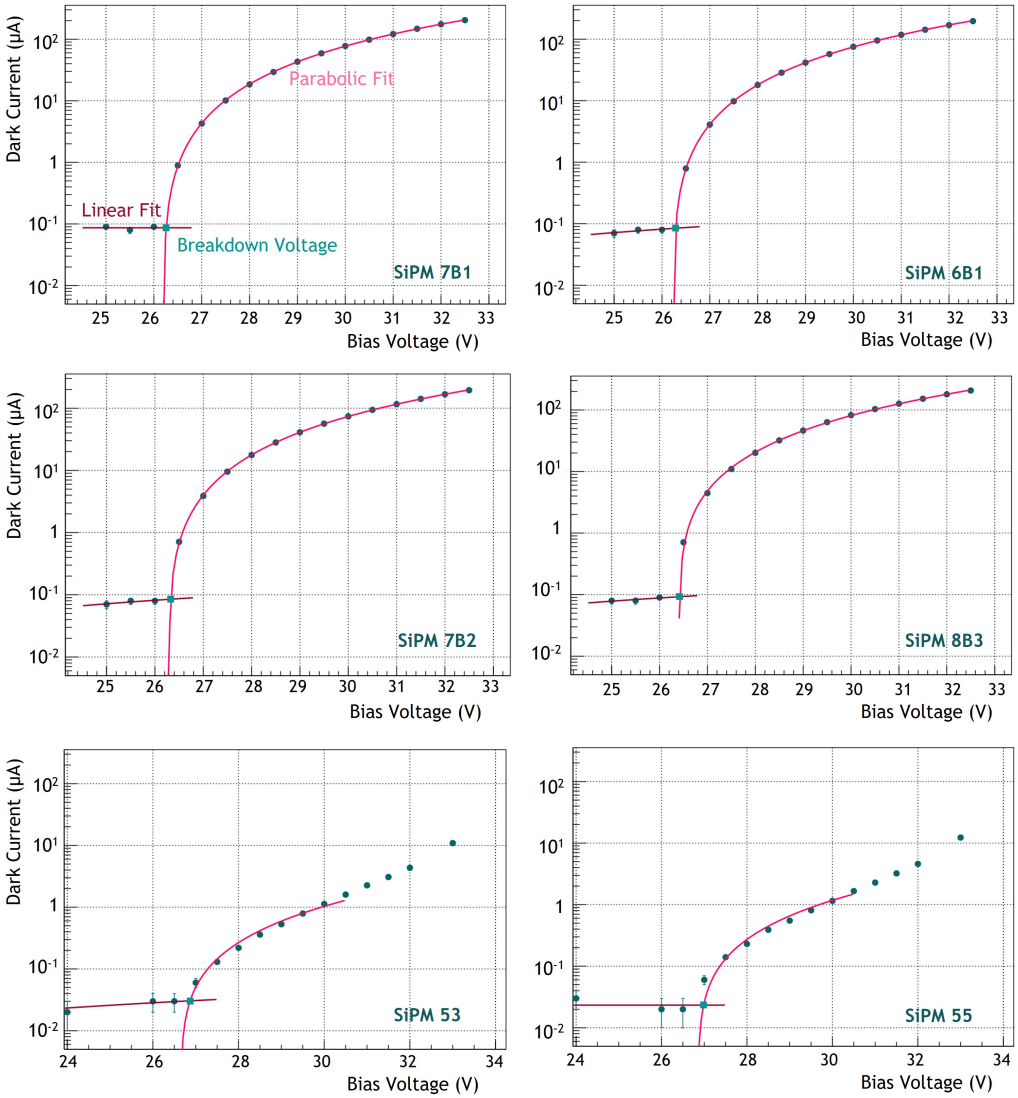

Figure 34: *I-V* curves for four damaged Veto-2 detectors (SiPMs 7B1, 6B1, 7B2, and 8B1) as well as two intact ones (SiPMs 53 and 55). A linear fit was applied to the voltage region below the breakdown voltage, and a parabolic fit was performed on the data above breakdown. The intersection of the two fit functions represents the breakdown voltage for this SiPM.

Fig. 33 shows the observed *I-V* curves for two damaged detectors (SiPM 7B1 and SiPM 7B2) together with two intact detectors (SiPMs 53 and 55). These curves were measured in February 2020. For a bias voltage

of 30 V, the dark current for the damaged detectors is higher by a factor of ~ 100 compared to SiPMs 55 and 53.
The I-V curves were again measured in October 2020 for the damaged detectors, as shown in Fig. 34. The top four panels show I-V curves for damaged detectors (SiPMs 7B1, 6B1, 7B2, and 8B3), the bottom two panels for the intact SiPMs 53 and 55. Now, the factor of increase in leakage current for the damaged detectors compared to the intact ones for a bias voltage of 30 V had decreased to ~ 80, suggesting a possible partial recovery of the SiPMs over time. To determine the breakdown voltage for each SiPM, a linear fit was applied to the data in the region below breakdown. The data above breakdown was fitted with a parabola; the breakdown voltage is given by the point of intersection of the two functions. The observed values are listed in Table 6, for the damaged SiPMs 6B1 to 8B4, and the intact ones 52 to 55. The systematic uncertainty was derived from the fit function using Gaussian propagation of errors. On average, the breakdown voltage for intact SiPMs was (26.8 ± 4.3) V, whereas the average value for the irradiated SiPMs was (26.4 ± 4.9) V. The two values are in agreement within one standard deviation, thus no change on the breakdown voltage due to radiation damage could be observed.

Table 6: Breakdown Voltages of Veto-2 Detectors with (*top*) and without irradiation (*bottom*) in the DAΦNE hall with the respective mean values for both groups.

SiPM Number	**Breakdown Voltage (V)**
6B1	26.29 ± 2.07
6B2	26.37 ± 1.66
6B3	26.42 ± 0.61
6B4	26.45 ± 0.54
7B1	26.26 ± 1.75
7B2	26.33 ± 1.11
7B3	26.45 ± 1.60
7B4	26.38 ± 0.59
8B1	26.39 ± 2.92
8B2	26.39 ± 0.26
8B3	26.42 ± 0.34
8B4	26.42 ± 0.56
Mean	26.40 ± 4.88
52	26.87 ± 1.99
53	26.99 ± 2.79
55	26.55 ± 2.51
Mean	26.80 ± 4.25

The increase in leakage current of the SiPMs as well as the possible partial recovery after time both hint towards exposure to radiation as the cause for the damage of the detectors. The irradiation with high energy electrons, protons, pions or photons can induce damage to the silicon bulk of the SiPM due to displacement of atoms in the silicon lattice. On a macroscopic level, this can lead to an increase of the detector's Dark Count Rate (DCR) and thus its leakage current, due to the thermal excitation of defects close to the middle of the silicon band gap [98]. On the other hand, bulk damage in silicon detectors can, over time, partially recover due to self-annealing even at room temperature. Hence, these first observations strongly hint toward radiation damage of the Veto-2 detectors during the DAΦNE commissioning.

2. **Pulse Heights**

A few months after installation in the SIDDHARTA-2 apparatus in the DAΦNE hall, in addition to the changes in dark currents, the pulse heights of the analogue SiPM signals noticeably decreased. Although no changes were made in the gain settings of the Veto-2 system's amplification boards, the signal amplitudes decreased to a level at which they were no longer distinguishable from thermal noise. Back at SMI in Vienna, pulse height spectra were measured for damaged (SiPM 7B4) and intact (SiPM 55) SiPMs with a ^{22}Na source. The amplification boards were set to a bias voltage of $\sim$ 31.5 V for both detectors to enable a direct comparison of signal amplitudes; this corresponded to a dark current of 183.08 µA for SiPM 7B4, and 3.22 µA for SiPM 55. For amplification of the SiPM signals, the predecessor of the current 16 channel amplification boards for SIDDHARTA-2 was used. It featured twelve analogue and ToT channels and its structure was equivalent to the 16 channel boards used now. The oscilloscope's (LeCroy WavePro 760 Zi-A) measurement tool was used to measure the detectors' negative voltage pulse minima and store the data in histograms.
The pulse height spectra for both SiPMs are shown in Fig. 35. For SiPM 55, the two Compton edges of the 511 keV and 1275 keV gamma rays emitted in the β^+-decay of ^{22}Na are clearly visible and located at approximately 150 mV and 450 mV, respectively. This is not true for the damaged SiPM; no Compton edges are visible, since the pulse heights are too low to be distinguishable from thermal noise.
The decline in pulse heights of the analogue SiPM signals strengthens the hypothesis of radiation damage to the Veto-2 detectors installed in the SIDDHARTA-2 apparatus. Defects in the silicon bulk act as trapping centres for charge carriers. Depending on their distance from the valence and conduction band edges, the trapping time can be too long for the charge carriers to contribute to the SiPM output signal [98], thus reducing its pulse height.

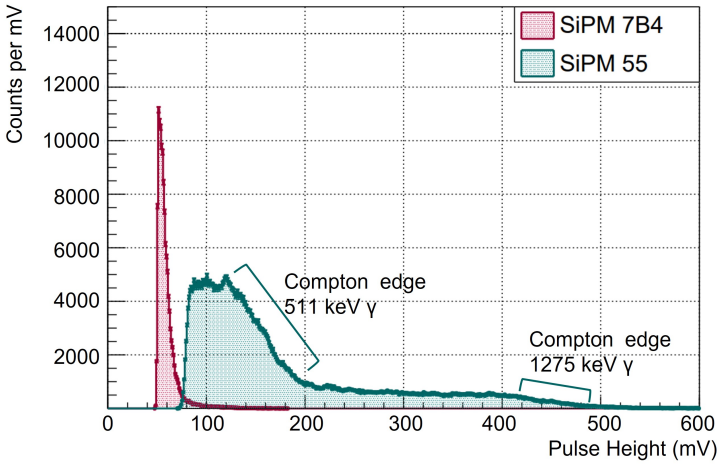

Figure 35: Pulse height spectra for a damaged detector (SiPM 7B4, magenta) and an intact one (SiPM 55, cyan) for equal overvoltage.

3. Laser Tests

To exclude other possible reasons for the damage to the Veto-2 detectors, more tests were performed. One possible hypothesis was impairment of the SiPMs due to the high particle rates during beam losses or beam injection. A high incident particle rate would result in a high number of photons being produced in the detector, and subsequently in high currents possibly able to damage the microcells' quenching resistors. This would lead to a short circuit in the microcells and hence high leakage currents.

In order to simulate a high rate and intensity of incident particles in the DAΦNE hall, an intact SiPM was irradiated with a pulsed picosecond injection laser from Advanced Laser Diode Systems with a wavelength of 404 nm. The laser pulse height, pulse frequency f, and pulse length were varied (see Table 7) and the SiPM's analogue output signals were monitored on a LeCroy WavePro 760 Zi-A oscilloscope. For amplification, the twelve channel amplification boards described above were used. The detector's leakage current I_D was observed with a Fluke-287 multimeter. Fig. 36 shows the laser trigger pulse (yellow) and SiPM output signal (pink) on the oscilloscope for a laser pulse height of 2.7 V as a reference for "normal operation". The detector is not in saturation with an average pulse height of ~ -480 mV and has a dark current of 2.5 µA. Fig. 37 shows the extreme case for a laser pulse height of 4 V and a pulse frequency of 20 kHz. The SiPM is fully saturated and its output signal has an average pulse height of approximately -940 mV.

Table 7: Configuration of the pulsed laser irradiating a SiPM to simulate a high rate and intensity of incident particles, as well as the resulting dark current of the SiPM.

Pulse Height (V)	f (kHz)	Pulse Width (ns)	I_D (µA)
2.7	0.1	1.5	2.5
4.0	0.1	10.0	3.0
4.0	10.0	10.0	64.8
4.0	20.0	10.0	124.6
5.0	0.1	10.0	3.1

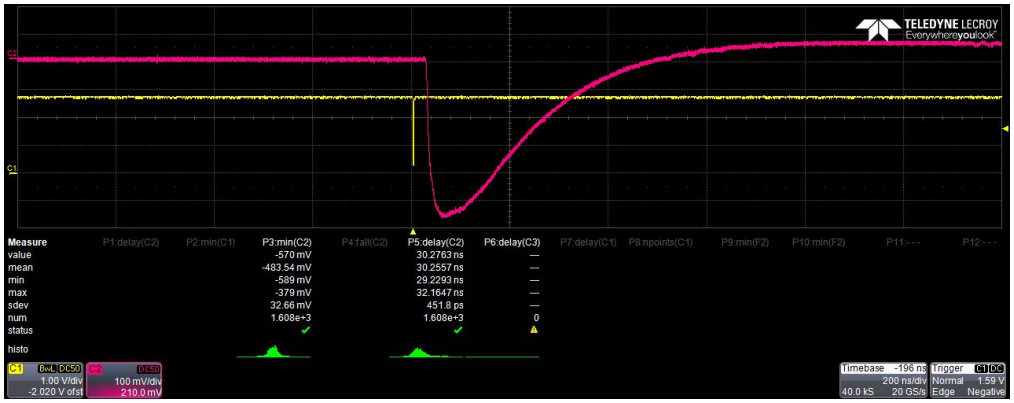

Figure 36: Oscilloscope screenshot showing the SiPM in "normal operation", i.e. not in saturation (pink signal) with a trigger pulse from the laser (yellow). The laser pulse height was 2.7 V at a pulse frequency of 100 Hz.

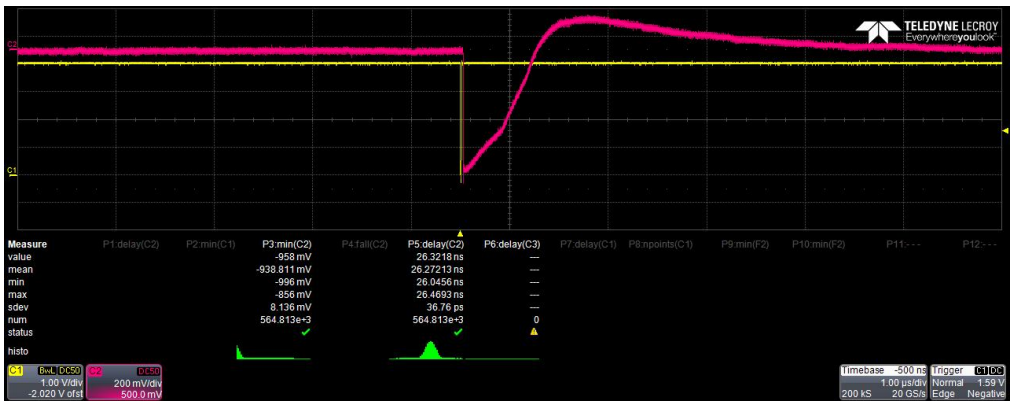

Figure 37: Oscilloscope screenshot with the SiPM signal (pink) and a trigger pulse provided by the laser (yellow). The laser pulse height was 4.0 V at a pulse frequency of 20 kHz.

In this extreme configuration, the detector was irradiated for 83 minutes and its performance was monitored; however, the height of the SiPM output signal and its dark current both remained unchanged during the irradiation and no effect on the signal amplitude or dark current were

observed.
In conclusion, the direct irradiation with the pulsed laser did not infer damage to the SiPM. However, this may not be an ideal simulation of the conditions during the injection phase of DAΦNE or during beam losses. With the laser, a constant number of photons equally distributed over the time of the pulse width is periodically hitting the detector. In the apparatus, an instant shower of 10^9 particles can hit the SiPMs of the Veto-2 system. These conditions could not be simulated at SMI. Nevertheless, the hypothesis of radiation damage as the cause of the SiPMs' declining performance is the most probable as suggested by the other characterisation measurements described.

4. **Annealing Attempt**

As final evidence of radiation damage, an attempt to anneal the damaged detectors was performed. Therefore, three of the detectors previously installed in the SIDDHARTA-2 apparatus (SiPMs 6B1, 7B1 and 8B1) were placed in a climate chamber of the type Vötsch VT 7021 at a temperature of 70°C for a duration of approximately 40 hours. For comparison, the pulse height spectra obtained with a collimated ^{22}Na source were measured for each detector before and after the annealing process. The dark currents of the detectors 6B1, 7B1, and 8B1 were set to 48.6 μA, 48.9 μA, and 48.7 μA, respectively. For each detector with a visible Compton edge in the spectrum, a fit was applied to the pulse height spectra to determine the pulse height of the Compton edge from the ^{22}Na 1275 keV γ-ray at 1061 keV. The detectors' response function was modelled as described in [99], as a convolution of a Gaussian function and the complementary error function. The pulse height value of the Compton edge was left as a free parameter in the fit. The fitted spectra before and after the annealing process for SiPMs 7B1 and 8B1 are shown in Fig. 38. Table 8 lists the Compton edge pulse height values for the two SiPMs 7B1 and 8B1; for 6B1, the Compton edge was not visible in the spectrum and thus the response function fit could not be applied. Additionally, the relative differences between the values pre- and post-annealing for each SiPM are listed. The statistical uncertainty of the pulse height value is given by the uncertainty of the fit and rounded to three digits conservatively. The uncertainty of the relative differences was calculated via Gaussian error propagation.
The pulse height spectra already show a slight visible improvement after the annealing of the detectors, as the maximum pulse heights are larger in the post-annealing spectra. This is particularly apparent for SiPM 7B1, and is mirrored in the fit results for the Compton edge pulse heights. For both SiPMs, the Compton edge appears at a larger pulse height after the annealing procedure. Although this improvement is only marginal and the detectors have not been restored to their intact state (in

fact, the Compton edge is still only barely visible for SiPM 7B1), it further indicates radiation damage in the silicon bulk as cause for the decline in detector performance. An improvement of $\sim 14\%$ and $\sim 5\%$ was achieved for the two detectors respectively, despite the suboptimal conditions for the annealing; ideally, the annealing temperature should have been higher and the exposure time longer: Tsang, T. *et al.* (2016) found a linear relation between the effectiveness of annealing and the temperature, and an exponential relation to the exposure time [100]. A higher temperature was not possible in this instance due to the fact that the SiPMs were glued to the scintillators, whose softening point is given at 75°C [87]. The annealing attempt was, however, not performed to restore the detectors, but as an additional tool to characterise their damage.

Table 8: Pulse height values of the 1061 keV Compton edge of ^{22}Na for the damaged Veto-2 detectors 7B1 and 8B1 before and after the annealing process.

	SiPM	**Compton Edge (mV)**	**Rel. Difference (%)**
before	7B1	34.469 ± 0.010	
after	7B1	39.437 ± 0.010	14.415 ± 0.017
before	8B1	39.862 ± 0.010	
after	8B1	41.910 ± 0.010	5.137 ± 0.010

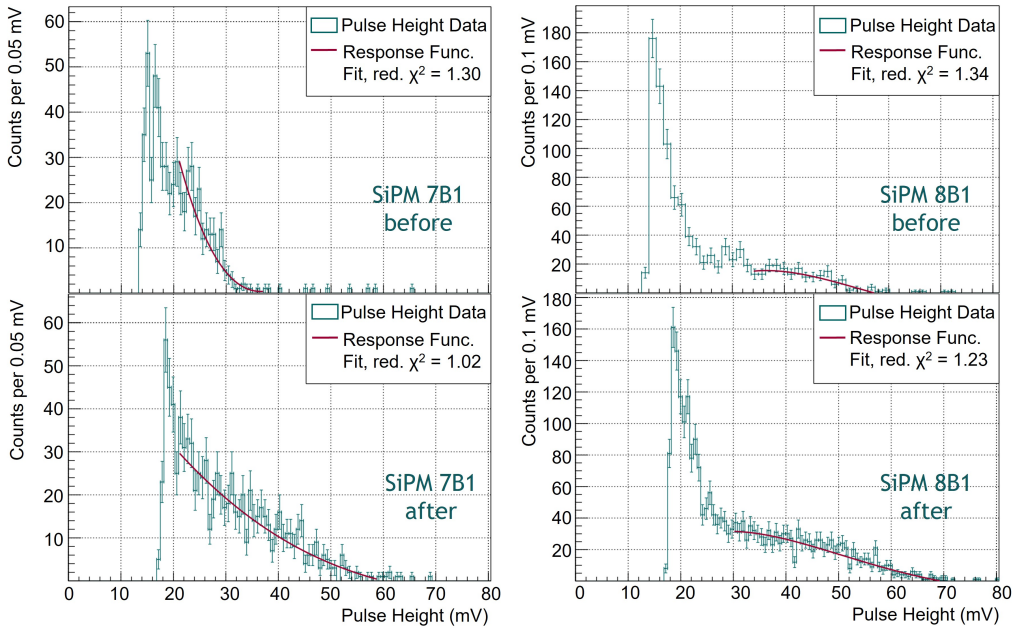

Figure 38: Pulse height spectra before and after the annealing process for SiPMs 7B1 (*left panels*) and 8B1 (*right panels*). A fit was applied to determine the pulse height of the 1061 keV Compton edge.

Summarising all the measurements performed to characterise and quantify the damage to the Veto-2 SiPMs, it can be concluded that the most likely origin for the decline is radiation damage to the silicon bulk. Although the particle flux present during their time of operation and hence the exact dose of irradiation to the detectors is unknown, MC calculations were performed to simulate the particle content of the background radiation in the DAΦNE hall. These calculations predicted bremsstrahlung on the one hand, and electrons and gammas (the latter as products of the positron annihilation) from beam losses on the other hand as the primary sources of background radiation [101]. The predicted background composition is consistent with the observed damage [98].

6.2.2 The Updated Veto-2 Design

Since the previously installed first version of the Veto-2 system was not able to stay in operation after only a few months of exposure to the DAΦNE background environment, the detector design had to be updated.
A first attempt was to increase the distance from the DAΦNE IP to the Veto-2 SiPMs. Instead of coupling the SiPMs directly to the scintillators with optical expoxy adhesive, glass fibres were used to transport the scintillating light to the SiPMs outside of the vacuum chamber. However, this design needed optimisation which was not possible in the SIDDHARTA-2 time schedule.
Therefore, the basic structure of the Veto-2 system remained unchanged; in the updated version, the SiPMs are not glued to the scintillators any more. Optical grease is now used to couple them to the scintillating tiles (a detailed description is given in Sec. 5.1.3), which enables an exchange of the SiPMs in case of radiation damage without the need to substitute the entire detector module. Moreover, the front-end electronics of the Veto-2 system were updated. As described before, the SiPMs' bias voltage is provided by the HV modules on the amplification boards. Previously, these modules operated as constant current sources to compensate the influence of small temperature fluctuations on the detectors' dark current. In the updated configuration, the modules were modified to provide a constant bias voltage. When the SiPMs experienced radiation damage which led to a steep increase in their leakage currents, the constant current HV modules thus decreased the bias voltage in an attempt to stabilise the current output. This resulted in an inappropriately low bias voltage supply for the detectors; thus, the detectors either produced signals with pulse heights indistinguishable from thermal noise, or even operated below the breakdown voltage. Furthermore, this issue lead to a decrease in pulse heights for high incident particle rates on the SiPMs, as shown in Fig. 39.

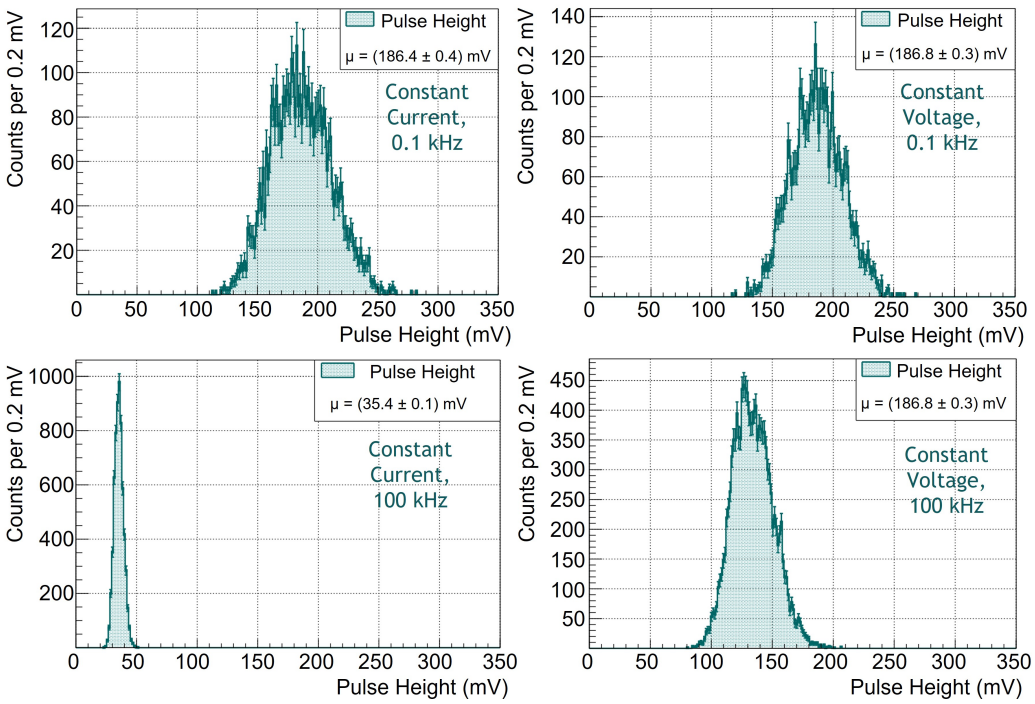

Figure 39: Pulse height spectra of a SiPM irradiated with a laser diode using the constant current HV modules (*left panels*), and the constant voltage modules (*right panels*) for a laser pulse frequency of 0.1 kHz (*top*) and 100 kHz *bottom*). The mean pulse heights μ are listed.

To quantify this issue, a SiPM was irradiated with a pulsed laser diode for multiple pulse frequencies using both the constant current HV modules and the constant voltage HV modules. The Keysight 81160A Pulse Function Arbitrary Generator provided the voltage pulses for the diode with an amplitude of 4.4 V and a width of 4 ns; the SiPM had a dark current of 0.85 μA.
The two left panels of Fig. 39 show the spectra measured with the constant current modules with a pulse frequency of 0.1 kHz at the top, and 100 kHz at the bottom. The mean pulse height (obtained from a Gaussian fit) of the distribution decreased from (186.40±0.40) mV at 0.1 kHz to (35.37±0.05) mV at 100 kHz. For the constant voltage HV modules (spectra shown in the right panels of Fig. 39), the mean value only decreased from (186.78 ± 0.35) mV at 0.1 kHz to (134.04 ± 0.16) mV at 100 kHz. The uncertainty of the mean value is obtained from the fit. The decrease of pulse heights for all measured frequencies is depicted in Fig. 40. It shows the mean pulse heights of the SiPM obtained for all measured frequencies with the constant current HV modules at the top panel, and with the constant voltage sources at the bottom. The error bars resulting from the fit error of the mean values and the frequency resolution of the pulse generator [102] are hidden behind the data points.
For the constant current modules, a clear trend towards lower pulse heights is visible starting at a pulse frequency of 5 kHz. While this is also true for the constant voltage modules, the decrease in pulse heights is much less than

for the constant current sources. Additionally, the linear decline stops and the pulse heights seem to stabilise again at approximately 15 kHz for the constant voltage source, which is not the case for the constant current supplies. Here, the SiPM's signal is indistinguishable from thermal noise in terms of its pulse height at a frequency of 100 kHz. Despite the fact that the incident MIP rate during the SIDDHARTA-2 experiment is not expected to be in the order of tens of kHz, the Veto-2 system is also subjected to leptonic background and beam losses e.g. during injection or commissioning phases and thus has to be able to operate under conditions with higher particle rates.
With the new constant voltage HV modules, the SiPMs can remain in operation in the SIDDHARTA-2 setup despite moderate radiation damage, since they produce reasonable signals with correct bias voltage at high dark currents. Moreover, high background particle rates will not have a large effect on the Veto-2 output any more. The block diagrams for both the constant current (Fig. 86) and constant voltage sources (Fig. 87) can be found in Appendix A.

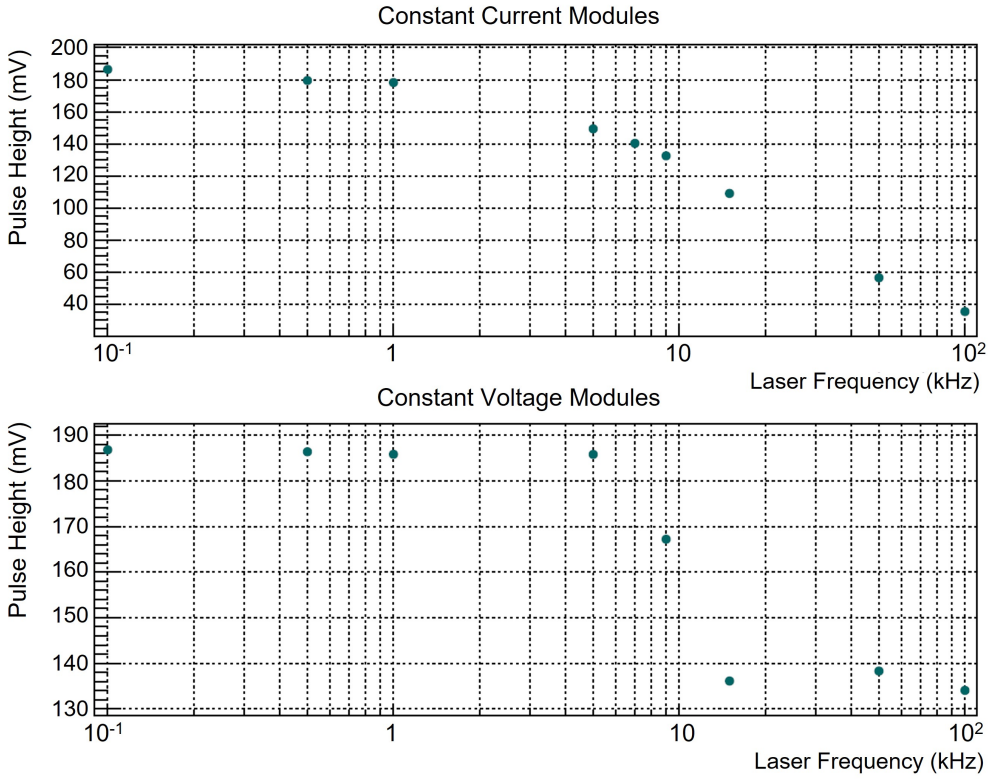

Figure 40: Mean SiPM pulse heights for different laser pulse frequencies for the constant current HV modules (*top*) and constant voltage modules (*bottom*).

6.3 The Veto-2 Calibration Procedure

Lastly, a calibration system was implemented for the Veto-2 detectors to monitor their signal output in terms of changes due to radiation damage. As described in Sec. 5.1.3, two neighbouring SiPMs share one blue LED to irradiate them in periodic intervals during beam time. The LEDs are driven by pulse generators manufactured at SMI. All 96 Veto-2 detectors were calibrated in Vienna to firstly correctly configure the gain and threshold settings on the amplification boards as well as the pulse generators to drive the LEDs, and secondly to characterise every detector in terms of its signal output. Therefore, the pulse height spectra were measured for each SiPM with both a ^{60}Co source and the pulsed LED.

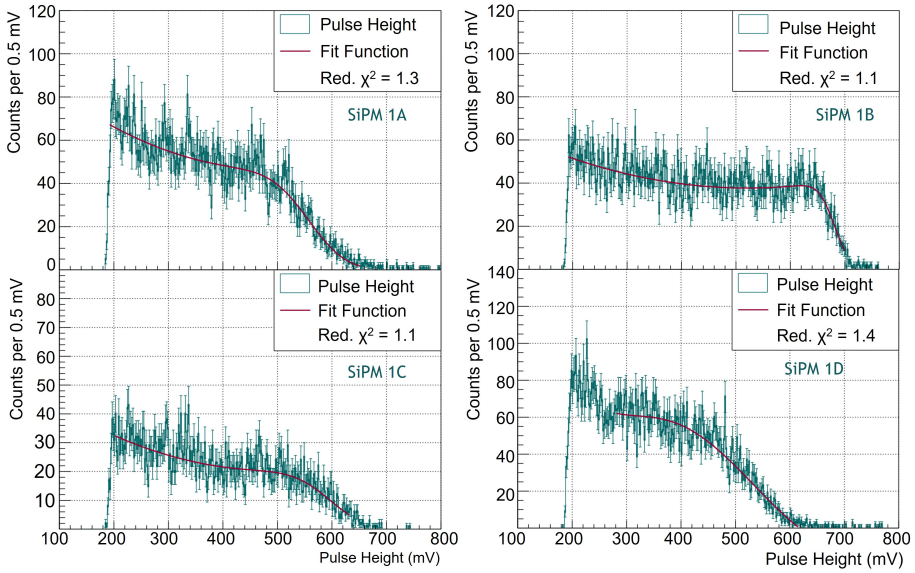

Figure 41: Pulse height spectra for four Veto-2 detectors of one calibration group, obtained with a ^{60}Co source. A fit function comprised of the convolution of a Gaussian function and a complementary error function was applied to each spectrum to determine the pulse height of the 1118.1 keV Compton edge of ^{60}Co.

First, the detectors had to be split into groups, since eight LEDs share one pulse generator, resulting in six groups of eight LEDs and sixteen Veto-2 detectors each. The LEDs have to show similar behaviour in terms of their light output, *I-V* curves and forward voltages. Hence, division into groups was done according to the LEDs' forward voltages measured with a Fluke 287 multimeter. The mean forward voltage for all 48 LEDs is 2.653 V, with a standard deviation of 0.025 V. After the division into the groups of eight, the pulse heights of the SiPMs attached to each LED in the groups were measured, using a ^{60}Co source to produce the signals. The SiPMs of one group should produce outputs with reasonable pulse heights; i.e., the Compton edge of the

1332.5 keV γ-ray should appear at pulse heights of a few hundreds of mV for all detectors of a group. For this measurement, the radioactive source was placed on top of the respective scintillator, and the SiPMs' dark currents were set to ~ 3.5 μA. The pulse heights were recorded with the LeCroy WavePro 760 Zi-A oscilloscope.
Fig. 41 shows the pulse height spectra obtained with ^{60}Co for four of the sixteen detectors of one of the groups. Each spectrum was fitted with a convolution of a Gaussian and complementary error function [99] to determine the pulse height of the Compton edge at 1118.1 keV. In Table 9, the results for one group are listed. The uncertainty of the Compton edge pulse heights are obtained from the fit. In spite of the difference in pulse heights for some of the channels in this group, all detectors produce signals in a pulse height range of a few hundreds of mV, as expected during "normal" operation in the SIDDHARTA-2 experiment.

Table 9: Pulse height values for the 1118.1 keV Compton edge of ^{60}Co and mean pulse height obtained with the LEDs for all sixteen Veto-2 detectors of one calibration group.

SiPM	**Compton Edge (mV)**	**Mean LED Pulse Height (mV)**
5A	573.5 ± 2.0	483.46 ± 0.41
5B	620.5 ± 19.2	655.57 ± 0.38
5C	487.0 ± 12.5	460.98 ± 0.28
5D	538.5 ± 6.2	442.98 ± 0.28
6A	671.8 ± 10.1	575.89 ± 0.59
6B	726.7 ± 4.0	559.70 ± 0.59
6C	681.5 ± 2.3	531.79 ± 0.50
6D	460.9 ± 32.5	578.94 ± 0.48
7A	404.4 ± 9.3	320.15 ± 0.38
7B	676.4 ± 6.4	661.03 ± 0.34
7C	583.4 ± 5.2	450.08 ± 0.39
7D	542.1 ± 9.8	681.92 ± 0.26
8A	584.2 ± 4.1	405.56 ± 0.49
8B	622.3 ± 5.8	557.81 ± 0.52
8C	574.9 ± 4.9	392.47 ± 0.41
8D	659.2 ± 10.3	603.79 ± 0.49

After the adjustment of the settings on the amplification boards for all channels in this way, the pulse height spectra of the SiPMs were now measured not with ^{60}Co, but the calibration LEDs as source. The groups of LEDs were driven with their dedicated pulse generators at a frequency of 100 Hz and a pulse width of 128 ns. The pulse heights of the SiPM signals were again acquired with the LeCroy WavePro 760 Zi-A oscilloscope's measuring tools.
Each distribution was fitted with a Gaussian function and the mean value was determined for each detector as a measure of SiPM response to the LED pulses.

They are listed in Table 9 for each SiPM of one group. Fig. 42 shows the pulse height distributions obtained with their respective LEDs for four detectors of this group. As with the values for the Compton edge, the detectors all have a mean pulse height response of a few hundred mV. These results provide a guideline for the detectors' operation in the SIDDHARTA-2 experiment and will be used to correctly configure the electronic settings of the Veto-2 system as well as to track any changes in detector performance during operation.

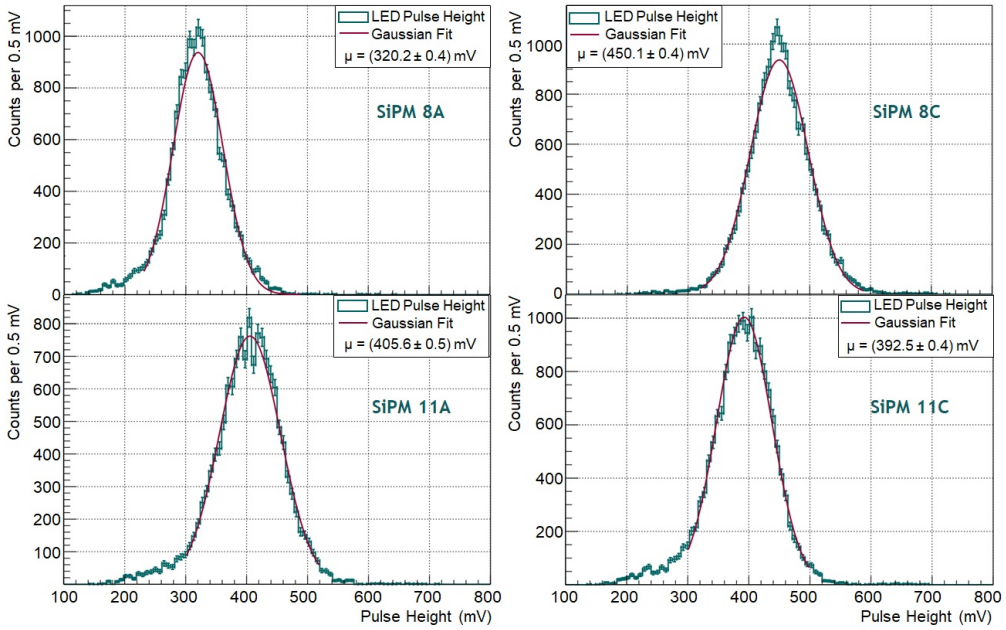

Figure 42: Pulse height distributions for four Veto-2 detectors of one calibration group, obtained with their respective LEDs. The mean values μ are given by the Gaussian fit.

7 SDD Characterisation

The following section presents a theoretical introduction to the characterisation of SDDs in terms of their energy response and energy resolution. The data for this analysis were collected with the SIDDHARTINO setup installed in the DAΦNE collider hall, which is described in Sec. 8. This section discusses the SDD energy calibration procedure and analyses the linearity and stability of the detectors' response.

7.1 Energy Response

The energy response function of silicon drift detectors is based on research on Si(Li) detectors [103], [104]. It was further developed to the current version during the E570 experiment at KEK [64]. The SDDs' energy response to an X-ray of energy E is comprised of several components: the main peak $G(E)$, a second, smaller peak shifted towards higher energies to account for pile-up effects $P(E)$, a low-energy tail $T(E)$, and a flat shelf towards low energies $S(E)$. The low-energy tail appears due to effects such as incomplete charge collection in the SDD or electron escape, shifting events from the main peak towards lower energies, leading to an exponential decrease [105]. Hence, the energy response function $f(E)$ is given by

$$f(E) = G(E) + P(E) + T(E) + S(E). \tag{43}$$

The main peak of the energy response function as well as the pile-up peak are described by Gaussian distributions of standard deviation σ, with the pile-up Gaussian having a smaller amplitude and shifted mean value compared to the main peak. The tail component is described by a quasi-exponential expression [106]:

$$G(E) = \frac{A_G}{\sqrt{(2\pi)}\sigma} \cdot exp\left(-\frac{(E-E_0)^2}{2\sigma^2}\right) \tag{44}$$

$$P(E) = \frac{A_G F_G^P}{\sqrt{(2\pi)}\sigma} \cdot exp\left(-\frac{(E-(E_0-E_P))^2}{2\sigma^2}\right) \tag{45}$$

$$\begin{aligned} T(E) =& \frac{A_G F_G^T}{2\beta\sigma} \cdot exp\left(\frac{E-(E_0-E_T)}{\beta\sigma} + \frac{1}{2\beta^2}\right) \cdot \\ & \cdot erf\left(\frac{E-(E_0-E_T)}{\sqrt{2}\sigma} + \frac{1}{\sqrt{2}\beta}\right) \end{aligned} \tag{46}$$

$$S(E) = \frac{A_G F_G^S}{2E_0} \cdot \frac{E-E_0}{\sqrt{2}\sigma}, \tag{47}$$

where A_G and E_0 denote the amplitude and mean of the main Gaussian, respectively; F_G^P, F_G^T and F_G^S the ratios between the amplitudes of the pile-up peak, tail or shelf and the main Gaussian, respectively; E_P and E_T the shifts of the mean values for the pile-up peak and tail with respect to the main Gaussian mean; and β the slope of the tail component [107]. In addition, the background is best described by a combination of constants and exponential functions, depending on the set of data. Usually, the constant shelf component of the spectral response can be included into the background function. Hence, the resolution of the X-ray peak is determined by the Gaussian and tail components.

7.2 Energy Resolution

In silicon detectors, the intrinsic energy resolution is dependent on the detector material and the energy deposited in the detector by the incident particle. Each particle of energy E will either yield a lattice excitation resulting in the production of phonons, or ionisation and therefore the production of charge carriers. The average number of charge carriers N_Q produced in ionisation processes is given by $N_Q = E/\epsilon$, with ϵ being the mean energy needed to produce an electron-hole pair. If the full energy of the incident particle is absorbed in the detector, the number of ionisation events is not accurately described by Poissonian statistics any more since the individual ionisations do not occur independently of each other. This behaviour is described by the Fano factor F, which includes all the possible processes resulting in energy transfer in the detector. The consequential intrinsic energy resolution $\Delta E_{\text{in}}(E)$ for a particle of energy E, which is the FWHM, is given by

$$\begin{aligned} \Delta E_{\text{in}}(E) = & \\ & = 2\sqrt{2log(2)}\sigma(E) = \frac{\sqrt{FN_Q}}{N_Q}E \simeq \\ & \simeq 2.35\frac{\sqrt{FN_Q}}{N_Q}E = 2.35\sqrt{F\epsilon E}, \end{aligned} \tag{48}$$

as described in [108]. Moreover, an energy-independent component ΔE_{noise} with contributions from thermal and electronic noise has influence on the total energy resolution $\Delta E_{\text{tot}}(E)$, leading to

$$\Delta E_{\text{tot}}(E) = \sqrt{\Delta E_{\text{noise}}^2 + \Delta E_{\text{in}}^2(E)}. \tag{49}$$

7.3 The SDD Energy Calibration

To minimise the influence of fluctuations in the SDD response on the kaonic atom measurement, periodic calibration runs are performed during the beam times of SIDDHARTA-2 and its commissioning phase, SIDDHARTINO. X-ray tubes mounted on the vacuum chamber of the apparatus shine on high-purity Ti and Cu foils installed on the target cell. The foils are activated and emit characteristic X-rays, which are then used to perform an energy calibration every few days.
A fit function is applied to the calibration X-ray spectra based on the SDD energy response as described earlier in Sec. 7.1. For the calibration data, the background shape is reproduced with a constant plus an exponential function. Apart from the lines used for the energy calibration, Ti $K_{\alpha 1}$ and Cu $K_{\alpha 1}$, the full fit function also includes the Ti and Cu $K_{\alpha 2}$ and K_{β} lines, as well as the $K_{\alpha 1}$, $K_{\alpha 2}$, and K_{β} lines of Fe and Mn, and the $K_{\alpha 1,2}$ lines of Zn. At higher energies, the Bi $L_{\alpha 1}$ transition is present. Those X-rays originate not from the calibration foils, but from the ceramic carrier of the SDDs or the surrounding setup inside the vacuum chamber. The Ti and Cu $K_{\alpha 1}$ lines, however, have the highest signal-to-background ratio. The final fit function has a total of 41 parameters, including the background, peak, pile-up, shelf and tail components previously described. The σ of the Gaussian peaks is determined via an energy-dependent component including the Fano factor and an energy-independent constant noise, as described in the previous section, with the Fano factor and the constant noise as free fit parameters.
The conversion of the SDD data from ADC channels to electronvolt is then performed in the following way:

$$m = \frac{E_{\text{Ti K}_{\alpha 1}} + E_{\text{Cu K}_{\alpha 1}}}{2} \tag{50}$$

$$k = \frac{E_{\text{Cu K}_{\alpha 1}} - E_{\text{Ti K}_{\alpha 1}}}{E_{\text{Cu K}_{\alpha 1,\text{fit}}} - E_{\text{Ti K}_{\alpha 1,\text{fit}}}} \tag{51}$$

$$E_{\text{eV}} = m + k \cdot \left(E_{\text{adc}} - \frac{E_{\text{Cu K}_{\alpha 1,\text{fit}}} - E_{\text{Ti K}_{\alpha 1,\text{fit}}}}{2} \right), \tag{52}$$

with m being the mid point between the Ti $K_{\alpha 1}$ and Cu $K_{\alpha 1}$ energies, $E_{\text{Ti K}_{\alpha 1}}$ and $E_{\text{Cu K}_{\alpha 1}}$ denoting the reference values for the respective transition energies, k the slope of the linear calibration, $E_{\text{Cu K}_{\alpha 1,\text{fit}}}$ and $E_{\text{Ti K}_{\alpha 1,\text{fit}}}$ the mean values of the transition lines obtained from the fit to the data, E_{eV} the calibrated energy in eV, and E_{adc} denoting the energy in ADC channels for the particular X-ray event. The energy calibration is a linear conversion, as indicated by Eq. 52 and Fig. 43. Therefore, the linearity of the SDD system has to be studied (see Sec. 7.4).

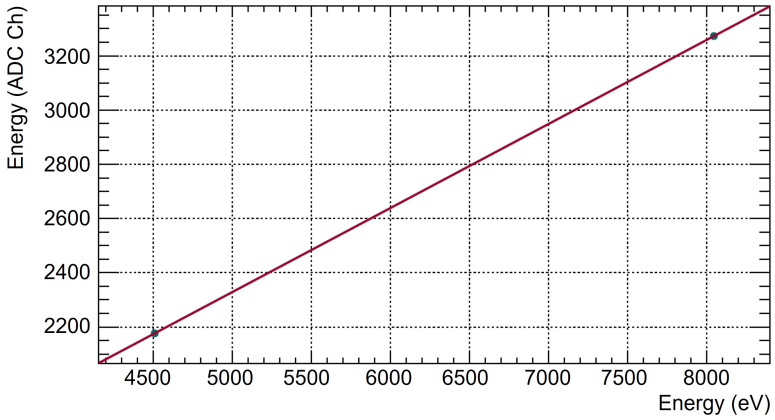

Figure 43: Conversion from ADC channels to eV. A linear fit is applied to the results from the global fit to the X-ray spectrum.

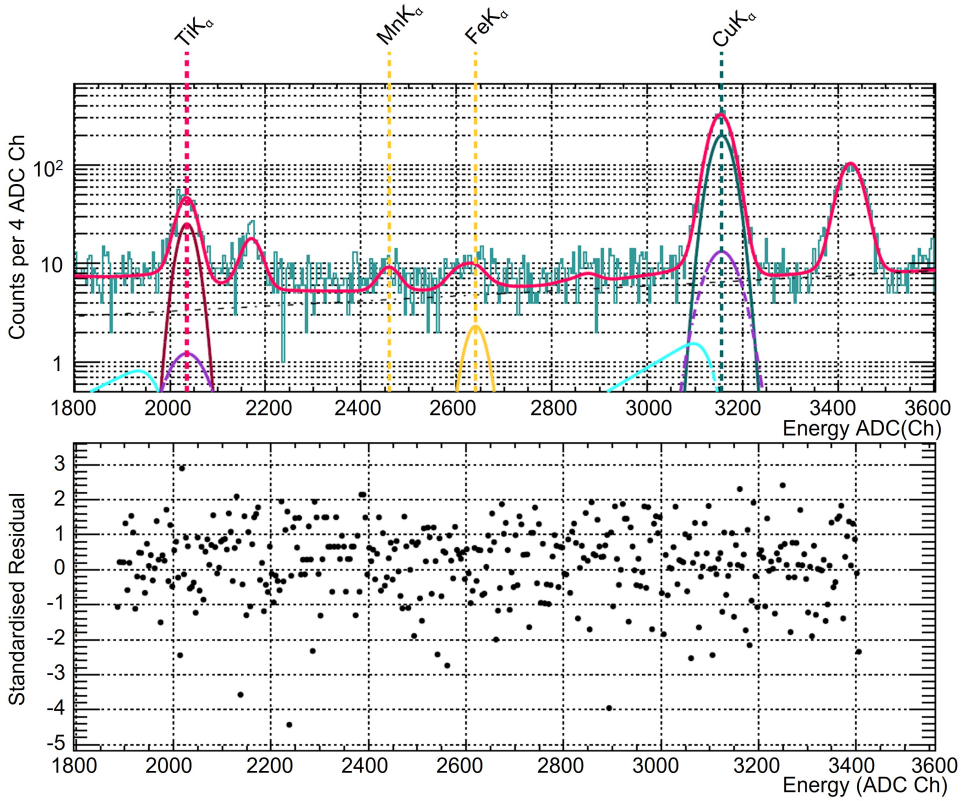

Figure 44: *Top:* Calibration X-ray spectrum in ADC channels for one SDD, obtained with a Ti and Cu target. The lighter magenta curve represents the global fit function; in addition, the components of the response function are shown as well, including the main Gaussian (dark magenta, yellow, and dark cyan), the low-energy tail (light cyan) and the pile-up peak (purple). *Bottom:* Standardised residuals for the global fit function shown above.

The top panel of Fig. 44 shows a typical calibration X-ray spectrum for one SDD channel. The global fit function is shown in light magenta, with a reduced χ^2 of 1.15. Moreover, the components of the SDD response function are added, with the main Gaussian functions in dark magenta for the Ti K_α, yellow for the Fe K_α, and dark cyan for the Cu K_α peaks. The low-energy tail components are plotted in light cyan, and the pile-up components in purple. In the bottom panel, the standardised residuals, i.e. the residuals of the global fit function divided by the Poissonian standard deviation of each bin, are shown. From the global fit, the energy resolution at the Fe K_α energy of 6403.8 eV [109] was determined from six calibration runs and found to be 155 eV, on average, with a standard deviation of 10 eV.
The Fe K_α transition line can also be utilised to evaluate the accuracy of the calibration method, since only the Ti and Cu K_α lines are used for the energy conversion. Hence, the calibrated energy spectra of all SDDs are summed up and a fit function is applied to the Fe K_α line, consisting of a Gaussian with a tail component, and an exponential function to describe the background (see Fig. 45). In this way, the Fe K_α transition energy was extracted from the fit as (6404.9 ± 2.5) eV, resulting in a deviation of (-1.1 ± 2.5) eV from the reference value [109]. This indicates that the accuracy of the SIDDHARTA-2 calibration method is within a few electronvolts and provides a first prediction of the systematic uncertainty of the SIDDHARTA-2 measurement. An analogous analysis is described in [110].

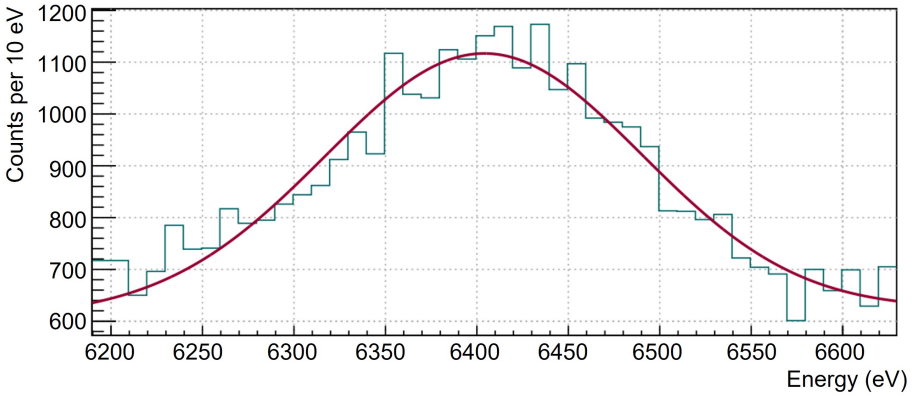

Figure 45: Fe K_α transition line summed for all calibrated SDDs with applied fit function to determine the Fe K_α transition energy.

7.4 Linearity

Since the calibration procedure is based on a linear conversion from ADC channels to eV and assumes a linear behaviour over the entire energy range of the SIDDHARTA-2 ROI, the linearity of the energy response of the SDDs has to be studied.

Therefore, data was accumulated with eight SDD arrays (see Sec. 8.1 for a detailed description of the experimental setup) and an X-ray tube placed at the position of the upper KT scintillator (Fig. 46). The X-ray tube activated a multi-element calibration target consisting of strips of titanium, iron, copper, bromine and strontium foils [111]. The characteristic X-rays of the calibration target range in energy from approximately 4 to 15 keV. The summed X-ray spectrum of all 48 SDDs was calibrated, again using only the Ti and Cu K_α lines.

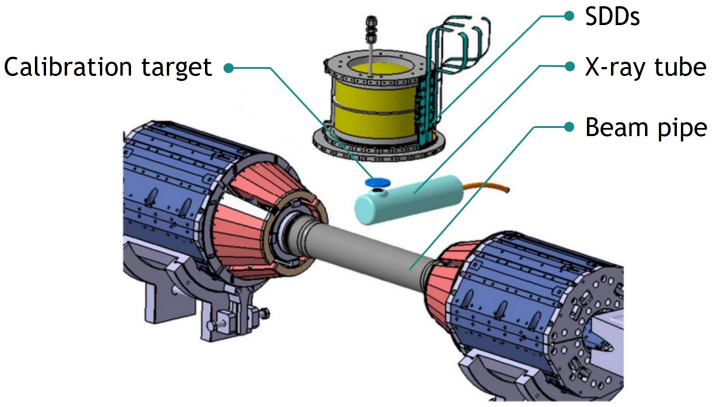

Figure 46: Schematic of the experimental setup with the X-ray tube and multi-element calibration target to study the linearity of the SDD system. *Adapted from [111].*

This dataset was acquired in 2020; the setup has since been optimised. At that time, the SDDs still showed considerable electronic noise on their signals from pick-up and grounding imperfections. Therefore, on top of the statistical uncertainty from Poissonian statistics, a systematic uncertainty of 2.5% of the bin height was added to the data. A fit was applied to the calibrated spectrum with a reduced χ^2 of 1.9 (ndf = 503), including the main Gaussian and the tail components of the SDDs' response for all visible transitions. The background was fitted with the sum of a constant and two exponential functions.
The top panel of Fig. 47 shows the fitted spectrum; the bottom panel shows the residuals of the mean values of the peaks obtained from the fit with respect to the reference values for Ti, Fe, Cu, Bi, Br, and Sr [109]. The obtained values are also listed in Table 10. The uncertainties from the fit are corrected for the reduced χ^2. At the energy of the Fe $K_{\alpha 1}$ transition at 6.4 keV, the system shows a non-linearity of 0.05 eV. For higher X-ray energies, the non-linearity increases up to an absolute value of 8.7 eV at the energy of the Sr $K_{\alpha 1}$ transition at 14.1 keV. According to the theoretical predictions for the shift of the kaonic deuterium ground state (see Table 1), the K^-d K-series X-rays are expected in an energy range from $\sim$ 6 to 15 keV. Up to an energy of $\sim$ 9 keV, the non-linearity of the SDD system is within 3.7 eV; up to X-ray energies of 15 keV, a non-linearity of 8.7 eV can be expected. Below energies of 7 keV, the non-linearity of the SDDs is < 1 eV. Thus, for energies larger than 7 keV,

the SDDs' non-linearity represents the dominant factor contributing to the systematic uncertainty of measurements of transition energies.

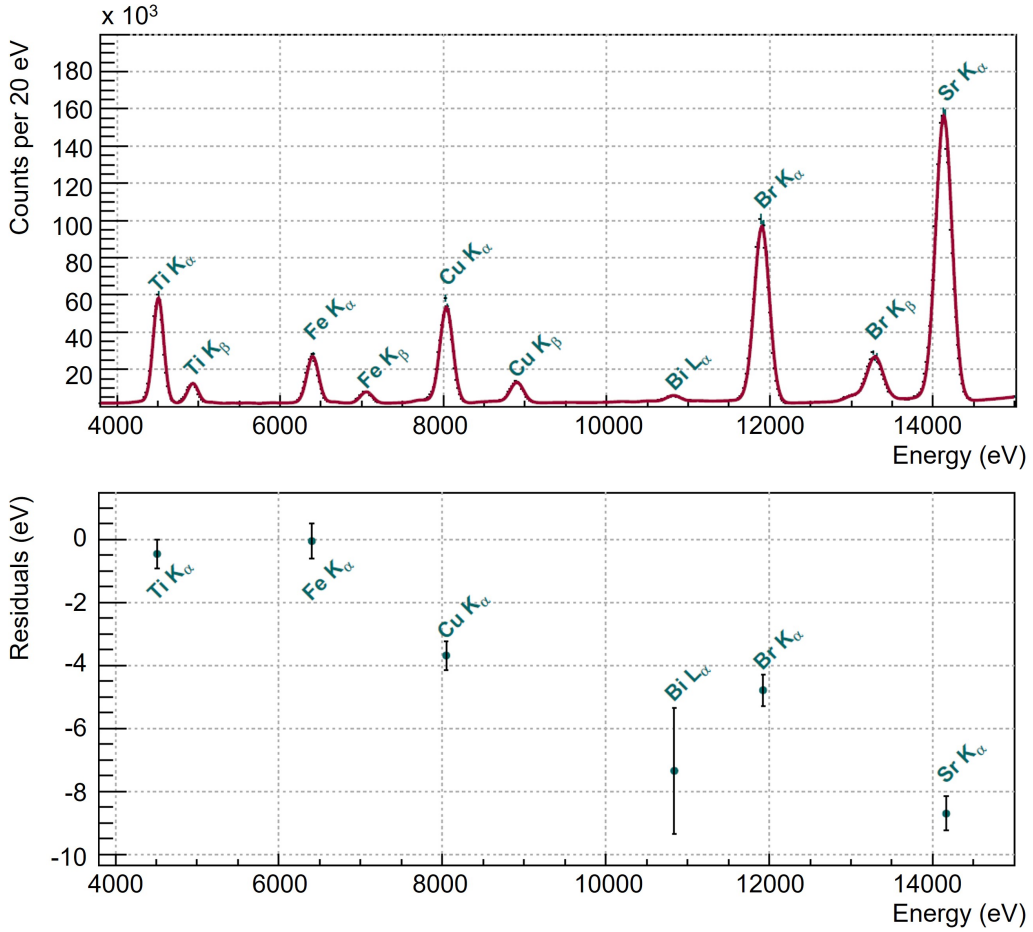

Figure 47: *Top:* X-ray energy spectrum summed for all SDDs which was obtained with a multi-element target. The applied fit function is shown in magenta. *Bottom:* Residuals of the peaks' mean energy values with respect to the reference values for those transitions.

Table 10: Transition energies and residuals obtained from the global fit function for the dominant transitions in the observed X-ray spectrum to determine the non-linearity of the SDD system.

Transition	**Residual (eV)**
Ti K_α	-0.45 ± 0.64
Fe K_α	-0.05 ± 0.78
Cu K_α	-3.68 ± 0.64
Bi L_α	-7.34 ± 2.78
Br K_α	-4.78 ± 0.71
Sr K_α	-8.70 ± 0.76

7.5 Stability

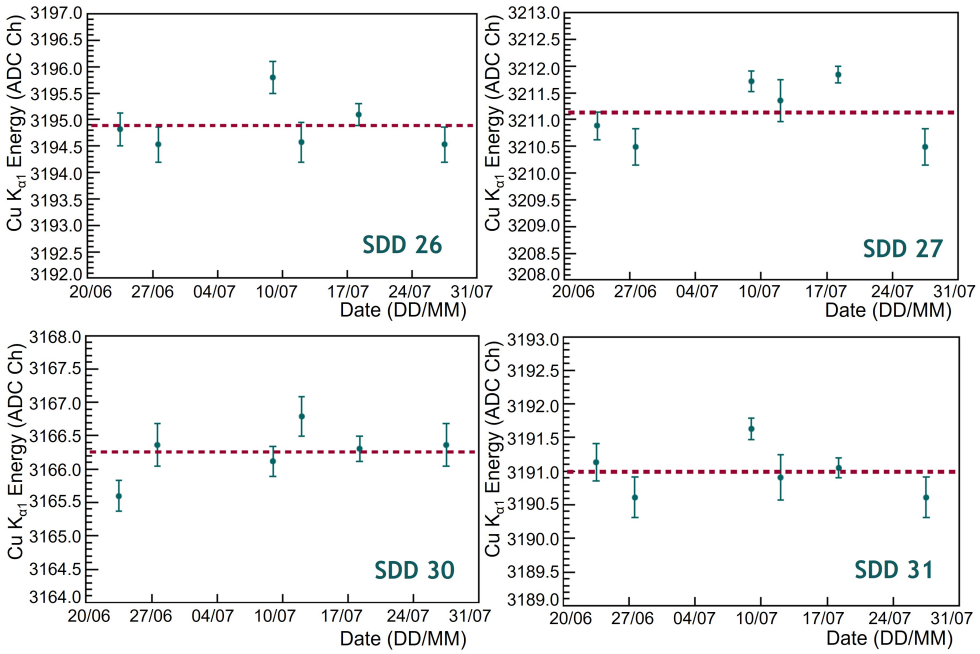

Figure 48: Stability over time of the Cu $K_{\alpha1}$ transition energy obtained from the calibration procedure, shown for four SDDs. The dashed line indicates the mean value for each SDD. Six calibration runs were performed during the beam time in 2021.

In addition to the linearity of the system, its stability is an important parameter for precision measurements like X-ray spectroscopy of light kaonic atoms, since it is a potential source of systematic uncertainty for the determination of transition energies in kaonic atoms. The stability of the SDDs was studied using six calibration runs performed over a span of 34 days in 2021 with the SIDDHARTINO setup (see Sec. 8). Fits were applied to the individual X-ray spectra for all 48 SDDs. From these fits, the fluctuation in the transition energy of the Cu $K_{\alpha1}$ transition was obtained. Fig. 48 shows the resulting energies and their mean value for four SDDs over six calibration runs. The error bars are given by the fit uncertainty. The deviations of the respective mean transition energies of the Cu $K_{\alpha1}$ line between these four SDDs are within 0.55 ADC channels, corresponding to $\sim$ 2.0 eV. This is in accordance with the linearity of the system for the Cu K_{α} energy as well as the precision of the calibration procedure. Moreover, it determines the number of necessary calibration runs, as a more stable SDD system requires less frequent calibrations and thus increases the time for production runs. As mentioned for the accuracy of the calibration method, an analogous but independent analysis of the SDD stability is presented in [110]. For X-ray energies below 7 keV, where the non-linearity of the SDD response can be neglected, this instability repres-

ents the dominant contribution to the systematic uncertainty of the performed measurements.

7.5.1 Rate Dependence of the SDD Response

In addition to its linearity and stability over time, the SDDs' response has to be independent of the incident particle rate. This stability was tested in the LNF laboratory by performing two types of calibration runs with different current and voltage configurations of the X-ray tube, resulting in different output rates of 60 Hz and 600 Hz. The transition energies for the Cu K_α lines obtained from fits to the calibration X-ray spectra for each SDD were used to compare their response during exposure to the different rates. The results are shown in Fig. 49: the top panel shows a comparison of the obtained transition energies for an X-ray tube (XRT) output rate of 60 Hz (dark cyan) and 600 Hz (dark magenta), for several SDDs. In the bottom panel, the differences between these two energies are plotted for those SDDs. The error bars were calculated via Gaussian error propagation using the uncertainty of the fit results. As clearly visible, the difference of the copper transition energy between the two X-ray tube configurations is de facto zero for almost all SDDs. This indicates an independence on the incident particle rate and thus rate stability of the detectors' performance, within the limits of accuracy of the calibration method and linearity of the SDDs.

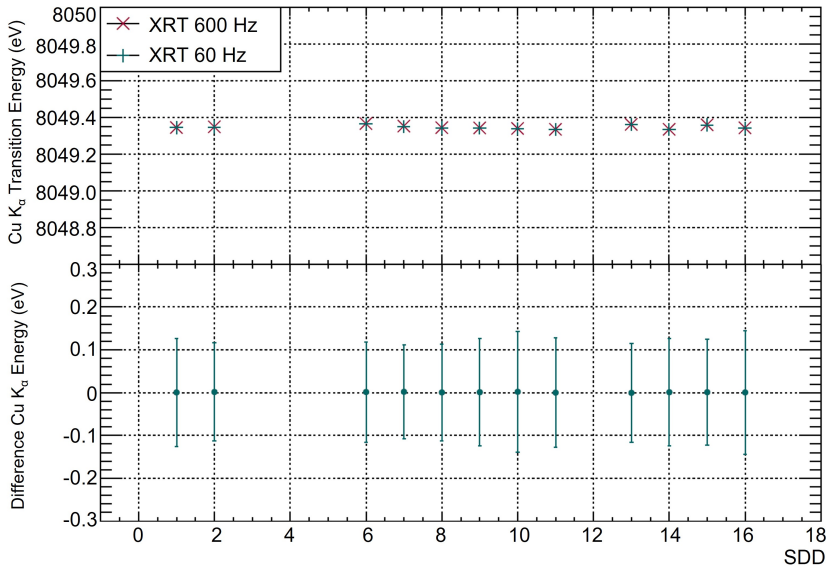

Figure 49: *Top:* Cu K_α transition energies extracted from fits to the calibration spectra obtained with two different X-ray tube configurations, resulting in output rates of 60 Hz and 600 Hz, for several SDDs. *Bottom:* Difference between the transition energies obtained for 60 Hz and 600 Hz.

8 SIDDHARTINO

Starting in 2021, the SIDDHARTA-2 experiment performed commissioning runs with a reduced setup called SIDDHARTINO. The aim of these measurements was to study the performances of the detector systems, the remaining apparatus, and of DAΦNE to ensure optimal conditions for the upcoming kaonic deuterium measurement. During this time, data were collected with an empty target as well as multiple different target densities of gaseous ^{4}He. In total, integrated luminosities of 22.8 pb^{-1} for the empty target, 21.2 pb^{-1} for a gas density of 1.52% Liquid Helium Density (LHeD), and 9.5 pb^{-1} for 0.66% LHeD were accumulated with the SIDDHARTINO setup. For both empty and helium targets, different degrader configurations were tested (see Sec. 8.2.4 for details). Table 11 provides a summary of the performed runs. This section provides an introduction to the analysis procedure performed on the kaonic atom X-ray data. The kaonic helium-4 commissioning data provides an example. The background characterisation and reduction methods and their results are presented. Finally, the fitting process of the spectra and, eventually, the extraction of the transition energy, level shifts and width are described based on the ^{4}He data as example. The analysis is based on C++ and ROOT code developed by H. Shi for the SIDDHARTA kaonic hydrogen analysis, which was further expanded in the scope of this thesis.

Table 11: Data acquisition runs performed with the SIDDHARTINO setup.

Date	Target	Degrader	Int. Lumi. (pb^{-1})
30/05/2021 - 09/06/2021	empty	550 µm	8.6
09/06/2021 - 15/06/2021		no	7.6
15/06/2021 - 20/06/2021		750 µm	6.6
Sum			**22.8**
24/06/2021 - 29/06/2021	1.52% LHeD	750 µm	4.8
29/06/2021 - 05/07/2021		550 µm	6.9
05/07/2021 - 09/07/2021		425 µm	4.4
09/07/2021 - 13/07/2021		350 µm	5.2
Sum			**21.2**
13/07/2021 - 19/07/2021	0.66% LHeD	550 µm	**9.5**

8.1 Experimental Setup

The experimental apparatus of SIDDHARTINO was installed at the DAΦNE IP in April 2019. It shared the same components as the final setup of SIDDHARTA-2 except for a reduced number of SDD arrays. Moreover, the

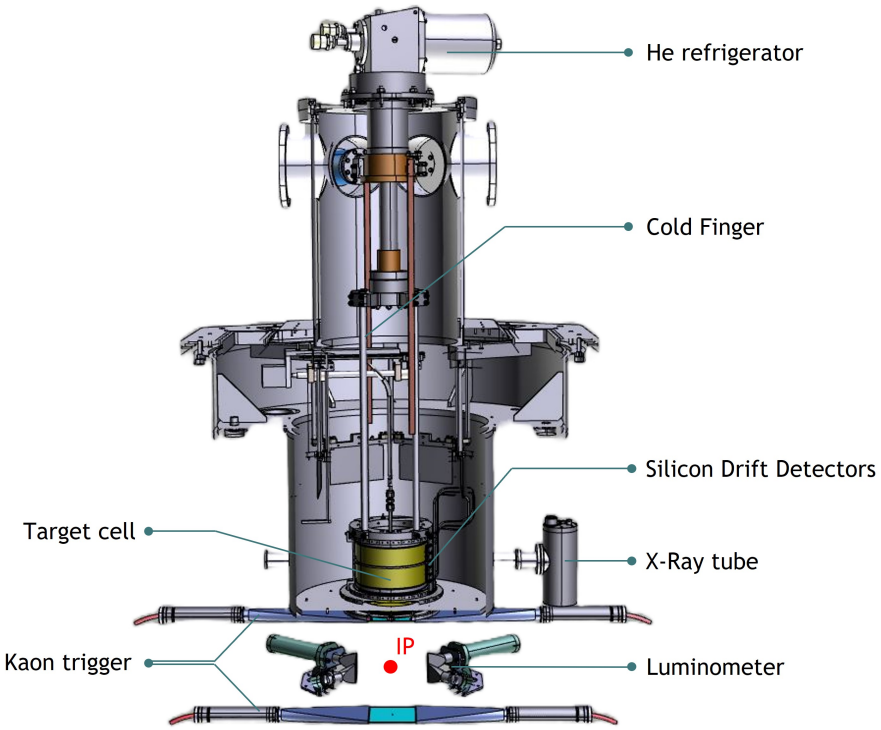

Figure 50: Schematic cross section of the SIDDHARTINO apparatus.

veto systems were not yet implemented to enable a direct comparison between the conditions at that time and the conditions during the SIDDHARTA measurements. For SIDDHARTINO, only eight out of the 48 SDD arrays were employed, resulting in a total of 64 read-out channels and a total active area of 41 cm^2. The SDDs were kept at a temperature of $\sim$ 170 K. One of the two X-ray tubes was installed for the periodic calibration of the SDDs. The luminometer provided real-time feedback on the beam and background conditions and the kaon detector was used as described in Sec. 5.1. Fig. 50 shows a schematic of the SIDDHARTINO setup. The target cell was kept at approximately 23 K at a pressure of 1.20 bar for a gas density of 1.52% LHeD, and of 0.42 bar for a gas density of 0.66% LHeD, respectively. The setup was evacuated to a pressure of approximately 3.5×10^{-7} mbar.

8.2 Analysis of Commissioning Data

8.2.1 SDD Selection

The periodically performed calibration measurements as described in the previous Sec. 7.3 provide a tool for the characterisation of the performance of

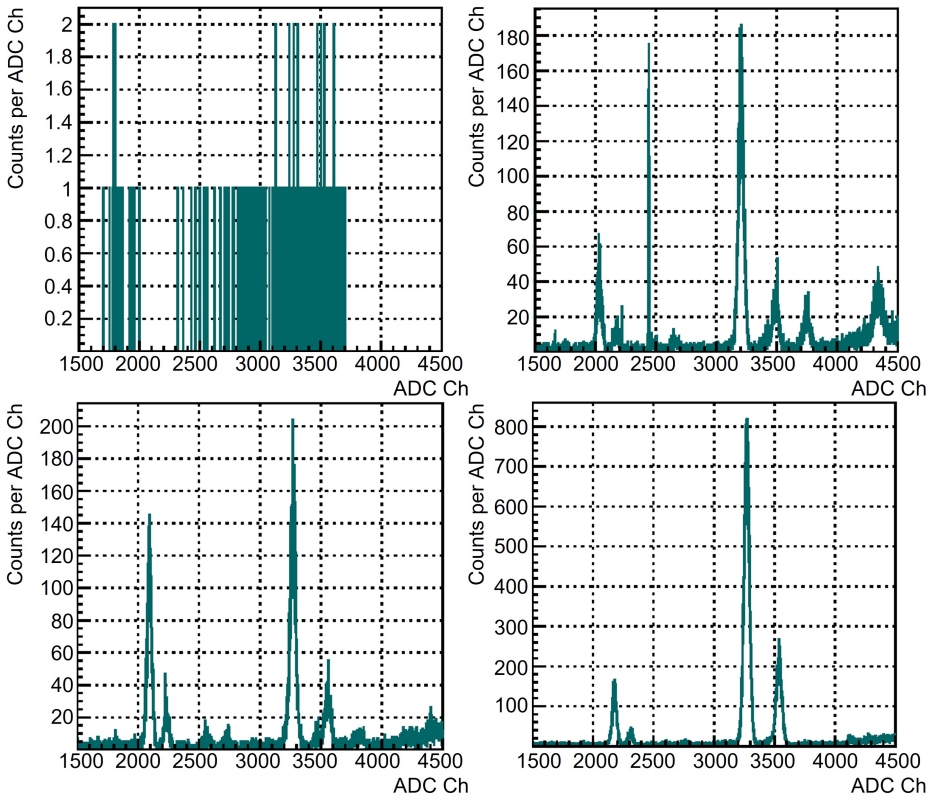

Figure 51: Calibration spectra of four SDD channels. *Top left:* Only a few events are visible in the spectrum, corresponding to a non-functional SDD channel and thus a rank of 1. *Top right:* A spike is present at approximately 2450 ADC channel, leading to a rank of 2 for this SDD channel. *Bottom left:* An SDD channel with a rank of 3 - the calibration lines are clearly distinguishable, but the signal-to-noise ratio is low. *Bottom right:* The spectrum features even statistics and clear calibration lines with good resolution, corresponding to a rank of 5.

the SDDs. Only the detectors fulfilling the requirements necessary for kaonic atom spectroscopy in terms of their noise level, energy resolution, and spectroscopic response are selected. After inspecting their calibration spectra, each SDD is "ranked" according to their performance. A rank of 0 to 2 indicates that the SDD channel is non-functional (see Fig. 51 top left panel) or spikes of electronic noise are visible in the spectra (Fig. 51 top right panel). For a rank of 3, the copper and titanium calibration peaks are clearly visible in the spectrum, but the level of background is high or the signal-to-noise ratio is low, as shown in the bottom left panel of Fig. 51. SDD channels with a rank of 4 or 5 show clear peaks with a low background level and a good energy resolution (see Fig. 51 bottom right panel). For the final analysis, only SDD channels with a rank of ≥ 3 are considered. Moreover, only events from SDDs with an energy resolution of < 200 eV at the energy of the manganese K_α line at ~ 5.9 keV [109] are accepted for the final kaonic atom X-ray spectrum.

8.2.2 Background Characterisation and Rejection

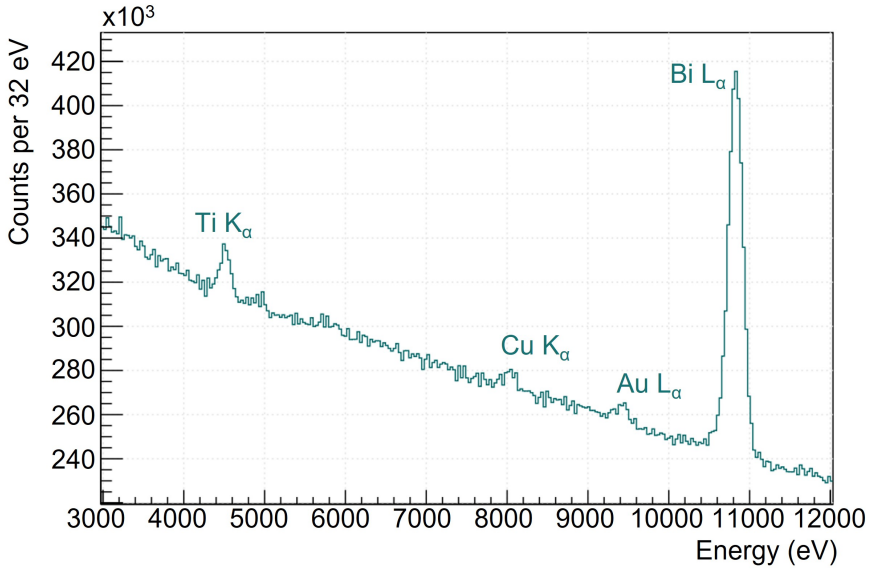

Figure 52: Summed SDD spectra for the SIDDHARTINO runs with an integrated luminosity of 21 pb^{-1} without the application of any background cuts. No kaonic lines are visible.

In the DAΦNE collider environment, the background consists mainly of two components - an asynchronous part of MIPs, originating from both beam-beam and beam-environment interactions, and a synchronous part of charged particles from kaon interactions with the setup. The identification and suppression of background are essential to extract the kaonic atom transition lines. Fig. 52 shows the summed energy spectrum of all used SDDs without any background cuts; only the Ti K_α, Cu K_α, Au L_α, and Bi L_α fluorescence lines from the target cell, surrounding solid structures, and SDD ceramic carriers are visible. No kaonic atom transitions can be identified due to the high background levels.
A first measure to reduce the asynchronous background is to define a trigger, given by a coincidence in signals in both the upper and lower scintillators of the KT, representing the detection of a K^+K^- pair. Only events within a 5 µs time window with respect to these K^+K^- signals are accepted, reducing the background by a factor of 7.7×10^3. Moreover, the kaon detector can be used to reject the asynchronous part by discriminating between MIPs and kaons by their difference in ToF. The time difference between signals on the kaon trigger's scintillators and the radio frequency (RF) of DAΦNE to which the e^+ and e^- bunches are synchronised is used for this distinction. The top panel of Fig. 53 shows a 2D distribution of the TDC signals for the top and bottom scintillators of the KT, while the bottom panel shows the diagonal projection of this distribution. The visible double structure is a result of using half of

the DAΦNE RF as reference clock, since the Constant Fraction Discriminator (CFD) processing the signals from the KT is unable to deal with rates as high as the DAΦNE RF. In both panels, the lines show the selected regions identifying the kaon signals. In this way, the background can be further reduced by a factor of 1.4.

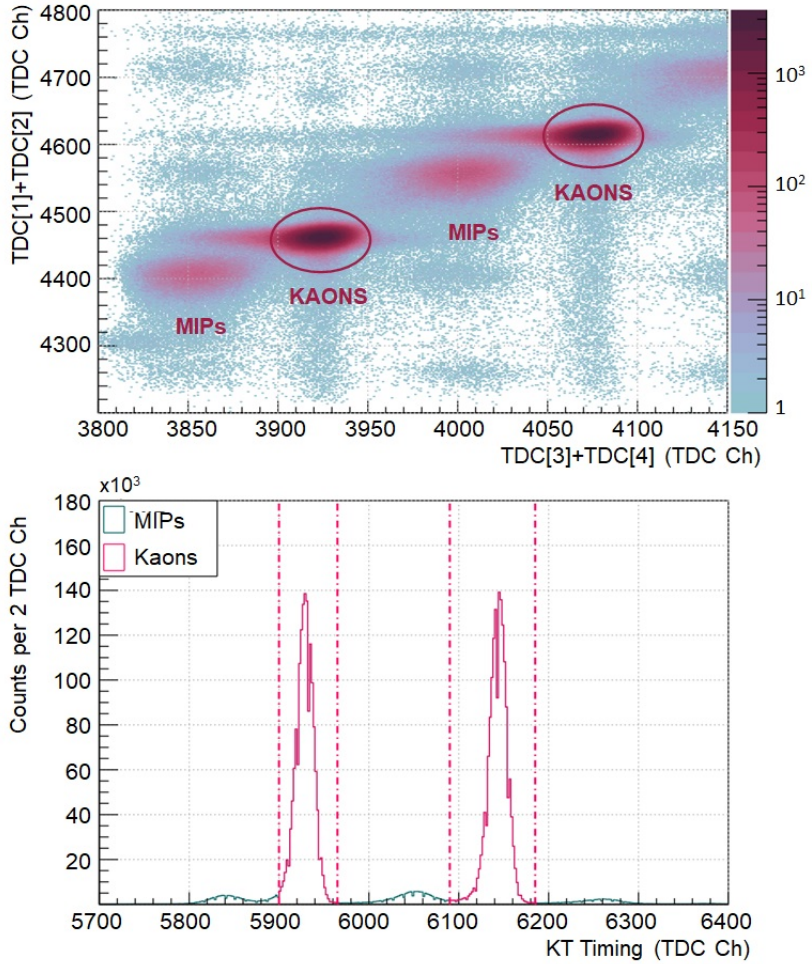

Figure 53: *Top:* 2D plot of the mean time of each KT scintillator. *Bottom:* Diagonal projection of the KT mean time signals shown in the top panel. The magenta regions, enclosed in the vertical lines, are the selected kaon events.

Fig. 54 shows the time difference between a kaon trigger signal, i.e. a coincidence in the upper and lower scintillators, and an X-ray signal in the SDDs. The peak corresponds to SDD signals in coincidence with the KT and the synchronous hadronic background which is a result of kaon decays and kaon absorption processes. Its width is given by the electrons' drift time through the SDD bulk, which depends on the SDDs' temperature. For the SIDDHARTINO data, the SDD drift time was found to be 922 ns. The flat region corresponds to electromagnetic and leptonic asynchronous background which is a

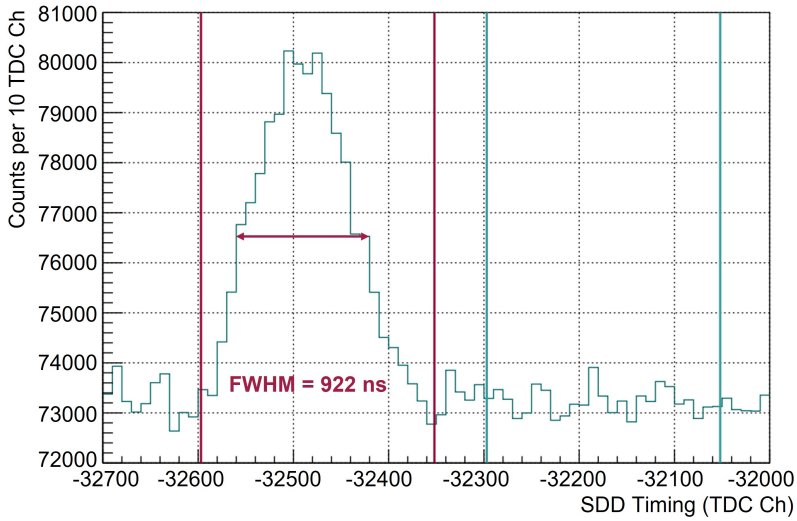

Figure 54: Time difference between the K^+K^- signals on the KT and the SDD signals. The magenta vertical lines indicate the acceptance window selecting kaon-correlated events, whereas the cyan lines indicate the uncorrelated events.

result of beam-beam interactions via the Touschek effect [112], beam losses and bremsstrahlung. The ratio of the correlated events, including the hadronic background, to the electromagnetic background component provides a useful tool to further characterise the background and optimise the setup and shielding accordingly. It can be determined by the ratio between an integral over the main peak region (indicated by the magenta lines in Fig. 54) and an integral of the same width over a region in the flat shelf (indicated by the cyan lines in Fig. 54). For SIDDHARTINO, this ratio was found to be 1.05 (Table 12), which is in agreement with the conditions found during the SIDDHARTA measurements in 2009 [101]. To further reduce the electromagnetic background not correlated to the kaons, the timing information of the SDDs can be used. By selecting only SDD events within this main drift time peak, i.e. events in coincidence with the kaon trigger, the electromagnetic background is further suppressed by a factor of 1.9. The hadronic background component will be suppressed by the dedicated veto systems in the full SIDDHARTA-2 setup. A detailed analysis of the effect of the veto systems is given in Sec. 9.3.

Table 12: Characterisation of kaon-correlated and electromagnetic background via the SDD timing information for SIDDHARTINO.

Background Characterisation for SIDDHARTINO	
Number of Events in Peak	1.88×10^6
Number of Events in Flat Region	1.80×10^6
Ratio	1.05

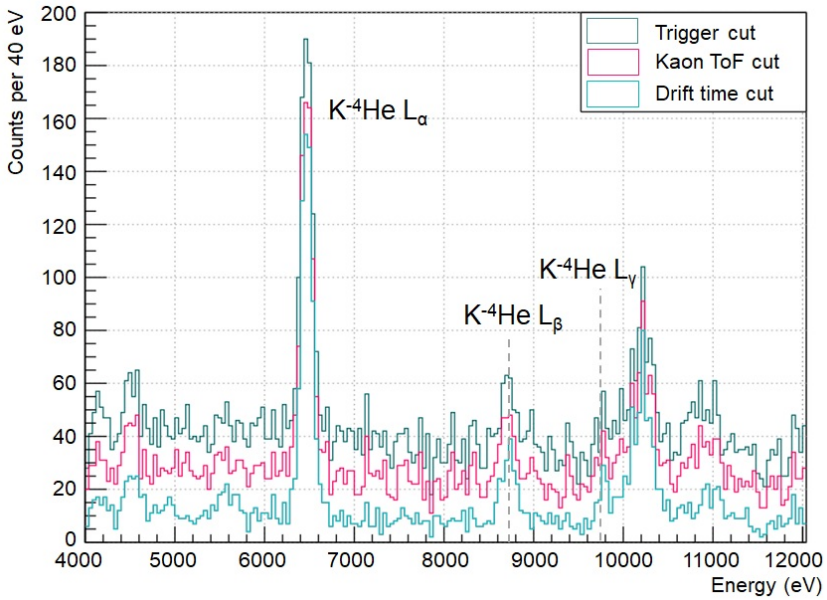

Figure 55: K^4He spectra obtained during the SIDDHARTINO runs, after each respective step of background reduction.

Table 13: Background rejection factors from 6 - 10 keV for the different methods of suppression during the SIDDHARTINO runs.

Cut	Number of events in ROI	Rejection Factor
No Cut	3.5×10^7	-
Trigger	4545	7747
Kaon selection via ToF	3191	1.4
Drift time selection	1666	1.9
All cuts	1666	2.1×10^4

In Fig. 55, the influence of the different background cuts on the kaonic ^{4}He X-ray spectrum obtained by SIDDHARTINO for an integrated luminosity of 21 pb^{-1} is shown. After the final data selection step, the kaonic atom transition lines from the helium gas as well as the solid setup materials are clearly visible. In total, the background was reduced by a factor of 2.1×10^4 (see Tab. 13). During the SIDDHARTINO runs, the veto systems were not in use in order to enable a direct comparison of the conditions during the SIDDHARTINO kaonic helium runs with the previous measurements preformed by SIDDHARTA.

8.2.3 Measurement of Kaonic Helium-4 Transitions

In order to extract the desired parameters from the kaonic atom lines, a fit was applied to the X-ray spectrum. After the application of all background cuts described above, the kaonic atom lines originating from the target gas as well

as solid structures in the setup are clearly distinguishable in the X-ray spectrum. All kaonic atom lines corresponding to transitions towards an energy level on which the strong interaction between the K^- and the nucleons has a possible effect are fitted with a Voigtian curve, i.e. a convolution of a Gaussian function and a Lorentzian line shape. The width of the Gaussian component is again dependent on the Fano factor and X-ray energy as explained in Sec. 7.2. The Lorentzian linewidth corresponds to the intrinsic broadened width of the energy level induced by the strong interaction. Only the $K^-{}^4He$ L-series transitions are visible in the SIDDHARTINO X-ray spectrum. Their transition energies calculated from quantum electrodynamics (QED) and including corrections for vacuum polarisation and relativistic recoil effects are listed in Table 14 [113]–[115].

Table 14: Kaonic ^{4}He L-series transition energies present in the SIDDHARTINO X-ray spectrum as calculated from quantum electrodynamics.

Transition		**Transition Energy (eV)**
L_α	$3d \rightarrow 2p$	6463 [113]
L_β	$4d \rightarrow 2p$	8722 [113]
L_γ	$5d \rightarrow 2p$	9766.8 [114]
L_{high}	$6d \rightarrow 2p$	10334.5 [114]
	$7d \rightarrow 2p$	10676.5 [115]
	$8d \rightarrow 2p$	10898.7 [115]
	$9d \rightarrow 2p$	11050.9 [115]
	$10d \rightarrow 2p$	11159.9 [115]

To account for possible strong interaction effects, the kaonic helium L-lines were fitted with a Voigtian function, while the other lines, from both fluorescence and kaonic atom transitions produced in the solid materials of the setup, were fitted with the usual energy response function with a Gaussian and exponential tail component, as described in Sec. 7.3. The effects of the strong interaction on the the higher kaonic transitions from elements with larger Z produced in the setup are negligible. The tail components of each fitted line have universal slope, shift, and gain parameters, according to the description in Sec. 7.1. The background shape is described in the fit by the sum of a constant, a linear, and an exponential function. The final fit function has 42 free parameters, listed in Table 15. The energy differences between the $K^-{}^4He$ L_α line and the higher L-series transitions including the L_β and L_γ lines, and transitions from higher n-states up to $n = 10$, were fixed in the fit. The complete fit function is listed in Appendix B. The MIGRAD minimiser provided in the Minuit-2 minimisation package of ROOT was used to perform a χ^2 fit. All parameters were left free in the fit, but appropriate limits were chosen to find the correct minimum.

Table 15: Parameters of the fit function applied to the SIDDHARTINO $K^{-4}He$ X-ray spectrum.

Function Component	**Parameter**
Background function	$p_{0,\text{const}}$ $p_{1,\text{lin}}$, $p_{2,\text{lin}}$ $p_{3,\text{exp}}$, $p_{4,\text{exp}}$
SDD energy resolution	Fano factor Constant noise
Global energy shift	Shift
$K^{-4}He$ parameters	$K^{-4}He$ $(3 \to 2)$ mean value $K^{-4}He$ $(3 \to 2)$ width Γ_{2p} $K^{-4}He$ $(3 \to 2)$ amplitude $K^{-4}He$ $(4 \to 2)$ / $K^{-4}He$ $(3 \to 2)$ relat. ampl. $K^{-4}He$ $(5 \to 2)$ / $K^{-4}He$ $(3 \to 2)$ relat. ampl. $K^{-4}He$ $(6 \to 2)$ / $K^{-4}He$ $(3 \to 2)$ relat. ampl. $K^{-4}He$ $(7 \to 2)$ / $K^{-4}He$ $(3 \to 2)$ relat. ampl. $K^{-4}He$ $(8 \to 2)$ / $K^{-4}He$ $(3 \to 2)$ relat. ampl. $K^{-4}He$ $(9 \to 2)$ / $K^{-4}He$ $(3 \to 2)$ relat. ampl. $K^{-4}He$ $(10 \to 2)$ / $K^{-4}He$ $(3 \to 2)$ relat. ampl.
Other included lines	$K^{-}C$ $(5 \to 4)$ amplitude $K^{-}C$ $(6 \to 5)$ / $K^{-}C$ $(5 \to 4)$ relat. ampl. $K^{-}C$ $(7 \to 5)$ / $K^{-}C$ $(5 \to 4)$ relat. ampl. $K^{-}C$ $(6 \to 4)$ / $K^{-}C$ $(5 \to 4)$ relat. ampl. $K^{-}O$ $(6 \to 5)$ / $K^{-}C$ $(5 \to 4)$ relat. ampl. $K^{-}O$ $(7 \to 6)$ / $K^{-}C$ $(5 \to 4)$ relat. ampl. $K^{-}O$ $(7 \to 5)$ / $K^{-}O$ $(6 \to 5)$ relat. ampl. $K^{-}N$ $(5 \to 4)$ / $K^{-}C$ $(5 \to 4)$ relat. ampl. $K^{-}N$ $(6 \to 5)$ / $K^{-}N$ $(5 \to 4)$ relat. ampl. $K^{-}N$ $(7 \to 5)$ / $K^{-}C$ $(5 \to 4)$ relat. ampl. $K^{-}N$ $(7 \to 6)$ / $K^{-}C$ $(5 \to 4)$ relat. ampl. $K^{-}Al$ $(7 \to 6)$ mean value $K^{-}Al$ $(7 \to 6)$ / $K^{-}C$ $(5 \to 4)$ relat. ampl. $K^{-}Al$ $(8 \to 7)$ / / $K^{-}C$ $(5 \to 4)$ relat. ampl. $K^{-}Al$ $(9 \to 8)$ / $K^{-}Al$ $(8 \to 7)$ relat. ampl. $K^{-}Ti$ $(11 \to 10)$ / $K^{-}C$ $(5 \to 4)$ relat. ampl. $K^{-}Ti$ $(12 \to 11)$ / $K^{-}Ti$ $(11 \to 10)$ relat. ampl. Ti K_α amplitude Ti K_β / Ti K_α relat. ampl.
Tail components	Tail shift Universal tail gain Universal tail slope

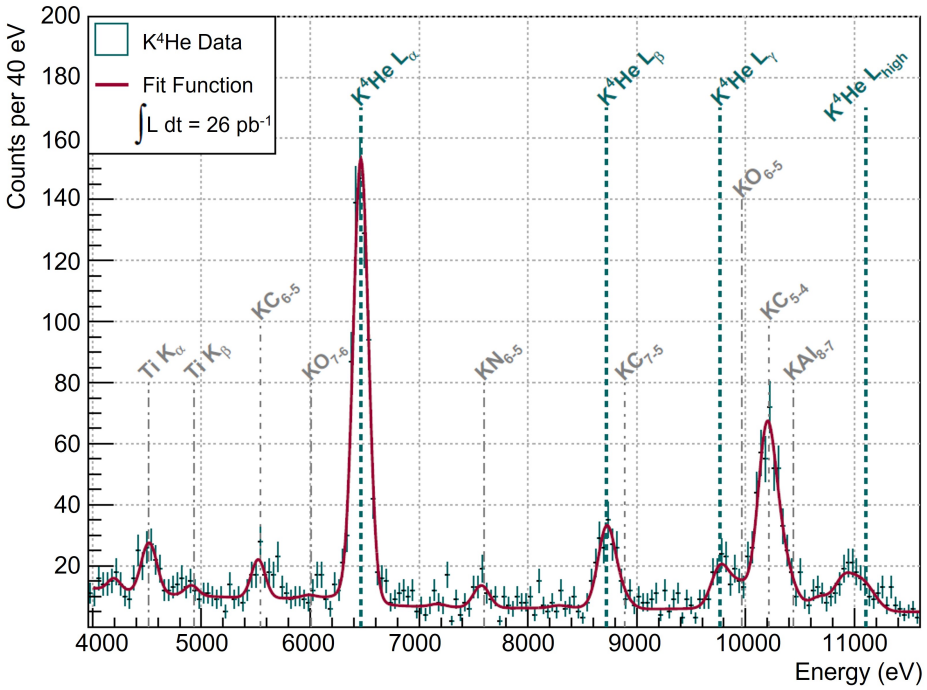

Figure 56: SIDDHARTINO kaonic helium X-ray spectrum with the applied fit function for an integrated luminosity of 26 pb^{-1}.

The data were summed for both helium target densities, leading to an integrated luminosity of 26 pb^{-1}. The fit was applied to the resulting X-ray spectrum with a reduced χ^2 of 1.2 and a number of degrees of freedom (ndf) of 151. From the fit, the K^{4}He L$_\alpha$ transition energy and the $2p$ level shift ε_{2p} and width Γ_{2p} were extracted. It has to be noted that the Lorentzian linewidth of the kaonic helium-4 $2p$ level is predicted to be very small with respect to the SDDs' energy resolution [62]. The statistical uncertainty arises from the fit, while the systematic uncertainty is determined by several factors. Firstly, the performance of the SDDs regarding their stability and linearity, which were quantified in Sec. 7, contributes to the systematic uncertainty of the measurement. This results in an uncertainty of 2.0 eV. Secondly, the analysis procedure can contribute to the systematic uncertainty of the results. Therefore, the analysis was performed with varying conditions in terms of the background reduction cuts and histogram binning. To determine the effect of the drift time cut on the results, five different lower (LT) and upper thresholds (HT) were set for the acceptance window of the SDD timing in coincidence with the kaon trigger, as shown in Fig. 57. The width of the acceptance window remained unchanged, while its position was varied within 40 TDC channels or 332 ns. Table 16 lists the values of the K^{4}He L$_\alpha$ transitions energy and Γ_{2p} obtained from the fit for all five cases. The listed statistical uncertainty is again given by the fit, corrected for the reduced χ^2. The maximum deviation of the transition energy is 1.6 eV, which lies within the statistical uncertainties of the results for each chosen time window. It can therefore be concluded that the choice of SDD

timing acceptance window does not significantly contribute to the systematic uncertainty of the SIDDHARTINO results. Furthermore, the effect of the histogram bin width of the SIDDHARTINO X-ray spectrum on the fit results was studied. The bin width was varied ranging from 10 eV to 50 eV. The fit results are listed in Table 17. The maximum deviation of the kaonic helium L_α transition energy was again found to be negligible within the statistical uncertainties of the results. Hence, the choice of histogram bin width does not contribute to the systematic uncertainty of the SIDDHARTINO results. The governing component of the systematic uncertainty remains the stability of the SDD response within 2.0 eV.

Table 16: Influence of the selection of the accepted SDD timing window in coincidence with the KT on the SIDDHARTINO K^4He L_α transition energy and $2p$ width.

LT (Ch)	HT (Ch)	L_α Energy (eV)	Γ_{2p} (eV)
-32617	-32372	6463.8 $\pm$ 3.2	0.6 $\pm$ 6.8
-32607	-32362	6463.3 $\pm$ 3.2	0.6 $\pm$ 7.6
-32597	-32352	6462.2 $\pm$ 3.3	0.6 $\pm$ 7.5
-32587	-32342	6463.2 $\pm$ 3.2	0.6 $\pm$ 6.7
-32577	-32332	6463.1 $\pm$ 3.3	0.6 $\pm$ 5.6

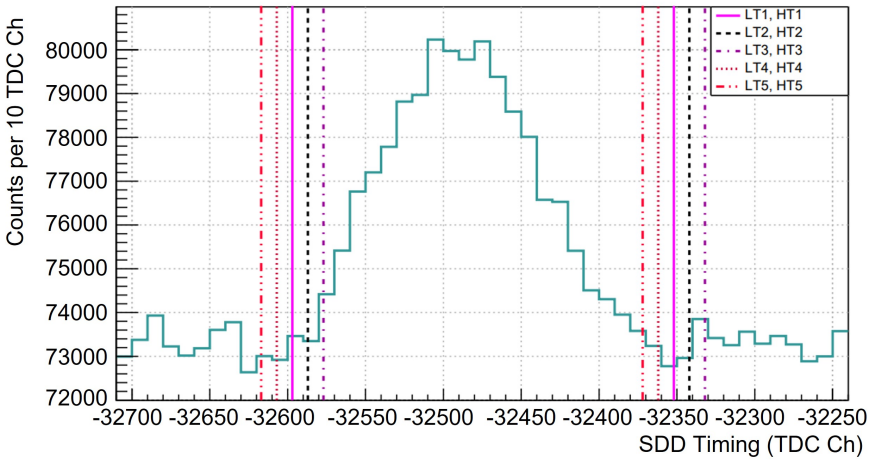

Figure 57: SDD timing data with varying acceptance windows to study their influence on the systematic uncertainty of the SIDDHARTINO results.

Therefore, the results of the SIDDHARTINO kaonic helium-4 measurement are listed in Table 18. The $2p$ level energy shift ε_{2p} was found to be $(0.8 \pm 3.2_{\text{stat}} \pm 2.0_{\text{syst}})$ eV, which is in agreement with the results from previous measurements performed by the E570, SIDDHARTA, and E62 collaborations [2]–[4], [64]. The E62 experiment used microcalorimeters for X-ray detection, while E570 and SIDDHARTA employed SDDs. Results from an independent analysis on the SIDDHARTINO data were published in [116]. This commissioning meas-

urement proves the ability of the SIDDHARTA-2 apparatus to operate under the difficult conditions present in the DAΦNE collider hall and to fulfil the requirements necessary for the experimentally challenging kaonic atom spectroscopy. The measurement provided a tool to characterise and optimise the experimental apparatus. After the conclusion of the commissioning phase of the experiment, additional data were accumulated with the full SIDHHARTA-2 setup. From the combination of the SIDDHARTINO and SIDDHARTA-2 helium-4 data, new precise results of the L-series transitions were achieved, as will be described in detail in Sec. 9.1.

Table 17: Influence of histogram binning on the SIDDHARTINO K^4He L_α transition energy and $2p$ width.

Bin width (eV)	**L_α Energy (eV)**	**Γ_{2p} (eV)**
10	$6465.2 \pm 2.9_{\text{stat}}$	$0.6 \pm 5.4_{\text{stat}}$
20	$6463.0 \pm 3.0_{\text{stat}}$	$0.6 \pm 7.3_{\text{stat}}$
25	$6464.6 \pm 3.0_{\text{stat}}$	$0.6 \pm 5.5_{\text{stat}}$
40	$6463.8 \pm 3.2_{\text{stat}}$	$0.6 \pm 6.8_{\text{stat}}$
50	$6464.1 \pm 3.0_{\text{stat}}$	$0.6 \pm 7.0_{\text{stat}}$

Table 18: SIDDHARTINO results for the kaonic ^4He $3d \rightarrow 2p$ X-ray transition.

$K^{-4}He$ $3d \rightarrow 2p$ transition energy	$(6463.8 \pm 3.2_{\text{stat}} \pm 2.0_{\text{syst}})$ eV
$K^{-4}He$ ε_{2p}	$(0.8 \pm 3.2_{\text{stat}} \pm 2.0_{\text{syst}})$ eV
$K^{-4}He$ Γ_{2p}	$(0.6 \pm 6.8_{\text{stat}} \pm 2.0_{\text{syst}})$ eV

8.2.4 Degrader Optimisation

As mentioned before, the SIDDHARTINO kaonic helium-4 measurement was used for the optimisation of the experimental apparatus. One important component of the setup to be refined was the kaon degrader. Although the momentum of the charged kaons produced by DAΦNE is already low, a thin plastic degrader is still needed to slow the K^- down enough to efficiently stop them in the target gas. The thickness and material composition of this degrader, placed below the upper scintillator of the kaon trigger, were varied during the SIDDHARTINO beam time to maximise the number of stopped kaons in the target.

For the gas density of 1.52% LHeD, four different degraders were installed to compare the results. Since the kaons are emitted with a small boost toward the centre of the collider ring due to the small collision angle of the beams, the degrader has to compensate for this difference in momenta and hence its thickness is not homogeneous. Instead, it consists of multiple thin layers of Mylar, with increasing number of layers towards the boost-side, as seen in Fig.

58. The four degraders had a central thickness of 350 µm, 425 µm, 550 µm (shown in Fig. 58) and 750 µm. The latter one also contained a layer of zirconium foil in addition to the Mylar to test different materials with varying densities and stopping powers.

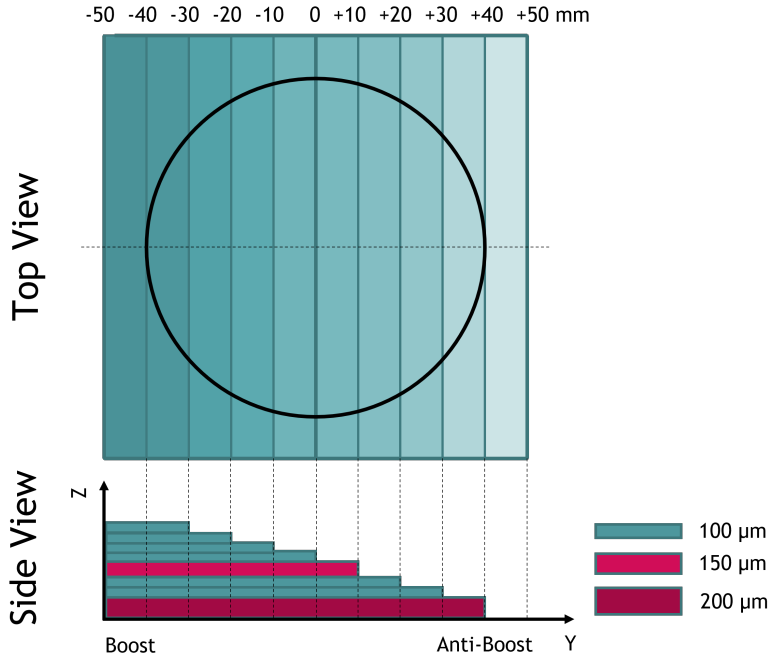

Figure 58: Schematic drawing of the Kapton degrader for SIDDHARTINO and SIDDHARTA-2, with increasing thickness towards the boost-side of the collider. *Adapted from [116].*

For each degrader thickness, the number of events in the kaonic ^{4}He L_α peak was determined and normalised by the number of kaon triggers and the active area of SDDs. Since the kaonic ^{4}He lines are fitted with Voigtian functions, the number of K$^-$^{4}He L_α events was given by the Voigtian amplitude parameter divided by the bin width. Fig. 59 shows the obtained results. The error bars in y-direction are given by the fit uncertainty of the K$^-$^{4}He L_α amplitude. The curve in Fig. 59 does not describe a fit applied to the data but rather an interpolation of the data points, and gives an idea of the degrader curve. Of all the tested configurations, the degrader with a thickness of 425 µm was closest to the optimal setup. It consists of eight layers of (1×9) cm^2 Mylar strips of varying thickness (see Fig. 58).
The degrader optimisation process is also described in [116]. It has to be noted that the optimal degrader is dependent on the target gas and its density and the optimisation process thus has to be repeated for different target configurations.

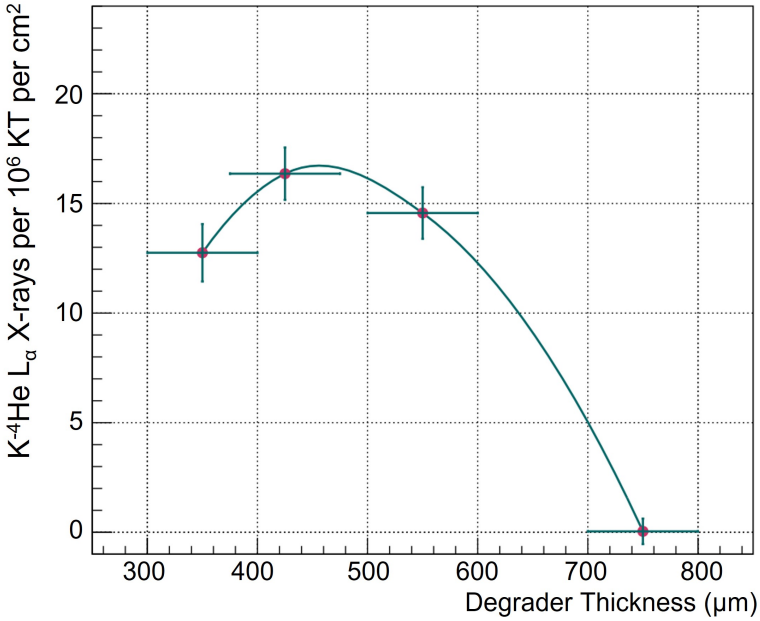

Figure 59: Number K^4He L_α X-ray events compared for degraders with varying thickness.

9 SIDDHARTA-2

In 2022, the full SIDDHARTA-2 setup was installed at the DAΦNE interaction point, now including all 48 arrays of SDDs, both X-ray tubes, and the veto systems comprised of the charged kaon detector, Veto-1, and Veto-2 system. Several runs were performed with a He target of two different gas densities (45.6 pb^{-1} of integrated luminosity for a density of 1.4% LHeD and 4.8 pb^{-1} for a density of 1.1% LHeD) and different degrader configurations. The target cell was kept at a temperature of $\sim$ 21 K. The setup was evacuated to a pressure of $\sim 9 \times 10^{-7}$ mbar and the SDDs operated at a temperature of $\sim$ 132 K. For an integrated luminosity of 29.8 pb^{-1}, data were collected with a deuterium target at a gas density of 1.04% LDD. Table 19 lists all the runs performed with the SIDDHARTA-2 setup discussed in this work.
In this section, a final result for the kaonic helium-4 $3d \rightarrow 2p$ transition, obtained from a combination of the SIDDHARTINO and SIDDHARTA-2 data, is presented. From this data, several transitions from kaonic atoms produced in the solid setup materials are extracted and presented for the first time. Moreover, a first analysis of the kaonic deuterium data, including a detailed investigation of the performance of the Veto-2 system, is described.

Table 19: Run summary for the SIDDHARTA-2 experiment.

Date	Target	Degrader	Int. Lumi. (pb^{-1})
13/04/2022 - 20/04/2024		475 µm	6.6
24/04/2022 - 29/04/2022		350 µm	4.7
29/04/2022 - 04/05/2022	1.4 % LHeD	600 µm	5.6
04/05/2022 - 26/05/2022		475 µm	28.7
Sum			**45.6**
03/06/2022 - 02/07/2022	1.04% LDD	475 µm	**29.8**
07/07/2022 - 11/07/2022	1.1% LHeD	500 µm	**4.8**

9.1 Final Analysis of Kaonic Helium-4

With the full SIDDHARTA-2 setup, an additional 50.4 pb^{-1} of data were collected with a helium-4 target. In combination with the SIDDHARTINO helium data, this results in a total of 81.1 pb^{-1}. The kaonic helium $3d \rightarrow 2p$ transition analysis as described in Sec. 8.2 was repeated on the complete helium data to improve the statistical precision of the results.
After the selection of SDDs according to their rank derived from the calibration data, as described previously, several steps of background reduction were applied to the new helium-4 data. Firstly, the kaon trigger was again used to

reduce the asynchronous background by selecting only events within a 5 μs time window in coincidence with a K^+K^- signal in the KT. Secondly, events originating from kaons were selected by using the ToF in the KT to distinguish them from MIPs produced in beam interactions. The 2D distributions of the mean time of particles detected in the kaon trigger is shown in the top panels of Fig. 60 and 61 for the run with a gas density of 1.4% LHeD and 1.1% LHeD, respectively. The bottom panels show the diagonal projections of these distributions, with the selected regions corresponding to kaon events highlighted in magenta.

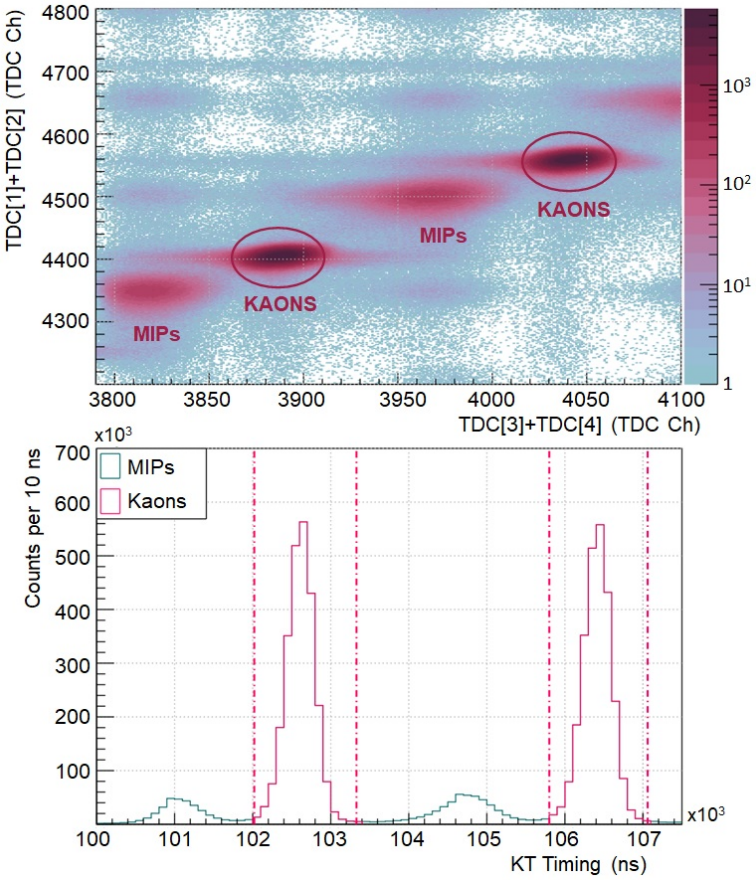

Figure 60: *Top:* Scatter plot of the mean time on the upper and lower scintillators of the kaon trigger for the 1.4% LHeD run. *Bottom:* Diagonal projection of the KT mean time, with the selected kaon events in magenta.

Moreover, the SDD timing information was used to further reduce the asynchronous background, as previously described for SIDDHARTINO. Only events in the marked regions of the TDC spectra shown in Fig. 62 were selected. During those runs, the SDDs were kept at an average temperature of $\sim$ 132 K, reducing the FWHM of the main peak in the timing spectrum and thus the electrons' drift time to the anode to 450 ns (see Fig. 62 top panel) for a target density of 1.4% LHeD, and to 444 ns for a target density of 1.1% LHeD (Fig. 62 bottom panel). During the SIDDHARTINO runs, the SDD temperature was

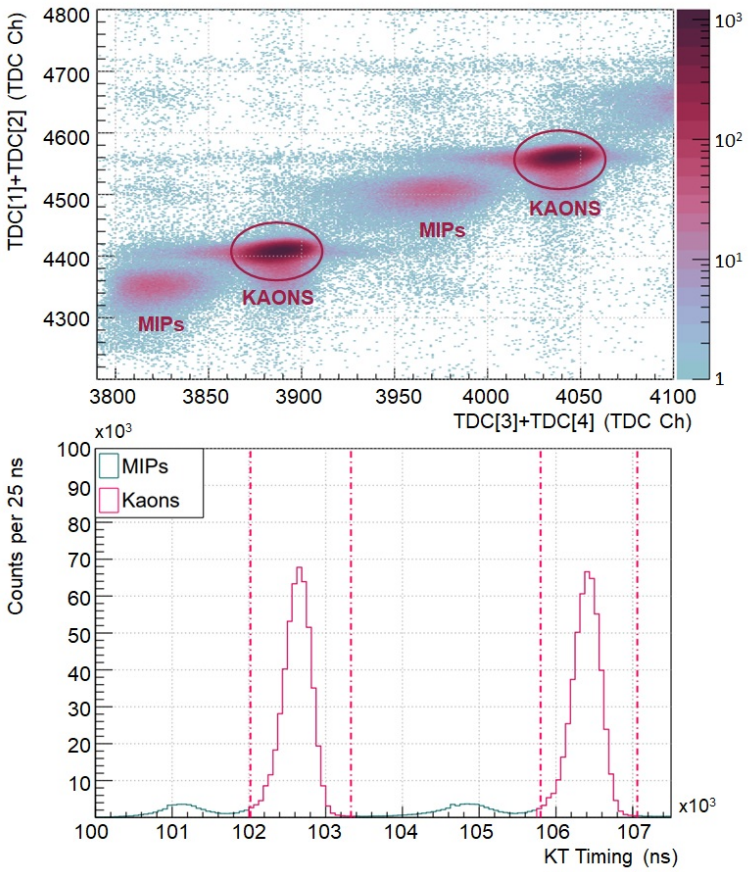

Figure 61: *Top:* Scatter plot of the mean time on the kaon trigger scintillators for the 1.1% LHeD run. *Bottom:* Diagonal projection of the KT mean time. The magenta regions again represent the selected kaon events.

approximately 170 K; the decrease in temperature improved the drift time by a factor of ~ 2. Besides those three established background reduction tools, the veto systems were in operation during the final run with a helium target in July 2022. They therefore provided an additional method to clean the X-ray spectrum from background according to the method described in Sec. 9.3.
After the background reduction, a fit was applied to the final kaonic ^{4}He X-ray spectrum to extract the $3d \rightarrow 2p$ transition results. The fit function included the same components and parameters as described in 8.2.3 (see Table 15), except for the description of the background shape. Now, the background was described using the sum of a constant and an exponential function. A χ^2 fit was performed using the Minuit2 minimizer package included in ROOT, resulting in a reduced χ^2 of 1.1 (ndf = 280). Fig. 63 shows the summed kaonic helium-4 X-ray spectrum with the applied fit function in dark magenta. Additionally, the main components of the fit function are plotted. In light cyan, the employed background function is shown. The main Gaussian components of the K^{4}He L_α, L_β, and L_γ lines are drawn in light magenta.
The final results for the kaonic ^{4}He ($3d \rightarrow 2p$) transition, obtained from the

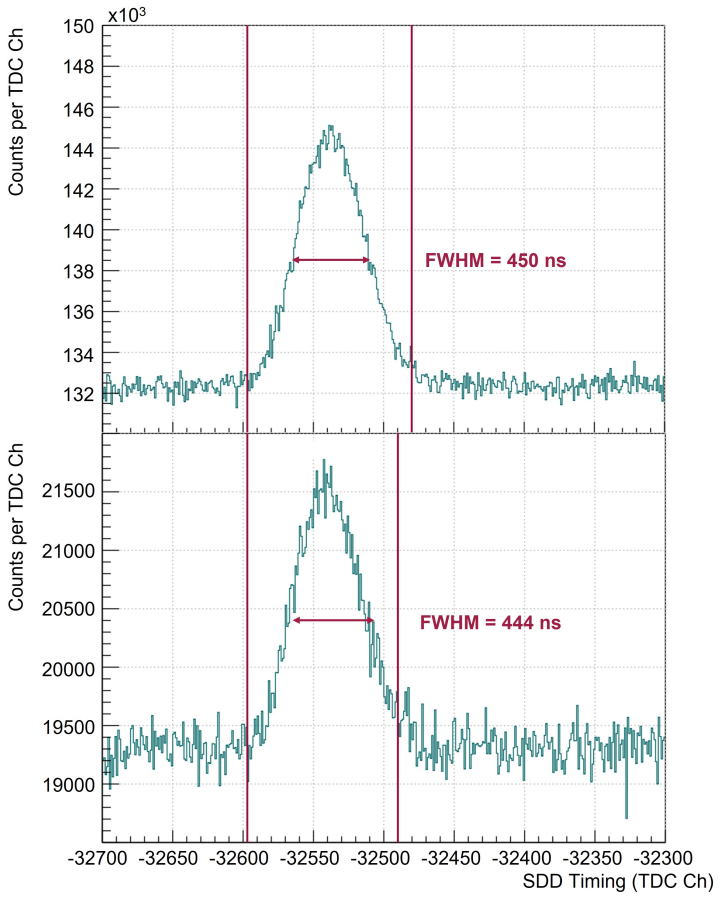

Figure 62: SDD timing spectra in coincidence with a K^+K^- signal in the kaon trigger for the SIDDHARTA-2 helium run with a gas density of 1.4% LHeD (*top*) and 1.1% LHeD (*bottom*). The SDDs' drift time was reduced to 450 ns and 444 ns (FWHM), respectively.

fit, are listed in Tables 20, 21, and 22. The transition energy was found to be $(6463.44 \pm 0.95_{\text{stat}} \pm 2.00_{\text{syst}})$ eV, resulting in a $2p$ level shift of $(0.44 \pm 0.95_{\text{stat}} \pm 2.00_{\text{syst}})$ eV. The statistical uncertainty, extracted from the fit and corrected for the reduced χ^2, has now been decreased to 0.95 eV, while the SDDs' energy resolution was found to be 155 eV. The systematic uncertainty was evaluated in terms of the influence of the bin width and varying functions for the background description. The uncertainty based on these analysis aspects was found to be 0.95 eV, leaving the stability of the SDDs as the main source of systematic uncertainty of the transition energy and shift. For the result of the $2p$ level width, the variation of bin width and background description did not have a measurable effect and the systematic uncertainty was found to be negligible compared to the large statistical uncertainty of 10.1 eV (see Tab. 22).
Compared to previous measurements [2]–[4], [64], [116], the earlier results (listed in Tables 20, 21, and 22) and the newly obtained values are in agree-

ment within one standard deviation, confirming the findings of the E570 and SIDDHARTA collaborations. Moreover, they are also compatible with theoretical predictions: calculations using optical potentials anticipate a $2p$ level shift ε_{2p} in ^{4}He of (-0.13 ± 0.02) eV or (-0.14 ± 0.02) eV, depending on the approach to describe the nucleon density distribution of the $\overline{\text{K}}$-He system [62]. For the $2p$ level width Γ_{2p}, they predict values of (1.8 ± 0.05) eV or (1.7 ± 0.05) eV, respectively [62]. Another approach using an SU(3) chiral unitary model produces similar predictions [63]. In [117] a coupled-channels approach predicts larger widths ($\Gamma_{2p} > 5$) eV, which can be excluded based on the obtained results.

The new result represents the first measurement of kaonic helium-4 at DAΦNE with sub-eV level statistical precision. The E62 experiment which implemented a TES spectrometer instead of SDDs achieved the most precise K^{-4}He result with both statistical and systematic uncertainties of below 1 eV. The TES spectrometer attained an energy resolution of 5.5 to 5.7 eV [4], which is a factor $\sim$ 25 higher than for the SDDs. Despite this significant difference, a total uncertainty of less than 3 eV was achieved with the SDDs. This new measurement by SIDDHARTA-2 provides the most precise result obtained with SDDs and thus puts strong restrictions on the expected shift and width of kaonic helium-4.

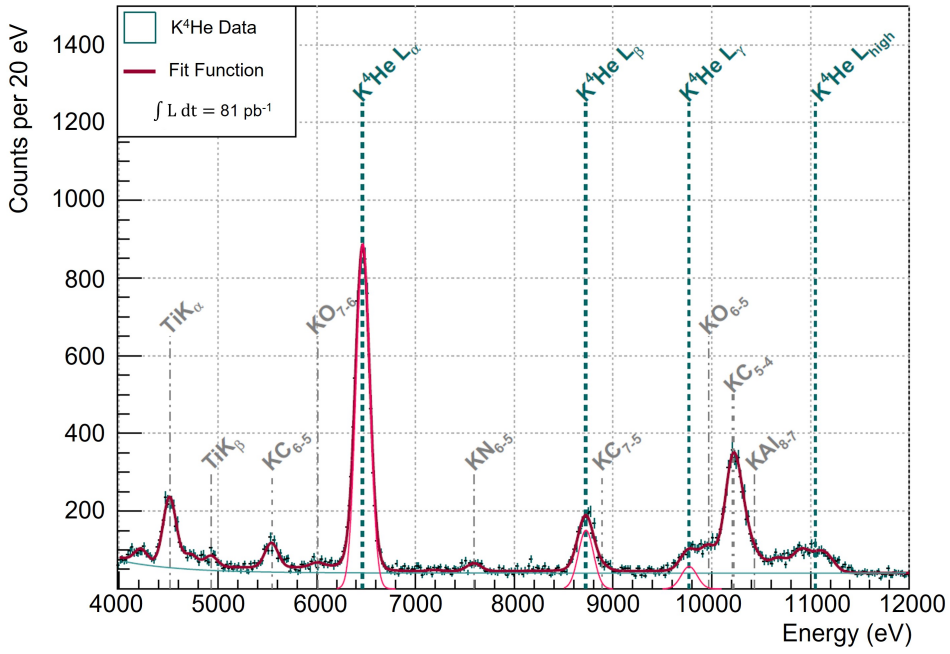

Figure 63: Final kaonic ^{4}He spectrum with summed SIDDHARTINO and SIDDHARTA-2 data. The global fit function (dark magenta), as well as its main components (background function in light cyan and main Gaussian peaks in light magenta for the K^{4}He L lines) are shown.

Table 20: Comparison of results of the kaonic ^{4}He $3d \rightarrow 2p$ X-ray transition energy for past measurements and the newly obtained result from the sum of SIDDHARTINO and SIDDHARTA-2 data.

Experiment	**Energy (eV)**
E570 [64]	$6467 \pm 3 \pm 2$
SIDDHARTA [2], [3]	$6463.6 \pm 5.8 \pm 2.0$
E62 [4]	$6463.7 \pm 0.3 \pm 0.1$
SIDDHARTINO [116]	$6463.7 \pm 2.5 \pm 2.0$
This work	$6463.44 \pm 0.95 \pm 2.00$

Table 21: Comparison of results for the kaonic ^{4}He $2p$ level shift ε_{2p} for past measurements and the newly obtained result from the sum of SIDDHARTINO and SIDDHARTA-2 data.

Experiment	ε_{2p}**(eV)**
E570 [64]	$2 \pm 2 \pm 2$
SIDDHARTA [2], [3]	$0 \pm 6 \pm 2$
E62 [4]	$0.2 \pm 0.3 \pm 0.2$
SIDDHARTINO [116]	$0.2 \pm 2.5 \pm 2.0$
This work	$0.44 \pm 0.95 \pm 2.00$

Table 22: Comparison of results for the kaonic ^{4}He $2p$ level width Γ_{2p} for past measurements and the newly obtained result from the sum of SIDDHARTINO and SIDDHARTA-2 data.

Experiment	Γ_{2p}**(eV)**
E570 [64]	-
SIDDHARTA [2], [3]	$14 \pm 8 \pm 5$
E62 [4]	$1.0 \pm 0.6 \pm 0.3$
SIDDHARTINO [116]	8 ± 10
This work	0.6 ± 10.1

9.2 Transitions in Kaonic Atoms from Solid Materials

The charged kaons produced by DAΦNE not only stop inside the gas volume of the target cell, but also in the target cell entrance window, sidewalls and solid structures. The entrance window and sidewalls are made of Kapton foils with a molecular formula of $C_{22}H_{10}N_2O_5$; the solid structures of the target cell consist of aluminium frames. Therefore, in the X-ray spectra obtained by SIDDHARTINO and SIDDHARTA, several transition lines from kaonic carbon, nitrogen, oxygen and aluminium are present besides the kaonic helium lines. X-ray spectroscopy of kaonic atoms with atomic numbers across the periodic table was of great interest in the 1970s and 1980s, with measurements spanning from kaonic lithium to kaonic uranium [59], [60], [118]–[127]. These measurements provide input to theoretical descriptions of the low-energy antikaon-nucleon interaction up to this date. As made evident by the "kaonic hydrogen puzzle" [52], [64], [66] and the "kaonic helium puzzle" [59], [61]–[63], however, they are implicated by large uncertainties. With the advent of new detector technologies giving rise to a new generation of kaonic atom spectroscopy experiments like KpX, DEAR, and SIDDHARTA, the reliability of the existing database was called into question. Hence, new, precise experimental input of measurements of intermediate-weight kaonic atoms can provide a solid database for theory [128]. The following section describes the analysis of a combination of SIDDHARTINO and SIDDHARTA data to extract the transition energies of higher-n kaonic carbon, nitrogen, oxygen, and aluminium transitions, which were reported for the first time by the SIDDHARTA-2 collaboration in an analogous, independent analysis [129], with differences in the energy calibration of the SDDs.

In this analysis, a total of 92.5 pb^{-1} of data were considered, including the SIDDHARTINO empty target data, as well as data from all He densities collected with both SIDDHARTINO and SIDDHARTA-2. Since the SIDDHARTINO degrader with a mean thickness of 750 µm contained a zirconium foil with characteristic X-rays at $\sim$ 15.7 keV [109] in the expected kaonic aluminium ROI, the data accumulated with this degrader configuration were not included.

The background reduction tools described previously were applied to the data, including the kaon trigger, kaon ToF cut and SDD timing cut. The resulting X-ray spectrum is shown in Fig. 64. A fit was performed to extract the desired transition energies. The fit function follows the description given in Sec. 8.2.3 with only slight differences. The background shape now is described by the sum of a constant and an exponential function (see Fig. 64 in light cyan). Apart from the kaonic helium lines, Gaussian functions with an exponential low-energy tail are used to reproduce the line shapes of the kaonic atom transitions, since for these intermediate mass, high-n transitions, the effects of the strong interaction on the energy level are far below the energy resolution of the SDDs. The Gaussian peaks are shown in light magenta in Fig. 64 for all newly measured transitions. Since the fit now covers a larger energy range,

for the transition lines with energies > 9700 eV, the slope of the tails was chosen differently from the lower-energy tails to account for differences in the charge-carrier collection at higher energies. The mean values of the Gaussian functions for the kaonic aluminium ($7 \rightarrow 6$), kaonic carbon ($5 \rightarrow 4$), kaonic nitrogen ($5 \rightarrow 4$), and the kaonic oxygen ($6 \rightarrow 5$) transitions were left as free parameters. The distances of the remaining kaonic Kapton lines to these transitions were fixed for each Z. The final fit function describes the data with a reduced χ^2 of 1.7 (ndf = 521). Table 23 lists the transition energies for the observed kaonic carbon, oxygen, nitrogen, and aluminium lines obtained from the fit. It also lists the reference values obtained from solving the Klein-Gordon equation and applying corrections due to vacuum polarisation and recoil effects [130]–[132], which have not been published to-date [64]. The statistical uncertainty was extracted from the fit results and corrected for the reduced χ^2. The systematic uncertainty is determined by the stability of the SDDs for X-ray energies up to $\sim$ 7 keV; at higher energies, the non-linearity of the SDDs is the dominant factor, as discussed in Sec. 7.4. The effects of different bin widths and background functions was studied and found to be negligible within the statistical uncertainty of the individual results.

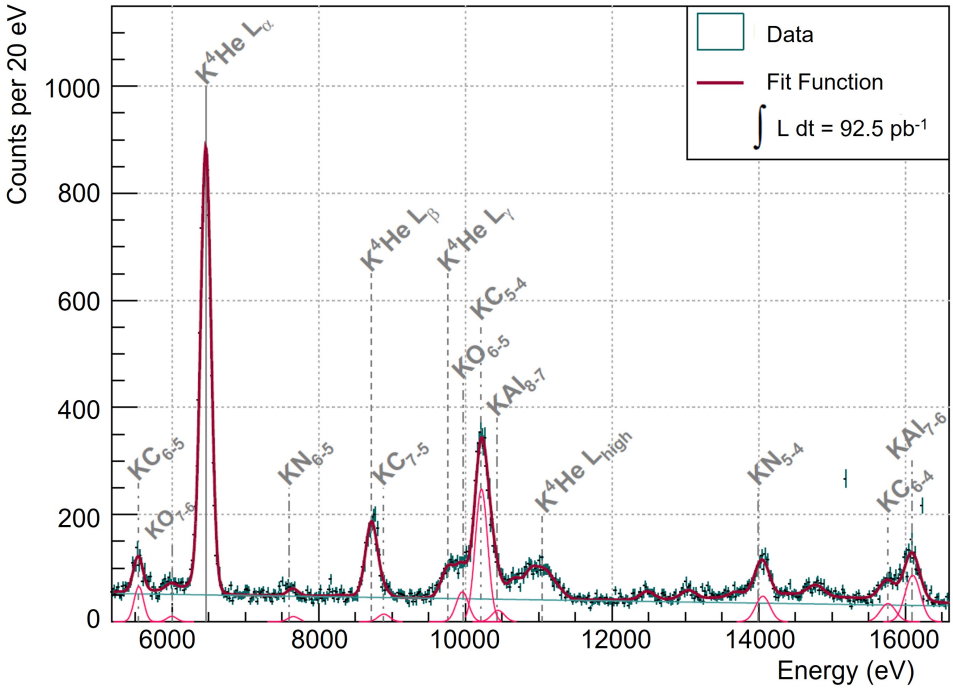

Figure 64: Energy spectrum summed for all SIDDHARTINO and SIDDHARTA-2 helium gas densities including empty target data. The fit function is shown in dark magenta. Transition lines from kaonic helium-4, carbon, nitrogen, oxygen and aluminium are clearly visible.

The obtained results represent the first ever measurements of these transition energies [129]. For kaonic carbon and aluminium, they agree with the theoretical values within one σ; for kaonic oxygen and nitrogen, theoretical and

experimental results are in agreement within two σ. The measurement of kaonic transitions in solid materials can provide valuable input to the theory describing the low-energy antikaon-nucleon interaction. While the cascade process in light, gaseous media has been theoretically studied in the past [6], [71], [75], [133], it is not well understood in solids to this day. Moreover, the role of multi-nucleon absorption processes in the interaction of kaons and nuclei needs further investigation [8], [134], [135]. Measurements of several transitions in the same kaonic atom enable the determination of transition probabilities, which contribute to the understanding of the contribution of absorption processes of the kaon. While the transitions measured in the framework of this thesis are too high to directly study the effects of the strong interaction, they can enrich the existing database and incentivise further measurements in intermediate-mass kaonic atoms to motivate the development of new theoretical descriptions.

Table 23: Transition energies for the observed kaonic C, O, N, and Al lines with statistical and systematic uncertainties, and the calculated values [115].

Transition	**Energy from Fit (eV)**	**Ref. Value (eV)**
K^-C $(7 \to 5)$	$8882.0 \pm 2.9 \pm 3.7$	8885.8
K^-C $(6 \to 5)$	$5541.1 \pm 2.9 \pm 2.0$	5544.9
K^-C $(6 \to 4)$	$15\,755.6 \pm 2.9 \pm 8.7$	15 759.4
K^-C $(5 \to 4)$	$10\,212.7 \pm 2.9 \pm 7.4$	10 216.5
K^-O $(7 \to 6)$	$5990.5 \pm 10.5 \pm 2.0$	6006.8
K^-O $(6 \to 5)$	$9952.4 \pm 10.5 \pm 7.4$	9968.7
K^-N $(6 \to 5)$	$7648.1 \pm 7.8 \pm 3.7$	7595.4
K^-N $(5 \to 4)$	$14\,048.6 \pm 7.8 \pm 8.7$	13 995.9
K^-Al $(8 \to 7)$	$10\,439.1 \pm 6.7 \pm 7.4$	10 435.1
K^-Al $(7 \to 6)$	$16\,092.3 \pm 6.7 \pm 8.7$	16 088.3

9.3 Performance Analysis of the Veto Systems

For the first kaonic deuterium run and the final kaonic helium run of the 2022 beam time of SIDDHARTA-2, the full veto system including the Veto-1, Veto-2, and charged kaon detector, was in operation for the first time. In this section, the methods of background reduction for each of these systems are explained. Their interplay and performance are discussed. Since the Veto-2 system is a focal point of this thesis, special attention is paid on the performance of this part of the veto system and it is studied in terms of its timing capabilities and efficiency. The effect of the combined veto systems on the X-ray spectra for deuterium and helium is discussed.

9.3.1 Application of the Veto Systems for Background Reduction

All three components of the veto system, the charged kaon detector, Veto-1, and Veto-2 system, are in charge of actively suppressing synchronous background. The charged kaon detector, placed below the bottom scintillator of the kaon trigger, distinguishes between events with either a K^+ or K^- reaching the target cell via timing information. The stop of a K^- in the detector results in the capture of the kaon by the surrounding atoms and its eventual absorption, and thus in the prompt emission of MIPs within, at most, 1 ns. A K^+, however, is not captured into a kaonic atom after it is slowed down in the detector, but decays after its mean lifetime of 12.4 ns [5]. The detection of a K^+ in the charged kaon detector thus results in a delayed emission of MIPs. This difference in timing is used in the analysis to reject the events for which a positively charged kaon reached the target cell. Fig. 65 shows the TDC timing spectrum of the charged kaon detector obtained during the SIDDHARTA-2 1.1% LHeD run. The main peak corresponds to the promptly emitted MIPs after K^- absorption in the detector, i.e. the events in which a K^+ reached the target cell. Thus, it represents the events to be discarded in further analysis. The flat tail contains the desired events where the K^- was stopped in the target gas.

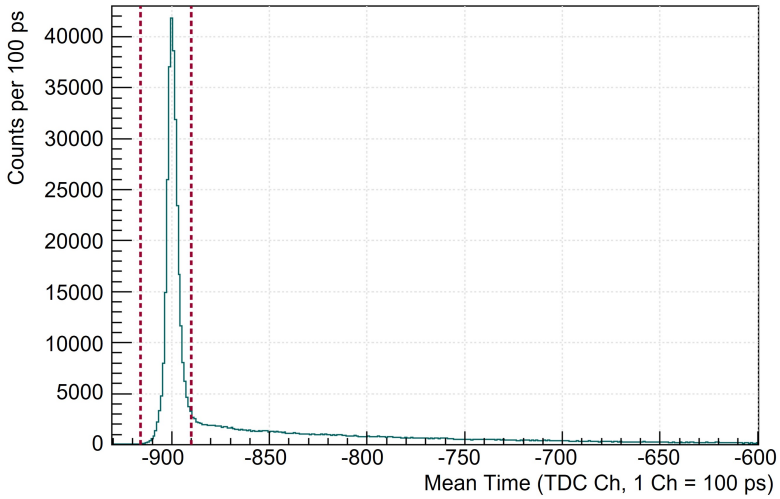

Figure 65: Mean time spectrum of the charged kaon detector. The dark magenta lines enclose the discarded events of prompt MIPs from K^- absorption in the detector, i.e. K^+ stops in the target cell.

In order to obtain the signature of a K^+ stopping in the target cell, information from the charged kaon detector is used. An event is discarded as a K^+ event when, in coincidence with a K^+K^- signal on the kaon trigger, the mean time of the charged kaon detector signal lies within the prompt gate.
The main purpose of the Veto-1 signal is the distinction between kaon stops in the target gas, and kaon stops in the solid materials of the setup. Since a

kaon stop and the subsequent formation of a kaonic atom, cascade, and final kaon absorption is much slower in gas than in a solid, timing information can be used for this distinction (see Fig. 21). The mean time spectrum summed for all twelve Veto-1 detector units on the condition of a kaon trigger signal is shown in Fig. 66. The first vertical line indicates the threshold between the left-hand shoulder of mean time from kaon stops in the setup material (shown in magenta) and the mean times corresponding to kaon stops in the target (shown in cyan). The cyan part of the distribution represents the events selected for analysis. The second vertical line divides the selected events and the events in the tail, corresponding to kaon stops in the titanium top of the target cell, as well as residual events produced by K^+ decays.

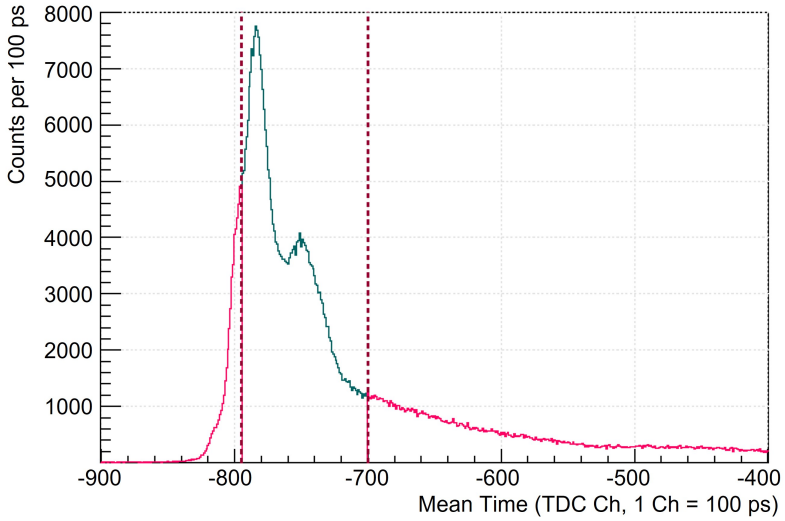

Figure 66: Mean time spectrum summed for all twelve Veto-1 units. The shoulder on the left (magenta) corresponds to kaon stops in solid materials; the distribution in cyan represents the desired kaon stops in the target cell. The magenta tail on the right corresponds to kaon stops in the upper window of the target cell and K^+ decays.

The remaining part of the time spectrum clearly shows a double-peak structure. The origin of this structure was investigated by selecting events with energies corresponding to transition lines from certain kaonic atoms or fluorescence lines. In particular, the $K^{-4}He$ L_α line, the titanium K_α line, the kaonic carbon ($5 \rightarrow 4$) transition line, the kaonic nitrogen ($6 \rightarrow 5$) transition line, and the kaonic aluminium ($7 \rightarrow 6$) transition line were chosen. The resulting timing spectra for the selected events are shown in Fig. 67, after the application of the kaon trigger and SDD drift time cuts. Using the timing information given by the Veto-1, a distinction between the place of origin of the kaonic atom transitions present in the X-ray spectrum is possible. Since the target cell entrance window consists of Kapton, the kaonic carbon and kaonic nitrogen transitions correspond to shorter mean times in the Veto-1 than the kaonic helium transitions. The kaons do not reach the target gas, but are stopped in

the Kapton foil instead. The kaonic aluminium transitions most likely originate from the bottom ring of the target cell, also resulting in a generally shorter mean time in the Veto-1 than the kaonic helium transitions. As visible in the top panel of Fig. 67, the distribution of the mean time of kaonic aluminium has a tail towards longer times. The target cell also has aluminium frames along the length of the cylinder; some kaons will reach these structures, resulting in a delay in the mean time compared to the bottom ring or target gas. The titanium transitions originate from kaons stopping in the top of the target cell which consists of high-purity titanium. The cyan selected part of the spectrum in Fig. 66 thus mainly corresponds to events from kaon stops in the gas. The Veto-1 system can thus be used to suppress transitions in the ROI by using timing information; moreover, it can enhance the understanding of the distribution of kaons in the setup and target and the degrader configuration.

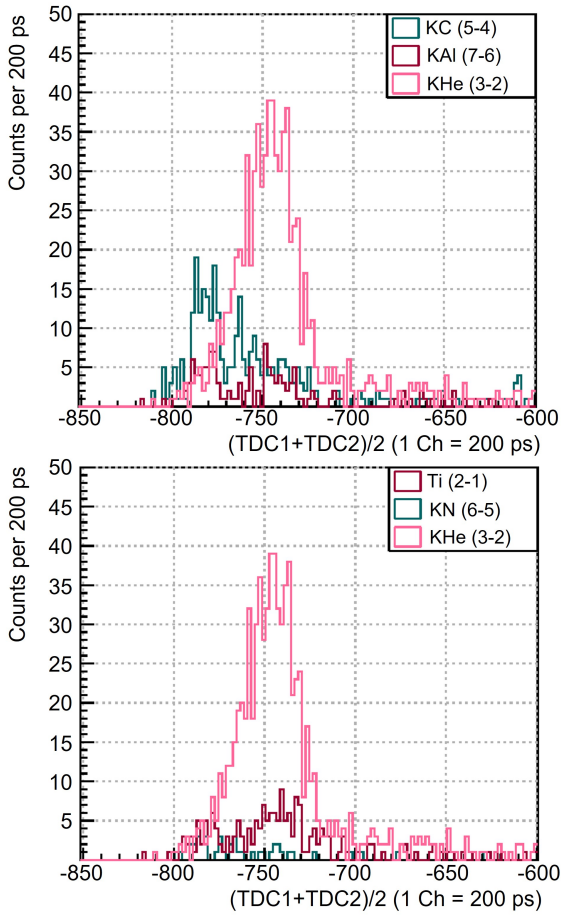

Figure 67: *Top:* Mean time distribution in the Veto-1 system for kaonic carbon ($5 \rightarrow 4$) (cyan), kaonic aluminum ($7 \rightarrow 6$) (dark magenta), and kaonic helium ($3 \rightarrow 2$) events (light magenta). *Bottom:* Mean time distribution for titanium ($2 \rightarrow 1$) (dark magenta) and kaonic nitrogen ($6 \rightarrow 5$) (cyan), again in comparison to kaonic helium ($3 \rightarrow 2$) events (light magenta).

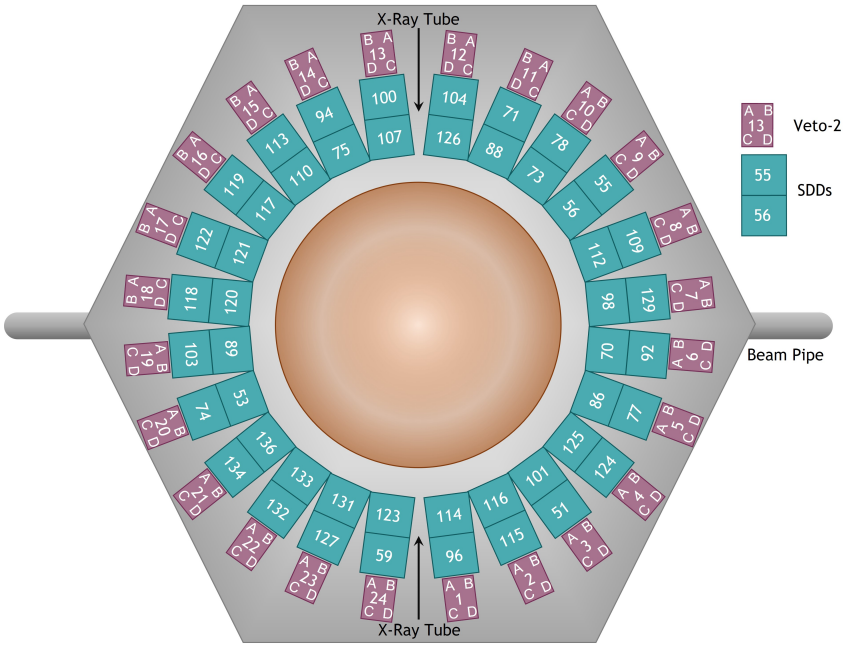

Figure 68: Mapping of SDDs to Veto-2 detectors in the SIDDHARTA-2 apparatus. One box of four Veto-2 counters (A, B, C, and D) in magenta corresponds to two SDD arrays (cyan).

The topological correlation between signals in the SDDs and the Veto-2 system is used to suppress background from the kaon-nucleon absorption, as explained in Sec. 5.1.3. Therefore, the Veto-2 detectors had to be mapped to the SDD arrays according to the setup shown in Fig. 68. Each box of four Veto-2 counters covers two SDD arrays, i.e. 16 SDD cells. Since the MIPs can pass through the SDDs and Veto-2 not only head-on but at various angles, more than one Veto-2 detector had to be correlated to each SDD cell. Only considering one Veto-2 detector directly behind the SDD cell significantly lowered the efficiency of the Veto-2 system, as discussed in Sec. 9.3.3. As depicted in Fig. 69, eight Veto-2 counters per SDD cell were accounted for in the analysis, including four detectors in the box directly behind the SDD array, as well as two neighbouring units on each side. If a signal was detected in an SDD channel and one of those eight Veto-2 counters within a 5 µs time window after a kaon trigger, the event was considered to be a background event and discarded.

9.3.2 Veto-2 Timing Capabilities

The time-over-threshold TDC spectra for four of the 96 channels are shown in Fig. 70. The ToT is the result of the difference between the time signal of the trailing and the leading edge and is proportional to the signal amplitude of the SiPM, and thus to the energy loss of the particle detected in the scintillator. The threshold for the ToT signals was set to values from −180 mV to −200 mV

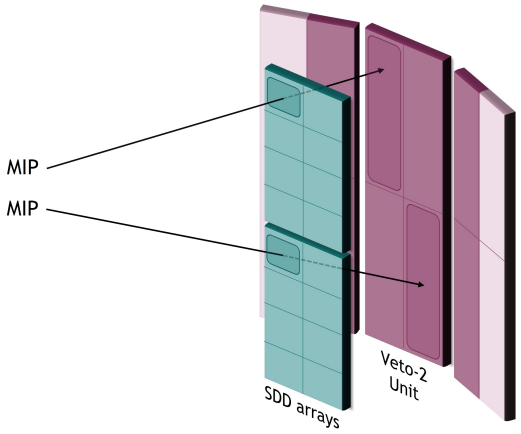

Figure 69: Topological correlation between SDD and Veto-2 hits.

during the calibration procedure performed at SMI before their installation at LNF. The ToT spectra in Fig. 70 therefore show an edge at shorter ToTs which corresponds to the set threshold. Since MIPs are expected to produce signals with amplitudes of > 300 mV in the SiPMs, the threshold was chosen conservatively low, but could be changed off-line in the analysis. The DAQ of the Veto-2 recorded the leading and trailing edges of the ToT signals in NIM standard provided by the amplification boards for each channel.
Since the time resolution of the Veto-2 system was determined to be < 1 ns at SMI, the Veto-2 system should be capable to distinguish between kaon stops in the target gas and kaon stops in the solid setup components analogously to the Veto-1. Fig. 71 shows the leading edge time signals summed for all Veto-2 channels in coincidence with a kaon trigger during the SIDDHARTA-2 1.1% LHeD run. As was the case for the Veto-1 system, a double-peak structure is visible in the distribution. An analysis analogous to the one for the Veto-1 system was performed for the Veto-2 system and datasets representing several kaonic atom and fluorescence transition lines were selected. The resulting time spectra are shown in Fig. 72, which indicate a similar behaviour to the Veto-1 system. The right-hand panels show the correlation between the energy of the X-ray detected in the SDDs and the leading edge timing in the Veto-2 system. The transitions with the highest statistics in the X-ray spectrum, i.e. the $K^{-4}He$ L_α and K^-C $(5 \rightarrow 4)$ transition lines, appear as clusters in the scatter plot. The lines originating in the target cell entrance window or bottom ring are associated with a faster signal in the Veto-2 with respect to the kaon trigger than the X-rays produced in the helium gas. This leads to the conclusion that the Veto-2 system, in addition to the suppression of hadronic background, is capable to distinguish between kaon stops in the gas and in solids and to determine the location of origin of the observed X-ray lines like the Veto-1. Thus, the Veto-2 can contribute to the tuning and optimisation of the degrader configuration and target gas density. This provides an additional lever to reduce background and to improve the signal-to-background ratio for the kaonic deuterium measurement.

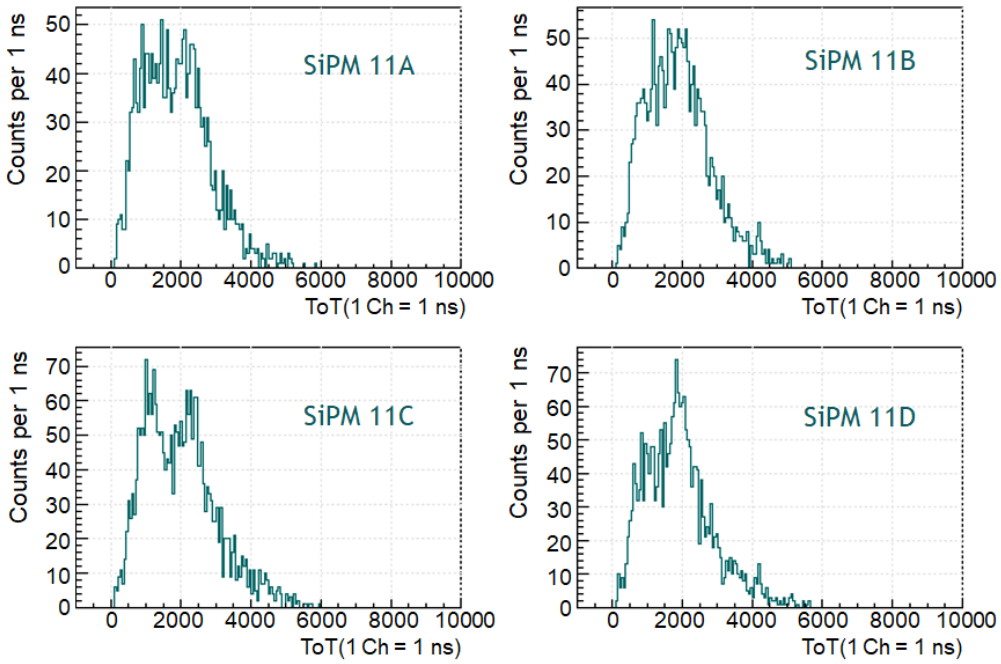

Figure 70: Time over threshold spectra for four Veto-2 detectors during the 1.1% LHeD run.

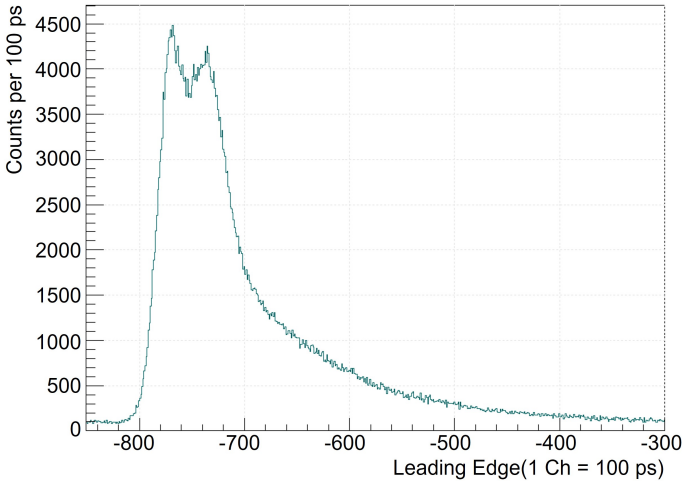

Figure 71: TDC spectrum of the leading edge time signals summed for all Veto-2 detectors during the 1.1% LHeD run.

9.3.3 Efficiency of the Veto-2 System

As described in Sec. 6.1.2, the intrinsic detection efficiency of the Veto-2 system has been determined at SMI using cosmic rays, and was found to be $> 99\%$ [94], [95]. Its efficiency in the context of the SIDDHARTA-2 apparatus

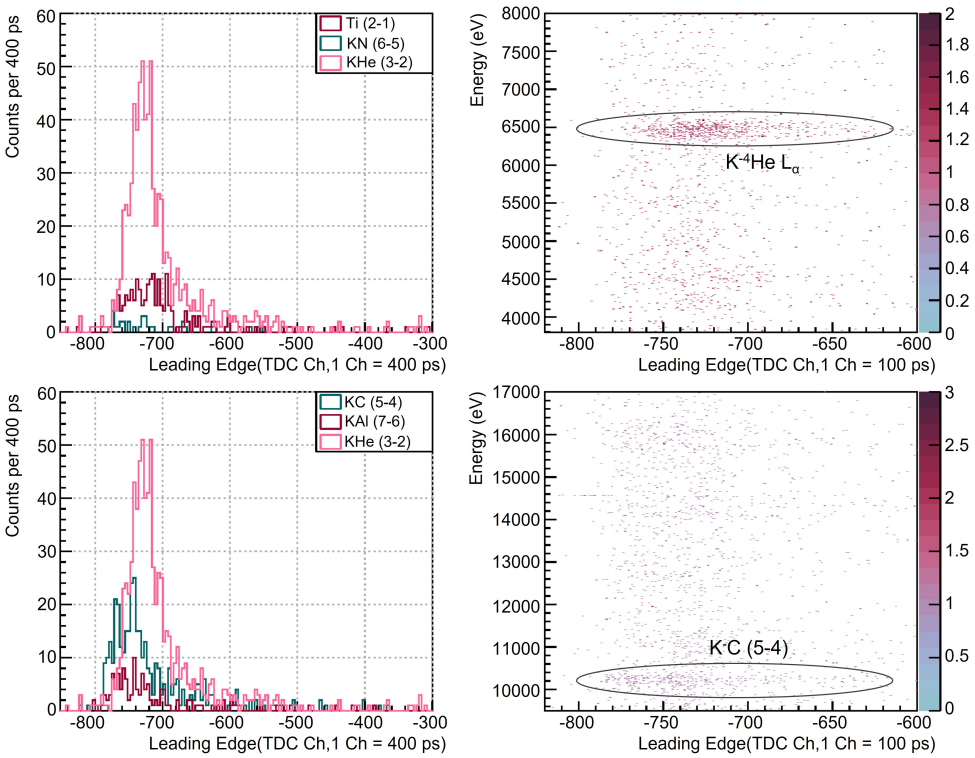

Figure 72: *Top left:* Time distribution for titanium ($2 \rightarrow 1$) (dark magenta), kaonic nitrogen ($6 \rightarrow 5$) (cyan) and kaonic helium ($3 \rightarrow 2$) events (light magenta) in the Veto-2 system. *Top right:* Correlation of SDD X-ray energy and Veto-2 timing for an energy range of 3800 - 8000 eV. The $K^{-4}He$ L_α cluster is circled. *Bottom left:* Time distribution for kaonic carbon ($5 \rightarrow 4$) (cyan), kaonic aluminium ($7 \rightarrow 6$) (dark magenta), again compared to kaonic helium ($3 \rightarrow 2$) events (light magenta). *Bottom right:* Correlation of SDD X-ray energy and Veto-2 timing for an energy range of 9800 to 17000 eV. The $K^{-}C$ ($5 \rightarrow 4$) transition shows as a cluster (circled).

and the collider environment, however, is expected to differ from its intrinsic efficiency given the particle composition of the background and the geometry of the setup. Thus, it has to be studied.
Since the main purpose of the Veto-2 system is the suppression of SDD hits by MIPs from the kaon-nucleon absorption, a condition had to be set to select MIP events in the data. Therefore, only events within a 5 µs coincidence with the kaon trigger and within the accepted kaon trigger ToF window (see Fig. 61) were considered. Moreover, an SDD hit with an energy of > 20 keV was requested, since MIPs passing through the SDDs' active area are expected to produce high-energy events. However, there are still kaonic X-ray transitions present in this energy region which would not lead to a signal in the Veto-2 system. Therefore, a coincidence of a > 20 keV signal in an SDD and a signal in the topologically correlated Veto-1 counters was required. The geometry of this coincidence in SDDs and Veto-1 detectors and the respective Veto-2 detectors

is depicted in Fig. 73. For each column of SDD arrays, two Veto-1 units are considered to allow for grazing hits or events produced off-centre in the target cell. Given a coincidence of a signal in one of the two Veto-1 detectors and the SDD, eight Veto-2 detectors (dark magenta) are monitored for a signal to determine the Veto-2 efficiency. The number of coincidences Σ_{coinc} and the number of events with a signal in one of the eight Veto-2 channels Σ_{V2} are summed up for the deuterium run data and the 1.1% LHeD helium data each. The Veto-2 efficiency ϵ_{V2} is then determined via

$$\epsilon_{\text{V2}} = \frac{\Sigma_{\text{V2}}}{\Sigma_{\text{coinc}}}. \tag{53}$$

Table 24: Results for the Veto-2 efficiency in the SIDDHARTA-2 setup.

Target	Σ_{V2}	Σ_{coinc}	ϵ_{V2}
1.1% LHeD	7671±87	12 422±111	0.62 ± 0.01
1.04% LDD	63 161±251	110 096±332	0.57 ± 0.01

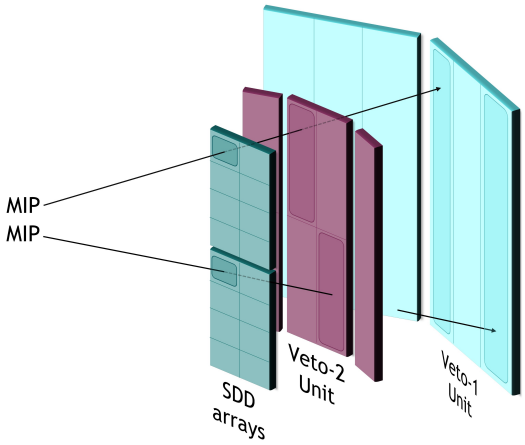

Figure 73: Geometry of the Veto-2 efficiency study.

The efficiencies obtained for the He and D data in this configuration are listed in Table 24, with their statistical uncertainties determined via Poissonian statistics. The described topology was chosen to account for grazing hits and the stopping distribution of kaons in the target cell. Fig. 74 and 75 show (a) the distributions of stopped kaons in the target volume with projections on the (b) x-, (c) y-, and (d) z-axis obtained from a GEANT4 MC simulation [136]. Since the kaon stops are spread throughout the entire volume of the target cell, the emitted MIPs can pass through the SDDs and veto systems at a non-perpendicular angle. Thus, one MIP can produce signals in an SDD and veto counters which are not directly aligned. This is made evident when only the Veto-2 detector directly behind the respective SDD cell is considered in the determination of the Veto-2 efficiency. For the helium data, the efficiency then drops from 0.62 ± 0.01 to 0.23 ± 0.01; for deuterium, it decreases from

0.57 ± 0.01 to 0.22 ± 0.01. For efficient suppression of the hadronic background, all four Veto-2 detectors directly aligned with the SDD array as well as the next two detectors in the neighbouring units have to be correlated with each single SDD cell. In comparison with the intrinsic efficiency of $> 99\%$, the efficiency within the SIDDHARTA-2 setup is significantly smaller for both helium and deuterium targets. This eludes to the presence of random coincidences in SDDs and the Veto-1 system, not originating from kaon related MIPs but a different component of the background. Since the 5 µs coincidence window with the kaon trigger is used, the electromagnetic background or background from beam interactions could induce signals in the Veto-1 detectors within the accepted time window. Depending on their particle type or direction of flight, they would not necessarily also produce a signal in the respective Veto-2 detectors. This would lead to a decrease of the observed detection efficiency.

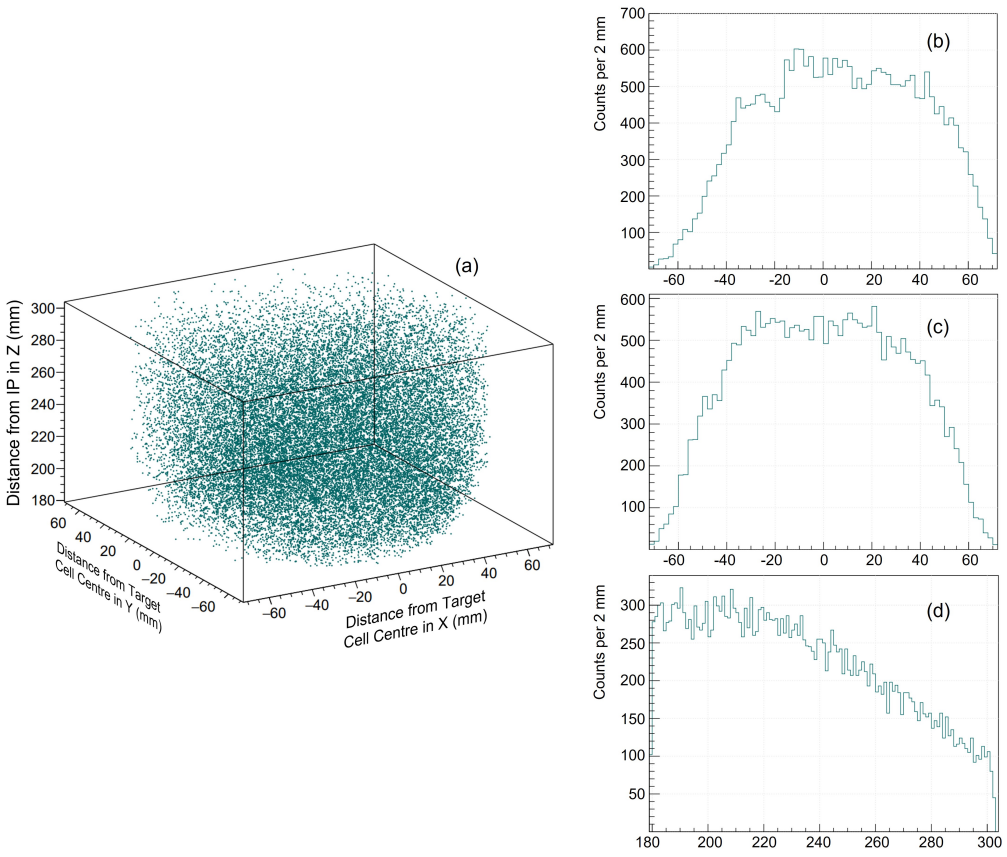

Figure 74: (a) GEANT4 simulated distribution of kaon stops in the target cell volume for 1.4% LHeD. (b) Projection of the kaon stop distribution on the x-axis. (c) Y-axis projection of kaon stops in the target cell. (d) Projection of the kaon stop distribution on the z-axis, along the height of the cylindrical target cell. *Adapted from [136].*

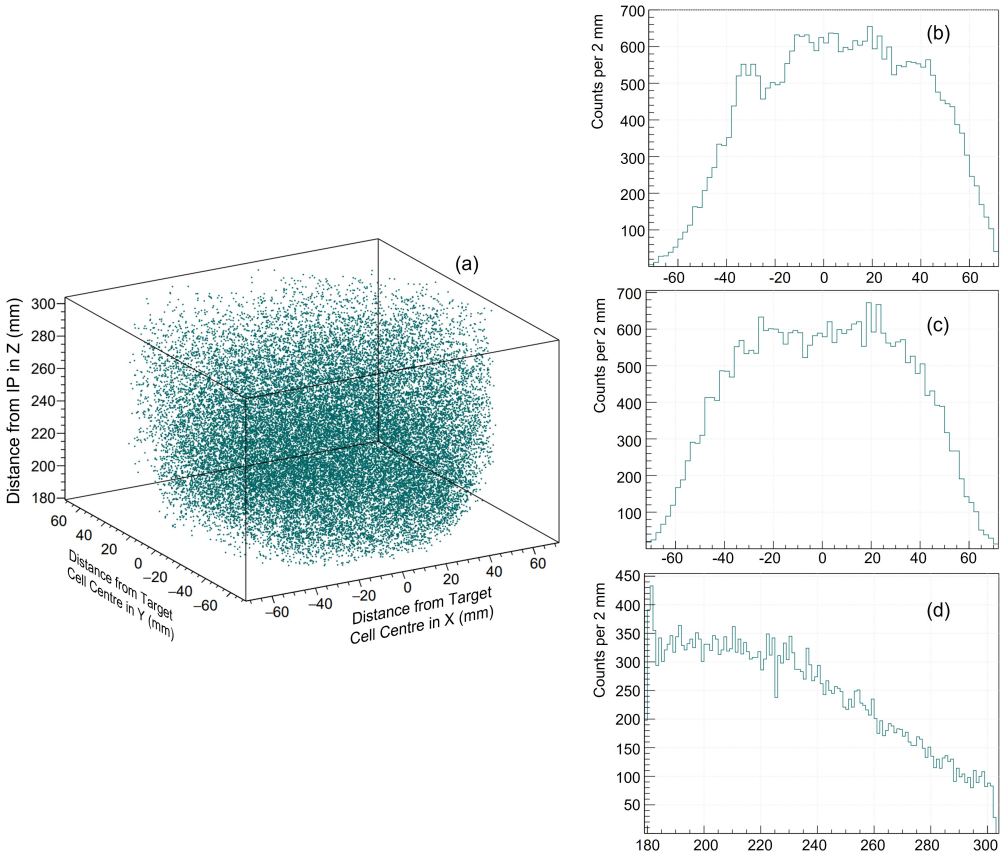

Figure 75: (a) GEANT4 simulated distribution of kaon stops in the target cell volume for 1.04% LDD. (b) Projection of the kaon stop distribution on the x-axis. (c) Y-axis projection of kaon stops in the target cell. (d) Projection of the kaon stop distribution on the z-axis, along the height of the cylindrical target cell. *Adapted from [136].*

The multiplicity of signals in the Veto-2 system per kaon trigger also hint at a high level of background not related to the kaon absorption on the nucleons. According to the reaction channels listed in Tables 3 and 4, a multiplicity of two or three is expected for the Veto-2 system for each triggered kaon. As indicated in Fig. 76, in many cases, more than three Veto-2 detectors show a signal. Thus, the values obtained for the Veto-2 efficiency actually provide an instrument to study the composition of the background present in the runs rather than an accurate measure of the detector efficiency. They can be used to improve the apparatus to reduce the effects of the background radiation. As discussed in Sec. 10, the passive shielding against electromagnetic and beam background will be increased for the upcoming SIDDHARTA-2 beam times. The veto systems not only actively suppress background, but in addition provide a useful tool to improve the qualitative and quantitative understanding of the background in the DAΦNE environment, which is of particular importance for the challenging kaonic deuterium measurement.

Another factor to be taken into account is the high-radiation environment in

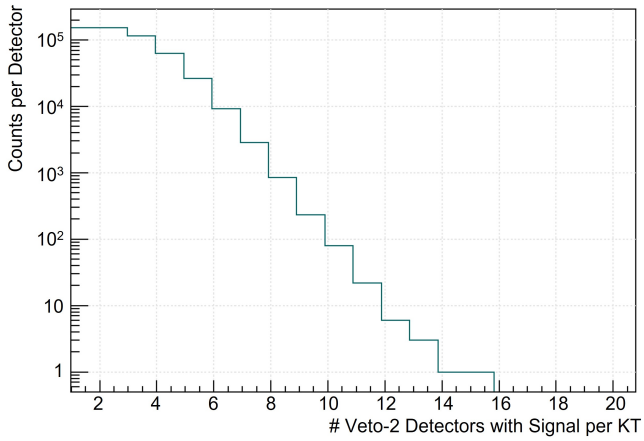

Figure 76: Multiplicity of Veto-2 Detectors for the 1.1% LHeD run on the condition of a K^- reaching the target cell.

which the detectors are installed. As evidenced by the past, the SiPMs suffer from radiation damage in the DAΦNE collider hall. Despite the implementation of updated electronics to keep the detectors operable even in the case of radiation damage, possible effects on the performance of the Veto-2 system cannot be excluded. Radiation damage leads to a rise in dark count rate in the SiPMs. In combination with incorrect settings of the SiPMs' gain and threshold for the ToT signals, this could lead to afterpulsing in the digital signals, or the treatment of electronic noise as a MIP signal to be discarded, which could harm the signal-to-noise ratio of the measurement. Since there are no calibrated ToT data available of the SiPM output during the analysed beam times, the possible effects of radiation damage are difficult to quantify. However, the time performance, TDC output, and overall efficiency of the Veto-2 system hint at a satisfactory operation of the detectors, which proves the effect of the implemented modifications to its front-end electronics. In Sec. 10 an update of the Veto-2 system is described in detail, to further improve its performance for the approaching period of beam time for SIDDHARTA-2.

9.3.4 Complete Veto Background Reduction

Following a sufficient understanding of the suppression mechanisms provided by the veto systems, their background rejection factor is the next step to characterise their performance in the SIDDHARTA-2 setup. Therefore, the effect of the Veto-2 system on the signal-to-background ratio for the dataset obtained with a target of 1.1% LHeD was studied. For the deuterium data, this analysis could not be performed since the kaonic deuterium signal is not yet visible in the spectrum.
In Fig. 77, the kaonic helium X-ray spectrum is shown after each step of background reduction. The signal-to-background ratio of the kaonic helium-4 L_α

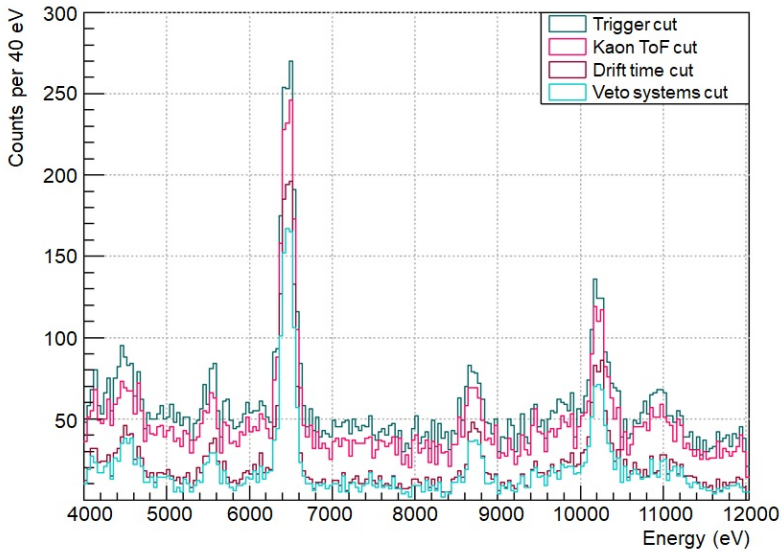

Figure 77: Kaonic helium-4 spectrum for 1.1% LHeD after each respective step of background reduction: kaon trigger (dark cyan), kaon ToF cut (light magenta), SDD drift time cut (dark magenta), and the veto systems (light cyan).

transition was determined for the spectra after application of the trigger cut (dark cyan), after application of the drift time cut (dark magenta), and after application of the complete veto systems, i.e. the Veto-1, Veto-2, and kaon detector (light cyan).
A fit was applied to the spectra as described in previous sections; the fit function was modelled after the description in Sec. 8.2.3 to obtain the transition energy for the $K^{-4}He$ L_α line. The transition line was described in the fit by a Voigtian function and a low-energy tail, while the background shape was reproduced by the sum of a constant and an exponential function. The Voigtian lineshape and the background function are shown for each spectrum in Fig. 78. To determine the signal intensity, the amplitude of the Voigtian curve at the obtained transition energy was extracted from the fit. The amplitude of the background function was evaluated for 50 equidistant energies in the range from 7000 to 8000 eV, and the mean value was calculated. The ratio of these two values represents the signal-to-background ratio.
After the application of the kaon trigger to the raw SDD energy spectrum, the signal-to-background ratio of the $K^{-4}He$ L_α transition was approximately 5 (see top panel of Fig. 78). The additional application of the SDD drift time cut increased the ratio by a factor four to approximately 18 (Fig. 78). The effect of the Veto-2 system on the S/B is shown in panel *(c)* of Fig. 78. Its application according to the method described in Sec. 9.3.1 reduced the hadronic background component. It improved the S/B from approximately 18 to approximately 20, resulting in an increase of $\sim$ 16%. In a final step, the Veto-1, Veto-2, and the charged kaon detector were used in combination to

further suppress the background.

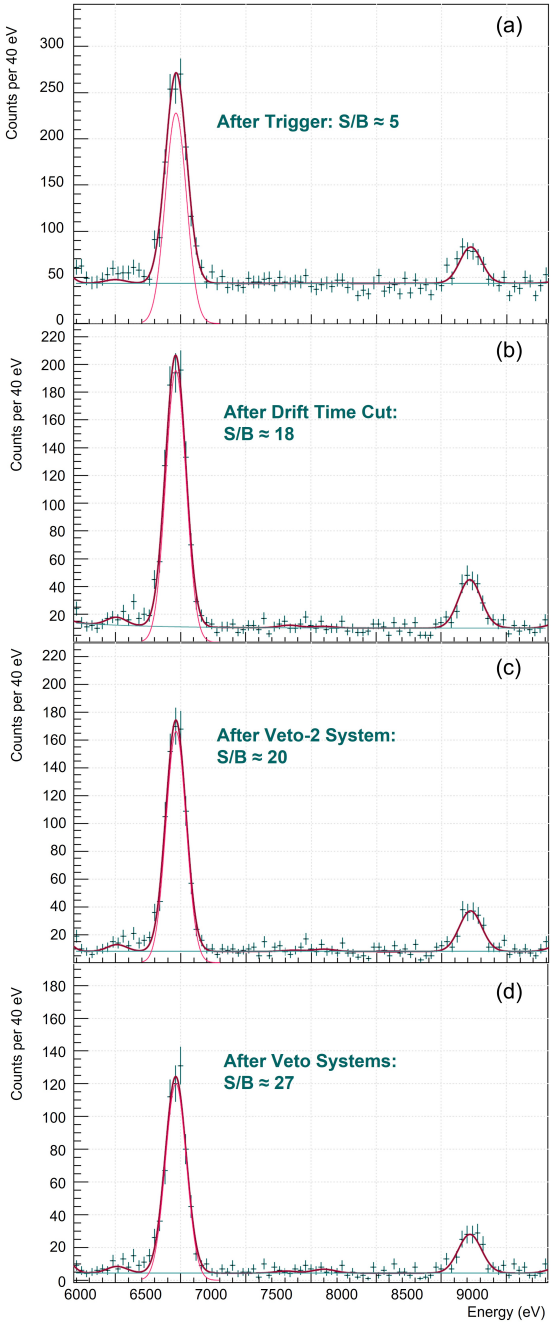

Figure 78: *(a)* 1.1% LHeD $K^{-4}He$ spectrum after application of the kaon trigger cut. The S/B was determined from the fit. *(b)* Helium spectrum after the drift time cut, improving the S/B to ~ 17. *(c)* After application of the Veto-2 system, the S/B increased by to ~ 20. *(d)* Final spectrum after the combined application of the charged kaon detector, Veto-1, and Veto-2 system. The S/B was further increased to ~ 27.

The contribution of events for which a K^+ reached the target cell was reduced by the charged kaon detector. The Veto-1 system suppressed background ori-

ginating from kaon stops in the solid structures of the setup via timing information. In the resulting kaonic helium spectrum after the veto system cuts, the signal-to-background ratio improved to approximately 27 (see the bottom panel of Fig. 78). This corresponds to an improvement of $\sim 55\%$.
Since kaonic helium data including the veto systems was only acquired for an integrated luminosity of ~ 5 pb^{-1}, a precise and reliable quantitative prediction of the background rejection factors for the veto systems is difficult to provide. However, the increases in the S/B after application of the veto systems indicate their correct operation and will be particularly important for the challenging measurement of kaonic deuterium.

9.4 A First Analysis of Kaonic Deuterium

Starting in June 2022, a first run with a deuterium target was performed with the SIDDHARTA-2 apparatus for an integrated luminosity of 29.8 pb^{-1}. The target gas had a density of 1.04% LDD and was kept at a temperature of ~ 27 K and a pressure of 1.1 bar. All 48 SDD arrays and the complete veto system were in operation for the deuterium run.

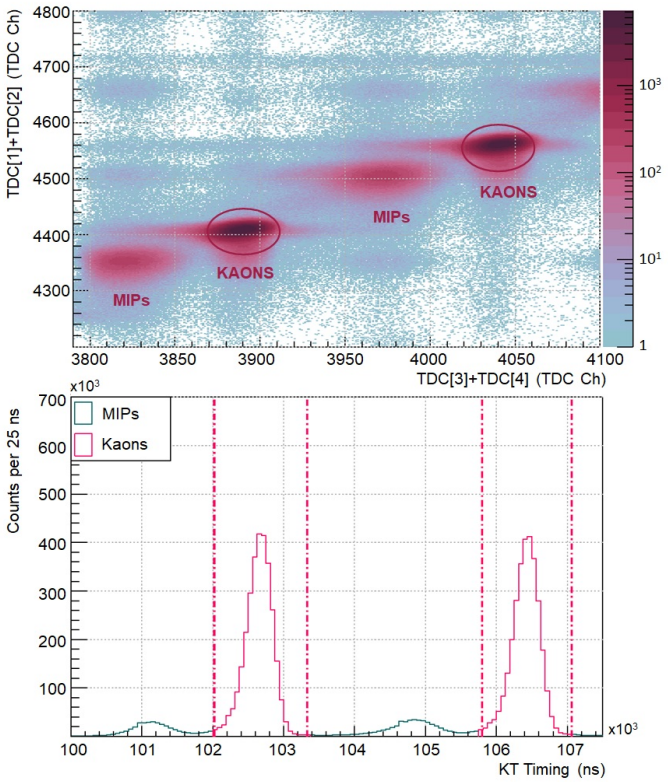

Figure 79: *Top:* Scatter plot of the mean time on the kaon trigger scintillators for the 1.04 % LDD run. *Bottom:* Diagonal projection of the KT timing, with the selected kaon events in magenta.

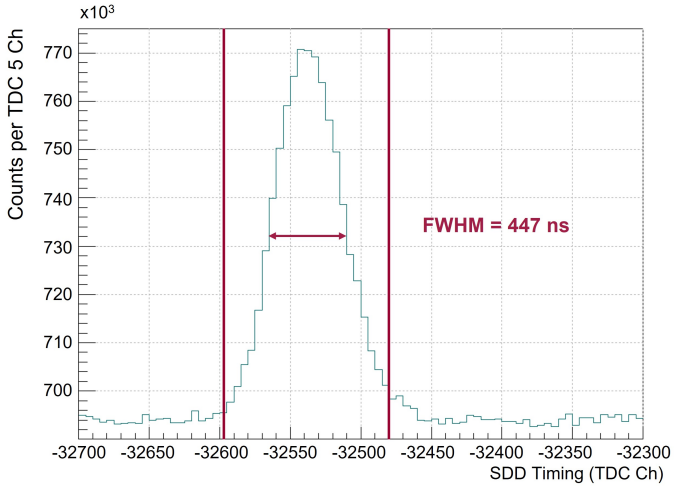

Figure 80: SDD timing spectrum for the SIDDHARTA-2 deuterium run. The vertical lines enclose the kaon-correlated selected events.

For the kaonic deuterium measurement, a precise understanding of the background composition is of even greater importance than for the previously performed kaonic hydrogen or helium measurements. As mentioned in Sec. 5, the K^-d K_α X-ray yield is expected to be, at most, a tenth of the kaonic hydrogen yield [68], [70], [71], and the ground state width Γ_{1s} is predicted to be approximately twice as large as in kaonic hydrogen. Hence, the rare desired kaonic deuterium signal has to be preserved, while the background has to be suppressed as far as possible. Analogously to the kaonic helium analysis, the kaon trigger was used for the kaonic deuterium measurement to reduce asynchronous background from beam-beam and beam-environment interactions. A triple coincidence in signals in both kaon trigger scintillators and the SDDs was again required to define a trigger with a rejection factor of 1.14×10^4. Moreover, the ToF measured by the KT was used to select the charged kaon events, as shown in Fig. 79. This suppressed the background in the deuterium ROI by an additional factor of 1.62. The SDDs' timing in coincidence with the kaon trigger further reduced the asynchronous background by only selecting kaon-correlated events within the main peak of the TDC spectrum in Fig. 80. The background rejection factor of this drift time cut in the K^-d ROI was found to be 3.03. In addition to these methods, the charged kaon trigger, and the Veto-1 and Veto-2 systems were used as described in the previous Sec. 9.3 for active background suppression. Their contribution to the background rejection was discussed in Sec. 9.3.4. In total, the combination of all background suppression cuts led to a rejection factor of 6.7×10^4 (see Fig. 81). A summary of all the different cuts is given in Table 25. Additionally, the ratio between events with a kaon-correlated origin and uncorrelated background events is of interest for a further understanding of the background conditions. As described for the helium analysis in Sec. 8.2.2, the SDD timing information is used for this comparison. The integral of events in the main peak

of Fig. 80 was calculated, representing the number of kaon-correlated events. The integral over an equally wide region on the flat plateau corresponds to the number of uncorrelated background events. For the first kaonic deuterium run of SIDDHARTA-2, the ratio between the two integrals was found to be $(1.59 \times 10^7)/(1.50 \times 10^7) = 1.06$. This is in agreement with the conditions found during the SIDDHARTA kaonic hydrogen measurement [101], as well as during the SIDDHARTINO kaonic helium runs.

Table 25: Background rejection factors for the ROI of kaonic deuterium.

Cut	Number of events in ROI	Rejection Factor
No Cut	8.8×10^8	-
Trigger	77021	1.14×10^4
Kaon selection via ToF	47667	1.62
Drift time selection	15711	3.03
All cuts	13202	6.7×10^4

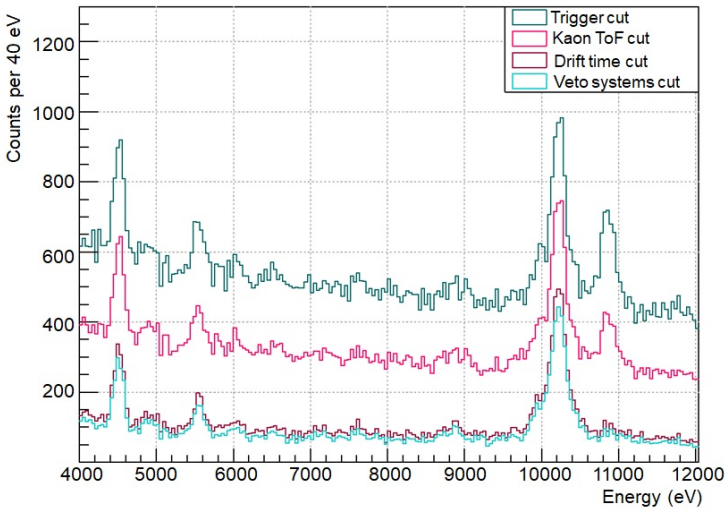

Figure 81: Kaonic deuterium X-ray spectrum after each step of background reduction: kaon trigger (dark cyan), kaon ToF cut (light magenta), SDD drift time cut (dark magenta), and the veto systems (light cyan).

The resulting X-ray spectrum is shown in Fig. 82. The K-series transition energies in kaonic deuterium derived from the Klein-Gordon equation with vacuum polarisation and recoil corrections, only considering electromagnetic interactions, are listed in Table 26 [115]. Assuming a ground state energy shift ε_{1s} of -800 eV, the K^-d K_α transition energy can be expected at 7034 eV. The transitions from higher n states to the ground state, i.e. the $(4p \rightarrow 1s)$ transition and higher, all appear at energies in close proximity to each other. They thus will not be individually resolvable in the SIDDHARTA-2 X-ray spectrum, but will rather present as a cluster called $K_{complex}$. A first attempt to fit the kaonic deuterium spectrum in the energy range from 4 to

12 keV was made. The proposed fit function includes 35 free parameters. The background shape is reproduced by the sum of a linear and an exponential function. Voigtian curves and exponential tails are used to describe the K^-d K_α, K_β, and $K_{complex}$ transition lines, where the Lorentzian linewidth Γ_{1s} of the Voigtian function represents the broadening due to the strong interaction. Since the shift due to the strong interaction is equal for all K-series transitions, the distances between the K^-d K_β and $K_{complex}$ transition lines to the K_α line were fixed. The intensities of these higher K-series transitions are incorporated into the fit as their relative amplitudes compared to the K_α line.

Table 26: K-series transition energies for kaonic deuterium, taking only electromagnetic effects into account [115].

Transition		**Transition Energy (eV)**
K_α	$2p \rightarrow 1s$	7834.0
K_β	$3p \rightarrow 1s$	9280.2
$K_{complex}$	$4p \rightarrow 1s$	9786.2
	$5p \rightarrow 1s$	10020.4
	$6p \rightarrow 1s$	10147.6
	$7p \rightarrow 1s$	10224.3
	$8p \rightarrow 1s$	10274.1

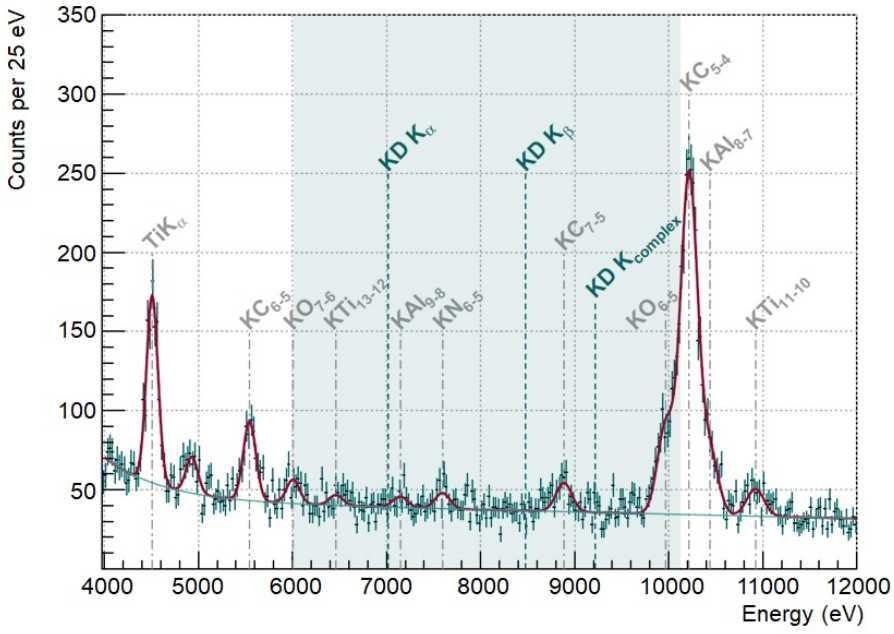

Figure 82: X-ray spectrum with the 1.04% LDD target. The ROI is indicated by the light cyan background, and the possible positions of the K^-d K_α, K_β, and $K_{complex}$ transition lines are marked, assuming a $1s$ shift of -800 eV. A first fit function is shown in dark magenta.

All remaining transition lines from other kaonic atoms or fluorescence lines are described by Gaussian functions and the exponential tails according to the SDDs' response function discussed in Sec. 7.1. The complete fit function is listed in Appendix B. Table 27 lists all components of the fit function. The fit function describes the X-ray spectrum well with a reduced χ^2 of 1.1 (ndf = 278). In the resulting spectrum, the kaonic deuterium K-series lines are not visible above the background level.

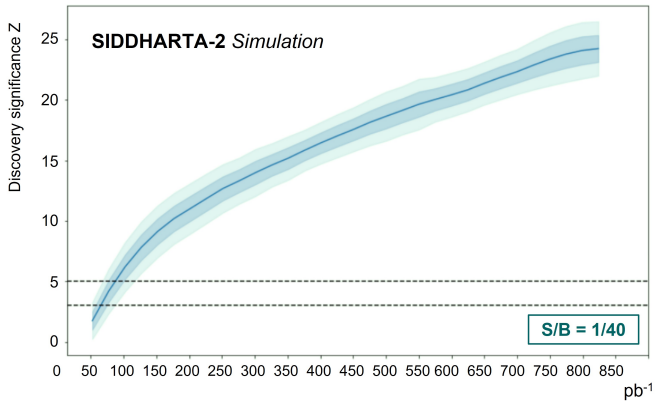

Figure 83: Simulated significance of the detection of the kaonic deuterium K-series transitions in relation to the collected integrated luminosity. *Adapted from [137].*

A simulation on the signal sensitivity was performed for the SIDDHARTA-2 kaonic deuterium measurement, assuming a $1s$ shift of -600 eV, a $1s$ width of 800 eV, and a K^-d K_α yield of 0.02 X-rays/(cm^2/pb^{-1}) [137]. The simulation performed a hypothesis test based on the profile likelihood ratio using Wilks' theorem [138]. The signal significance Z was determined as $Z = \Phi^{-1}(1 - p_0)$, with Φ being the Gaussian cumulative distribution function, and p_0 the p-value of the test statistic. According to this simulation, for a signal-to-background ratio of 1/40, an integrated luminosity of $\sim$ 40 pb^{-1} of collected data would result in the detection of the K^-d K-series transition lines with 5-σ significance (see Fig. 83). The first SIDDHARTA-2 run with a deuterium target only accumulated an integrated luminosity of 29.8 pb^{-1} and the signal-to-background ratio during this run is still unknown. Thus, a clean signature of the kaonic deuterium K-series transitions could not yet be expected. The goal of the SIDDHARTA-2 experiment is to accumulate data with a kaonic deuterium target for an integrated luminosity of 800 pb^{-1}; as indicated in Fig. 83, this corresponds to a K^-d K-series detection significance of approximately 20 - 25 σ. Moreover, the X-ray spectrum in Fig. 82 suggests an additional issue for the measurement of the kaonic deuterium K-series X-rays - the presence of transition lines from kaonic aluminium, kaonic carbon, and kaonic oxygen in the ROI. The kaonic aluminium ($9 \rightarrow 8$) or kaonic nitrogen ($6 \rightarrow 5$) transition lines could potentially overlap the K^-d K_α line, depending on the observed ε_{1s}. These kaonic X-rays originate from kaon stops in the target cell frames

and Kapton entrance window. Sec. 10 presents updates to the experimental apparatus currently in preparation to reduce the contamination of kaonic nitrogen and oxygen transitions in the X-ray spectrum. This first run of the SIDDHARTA-2 experiment with a deuterium target represents the the beginning of a long-awaited measurement campaign. It provided an important test of the experimental apparatus in difficult conditions. While the detectors and veto systems proved their functionality for this challenging measurement, this run also motivated the development of possible improvements to the apparatus for the upcoming beam time (see Sec. 10).

Table 27: Parameters of the proposed fit function to describe the kaonic deuterium X-ray spectrum.

Function Component	**Parameter**
Background function	$p_{0,\text{const}}$ $p_{1,\text{lin}}$, $p_{2,\text{lin}}$ $p_{3,\text{exp}}$, $p_{4,\text{exp}}$
SDD energy resolution	Fano factor Constant noise
Global energy shift	Shift
K^-d parameters	K^-d $(2 \to 1)$ mean value K^-d $(2 \to 1)$ width Γ_{1s} K^-d $(2 \to 1)$ amplitude K^-d $(3 \to 1)$ / K^-d $(2 \to 1)$ relat. ampl. K^-d $(4 \to 1)$ / K^-d $(2 \to 1)$ relat. ampl. K^-d $(5 \to 1)$ / K^-d $(2 \to 1)$ relat. ampl. K^-d $(6 \to 1)$ / K^-d $(2 \to 1)$ relat. ampl. K^-d $(7 \to 1)$ / K^-d $(2 \to 1)$ relat. ampl. K^-d $(8 \to 1)$ / K^-d $(2 \to 1)$ relat. ampl.
Other included lines	K^-C $(5 \to 4)$ ampl. K^-C $(6 \to 5)$ / K^-C $(5 \to 4)$ relat. ampl. K^-C $(7 \to 5)$ / K^-C $(5 \to 4)$ relat. ampl. K^-O $(6 \to 5)$ / K^-C $(5 \to 4)$ relat. ampl. K^-O $(7 \to 6)$ / K^-C $(5 \to 4)$ relat. ampl. K^-N $(6 \to 5)$ / K^-N $(5 \to 4)$ relat. ampl. K^-N $(7 \to 6)$ / K^-C $(5 \to 4)$ relat. ampl. K^-Al $(8 \to 7)$ / K^-C $(5 \to 4)$ relat. ampl. K^-Al $(9 \to 8)$ / K^-Al $(8 \to 7)$ relat. ampl. K^-Ti $(11 \to 10)$ / K^-C $(5 \to 4)$ relat. ampl. K^-Ti $(12 \to 11)$ / K^-Ti $(11 \to 10)$ relat. ampl. K^-Ti $(13 \to 12)$ / K^-Ti $(11 \to 10)$ relat. ampl. Ti K_α ampl. Ti K_β / Ti K_α relat. ampl.
Tail components	Tail shift Universal tail gain Universal tail slope

10 Future Perspectives

In preparation for the upcoming beam times of 2023 and 2024, the SIDDHARTA-2 apparatus is currently undergoing several updates.
The first run with a deuterium target demonstrated the presence of transition lines from kaonic carbon, nitrogen, oxygen and aluminium in the kaonic deuterium ROI. They originate from kaon stops in the target cell entrance window made of Kapton foil, and the bottom aluminium ring of the target cell. While it is difficult to eliminate the carbon, several solution are tested to remove the contributions of kaonic nitrogen or oxygen and reduce kaonic aluminium. Instead of Kapton foil, the new target cell entrance window could be made of ultra-high-molecular-weight polyethylene (UHMWPE). UHMWPE is a polymer based on ethylene (C_2H_4) and consists of large molecular chains of carbon and hydrogen atoms [139]. Due to the long molecular chains, UHMWPE is a resistant material with high impact strength. Another option under review is mylar foil, a polyethylene terephthalate (PET), which would eliminate the contributions of kaonic nitrogen. The aluminium bottom ring of the target cell will also covered with the new material.
A second modification to the setup was an update to the cooling system of the SDDs. Up to now, the cooling of the target cell and SDD system was coupled and the SDDs were cooled along the coldfinger to the target cell. Now the cooling supplies for the target and SDDs was de-coupled at the first cooling stage of the two-stage closed-cycle helium refrigerator. This modification increases the cooling power for the target cell, which was previously inhibited by the fact that the SDDs cannot be cooled down further than 120 K. A lower target cell temperature allows for a higher gas pressure and thus increased stopping power in the target gas.

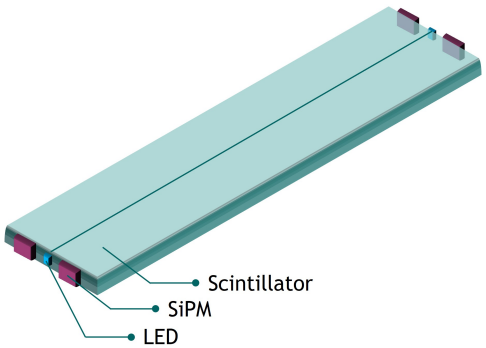

Figure 84: Updated Veto-2 design for the 2023/2024 beam times. The number of scintillators per Veto-2 unit was reduced from four to two.

Since the new cooling system for the SDDs slightly increased the radius of the Veto-2 system surrounding them and changes in the detector size were necessary, an opportunity to update the design of the Veto-2 detectors was presented. The analysis of the Veto-2 system's performance during its first

periods of operation indicated that the granularity of the Veto-2 detectors can be reduced without loss of efficiency. With the described design each SDD cell correlates to eight Veto-2 counters in the analysis. Therefore, the design of the veto system was adapted to reduce its granularity. The new design now only features two scintillators per detector box, as shown in Fig. 84. While the number of scintillators is now reduced, the number SiPMs remained unchanged and each scintillator now is read out on two sides. In this way, contributions from thermal noise in the SiPMs can be reduced by the requirement of coincidences in signals in both SiPMs on the same scintillator. The two-sided read-out also compensates for a possible loss in timing capabilities due to the larger scintillator size. The new scintillators now have a size of $(13 \times 5 \times 100)$ mm^3. Moreover, a new model of SiPMs manufactured by Broadcom is now used for the Veto-2 system. The SiPMs have an active area of (3.72×3.72) mm^2 with a peak sensitivity wavelength of 420 nm and 15060 microcells of size (30×30) μm^2 [140]. They are coupled to the scintillators with optical gel pads due to a height difference in the LEDs and SiPMs. The new system was constructed and calibrated at SMI.
To increase the solid angle of the Veto-1 system, an additional layer of scintillators with PMT read-out is planned to be placed below the vacuum chamber entrance window. This system is called the Veto-3 and will, analogous to the Veto-1 system, suppress background via timing information.
The goal of the SIDDHARTA-2 collaboration is the accumulation of approximately 800 pb^{-1} of total integrated luminosity. This data collection will likely be split into two beam times, starting in 2023 and possibly continuing into 2024. The kaonic atom research program at DAΦNE has a fruitful past, with the current SIDDHARTA-2 experiment as the conclusion to the final extraction of the isospin-dependent antikaon-nucleon scattering lengths, which will enable the constraint of the underlying theoretical models and motivate new developments in the theoretical field of the antikaon-nucleon interactions. But even after the successful completion of the kaonic deuterium measurement, several future experiments taking advantage of the ideal conditions provided by DAΦNE have been proposed [141], [142]. The introduced scientific program includes, for example, the measurement of transitions in selected heavy kaonic atoms, addressing the large uncertainty of the charged kaon mass [5] as well as the issues described in Sec. 9.2. Moreover, the development and application of new detector technologies is planned, like the implementation of 1 mm thick SDDs and Cd(Zn)Te detectors to increase the accessible energy range for kaonic atom X-ray spectroscopy. Evidently, the field of low-energy QCD still offers many research opportunities and open questions; the SIDDHARTA-2 experiment will finally lead to the answer of one of them.

11 Summary of Results and Conclusion

The framework of this thesis spans from detector development and characterisation at SMI in Vienna to their installation in the SIDDHARTA-2 apparatus at the DAΦNE collider, and concludes with the analysis of the kaonic helium-4 data and a first look at data collected with a deuterium target.

The design of the Veto-2 system was updated and expanded after the detectors experienced radiation damage during their first installation in the DAΦNE hall. The front-end electronics were modified to enable the operation of the detectors despite the effects of the irradiation. Additionally, a LED-based calibration system was implemented for the Veto-2 system to monitor the SiPMs' performance in-situ during beam time. The veto systems completed their first runs of operation in the SIDDHARTA-2 setup in 2022, both with a helium-4 and a deuterium target. Their performance during those periods was studied in terms of their efficiency, timing capabilities, and contribution to background identification and suppression. The Veto-2 system efficiency within the SIDDHARTA-2 setup was found to be 0.62 ± 0.01 for the 1.1% LHeD target, and 0.57 ± 0.01 for the 1.04% LDD target. These results hint at a large component of background not correlated to the kaon-nucleon absorption, i.e. an electromagnetic contribution from beam-beam interactions due to the Touschek-effect and bremsstrahlung, which can be reduced with increased passive shielding. Moreover, the timing of the Veto-1 and Veto-2 systems was studied. It was established that beyond just the distinction between kaon stops in the target gas and stops in solid materials, the Veto-1 can be used to identify the place of origin of kaonic X-rays using timing information. While not originally intended in this way, this was also found to be true for the Veto-2 system. Both systems thus provide a useful tool to further suppress background originating from specific materials in the setup and to also contribute to the understanding and optimisation of the kaon stopping distribution. The veto systems have proven to be crucial to fully understand the background composition and thus enable its efficient elimination and suppression, despite their operation in challenging conditions. The Veto-2 was found to increase the signal-to-background ratio by approximately 16%, while the combined application of the charged kaon detector, the Veto-1 system, and the Veto-2 system improved the S/B in helium from 18 to 27.
The characterisation of the X-ray detection system consisting of SDDs was another focal point of this thesis. The SIDDHARTA-2 SDDs have an energy resolution of (155 ± 10) eV at 6.4 keV and, for a temperature of ~ 132 K, an electron drift time of approximately 450 ns. The linearity of their energy response was studied with a multi-element calibration target as a potential contribution to the systematic uncertainty of the SIDDHARTA-2 measurements. In an energy range from 4 - 15 keV, the SDD system shows a non-linearity of

≤ 8.7 eV, with a non-linearity of (-0.05 ± 0.78) eV at 6.4 keV. Its stability over time was determined by comparing the copper K_α transition energies obtained from the periodically performed calibration runs during the SIDDHARTINO phase. The energy response of the SDDs was found to be stable within 0.55 ADC channels, corresponding to ~ 2.0 eV. Hence, the systematic uncertainty introduced by the performance of the SDDs ranges from 2.0 eV for X-ray energies up to ~ 7 keV to 8.7 eV for energies of 15 keV and higher.

The experimental setup has proven its functionality and adequacy for the challenging kaonic atom spectroscopy in multiple runs of data acquisition with a gaseous helium target. Several gas densities of ^{4}He were implemented in the SIDDHARTINO and SIDDHARTA-2 experiments. These runs facilitated the optimisation of the setup, background characterisation, and a new high-precision measurement of the kaonic helium-4 ($3d \rightarrow 2p$) transition energy, energy shift ε_{2p}, and $2p$ level width Γ_{2p}. The transition energy and shift were determined to be $(6463.44 \pm 0.95_{\text{stat}} \pm 2.00_{\text{syst}})$ eV and $\varepsilon_{2p} = (0.44 \pm 0.95_{\text{stat}} \pm 2.00_{\text{syst}})$ eV, with a statistical uncertainty below 1 eV. The width of the $2p$ level was found to be $\Gamma_{2p} = (0.6 \pm 10.1)$ eV. These results represent the most precise measurement of kaonic helium-4 obtained with SDDs as X-ray detectors. The E62 collaboration achieved the overall most precise measurement using TES microcalorimeters with an energy resolution of 5.5 to 5.7 eV [4]. Despite the much larger energy resolution of the SDDs, a total precision of < 3 eV was achieved by SIDDHARTA. The new measurement is in agreement with previous results and confirms their findings [2]–[4], [64], [116]. Furthermore, it validates the theoretical predictions for the $2p$ level shift and width of kaonic helium-4 both from calculations using optical potentials [62] and using an SU(3) chiral unitary model [63]. Another approach based on a coupled-channels potential allowed for large shifts and widths in case of a deep enough potential [117]. Since the obtained results exclude large values for shift and width in K^{-4}He, stringent constraints are provided for the theoretical predictions, and the predictions of [117] can be ruled out.

In addition to the improved result on kaonic helium-4, several transitions from kaonic atoms with $Z > 2$ in the intermediate-mass range were measured for the first time. The X-ray spectrum resulting from the combined data collected with empty and He targets contains not only the transition lines from kaon stops in the target, but also transitions from kaonic atoms produced in the entrance window and solid structures of the target cell. The transition energies for the K^-C $(6 \rightarrow 5)$, K^-C $(7 \rightarrow 5)$, K^-C $(5 \rightarrow 4)$, and K^-C $(6 \rightarrow 4)$ were extracted for the first time. For K^-O, the $(7 \rightarrow 6)$ and $(6 \rightarrow 5)$, and for K^-N, the $(6 \rightarrow 5)$ and $(5 \rightarrow 4)$ transition energies were measured. Lastly, the transition energies of the kaonic aluminium $(8 \rightarrow 7)$ and $(7 \rightarrow 6)$ transitions were obtained. These results demonstrate the ability of the SIDDHARTA-2 apparatus to perform measurements of higher transitions in kaonic atoms from solid targets

and can thus motivate the development of similar measurements in the future. The antikaon-nucleon interaction at low energies to this day poses many open questions. Since the quantum cascade in kaonic atoms is a highly complex process and lacks theoretical conceptualisation especially in solid media, new measurements of transitions in heavier kaonic atoms from solid materials can expand the experimental database to advance and constrain cascade models. Future measurements of higher levels in intermediate-mass kaonic atoms could also help to investigate the contribution of multinucleon-absorption processes in the $\overline{\mathrm{K}}\mathrm{N}$ interaction [8], [134], [135]. Thus, measurements of transitions to both high and low n levels with solid targets such as selenium, zirconium, tantalum and lead have been proposed[142].

Lastly, a first look at the kaonic deuterium spectrum obtained with the SIDDHARTA-2 apparatus for an integrated luminosity of 29.8 pb^{-1} was presented. A possible fit function to describe the spectral shape was proposed. Given the accumulated statistics, no clear transition lines from the kaonic deuterium K-series were visible yet. According to a simulation performed on the detection significance of the $\mathrm{K}^{-}\mathrm{d}$ K_{α} transition, the observation of this line could not yet be expected with the collected integrated luminosity [137]. Therefore, the SIDDHARTA-2 collaboration is scheduled to continue their data acquisition with a deuterium target until an integrated luminosity of 800 pb^{-1} is reached. Several updates to the apparatus are in preparation, which were be presented in the previous section.

In conclusion, the first beam times with the SIDDHARTA-2 setup were completed successfully. The capability of all components of the apparatus to perform the challenging measurements of kaonic helium and deuterium in a high-background environment was evidenced in multiple facets, and highlighted in the high-precision results for kaonic helium-4 and the first ever measurement of transitions from intermediatie-mass kaonic atoms from solid materials. The long-awaited observation of the ground state shift and width of kaonic deuterium in the continued measurement of SIDDHARTA-2 will provide a missing piece in the understanding of the antikaon-nucleon interactions at threshold.

List of Figures

List of Tables

Abbreviations

ABS	Acrylonitrile Butadiene Styrene
ADC	Analogue-to-Digital-Converter
ASIC	Application Specific Integrated Circuit
CCD	Charge-Coupled Device
CFD	Constant Fraction Discriminator
CMOS	Complementary-Metal-Oxide Semiconductor
DAΦNE	Double Annular Φ-Factory for Nice Experiments
DAQ	Data Acquisition
DCR	Dark Count Rate
DEAR	DAΦNE Exotic Atom Research
EEPROM	Electrically Erasable Programmable Read-Only Memory
FWHM	Full Width Half Maximum
GEANT4	Geometry and Tracking 4
GUI	Graphical User Interface
HV	High Voltage
INFN	Istituto Nazionale di Fisica Nucleare
IP	Interaction Point
JFET	Junction-Gate Field-Effect Transistor
J-PARC	Japan Proton Accelerator Research Complex
KEK	High Energy Accelerator Research Organisation
KT	Kaon Trigger
LDD	Liquid Deuterium Density
LED	Light-Emitting Diode
LHeD	Liquid Helium Density
LINAC	Linear Accelerator

LNF	Laboratori Nazionali di Frascati
LV	Low Voltage
LVDS	Low Voltage Differential Signal
MC	Monte Carlo
MIP	Minimum Ionising Particle
MR	Main Ring
MWPC	Multiwire Proportional Chamber
NIM	Nuclear Instrumentation Module
NUV	Near-Ultraviolet
PET	Polyethylene Terephthalate
PMT	Photomultiplier Tube
QCD	Quantum Chromodynamics
QED	Quantum Electrodynamics
RF	Radio Frequency
SDD	Silicon Drift Detector
SFERA	SDD Front-End Readout ASIC
SIDDHARTA	Silicon Drift Detectors for Hadronic Atom Research by Timing Application
SIDDHARTINO	see SIDDHARTA; literal: "small SIDDHARTA"
SiPM	Silicon Photomultiplier
SMI	Stefan Meyer Institute for Subatomic Physics
SPAD	Single Photon Avalanche Diode
TDC	Time-to-Digital Converter
ToF	Time of Flight
ToT	Time over Threshold
TTL	Transistor-Transistor-Logic
USB	Universal Serial Bus

UHMWPE Ultra-high-molecular-weight Polyethylene

VME/VMEbus Versa Module Eurocard Bus

A Appendix - Electronics

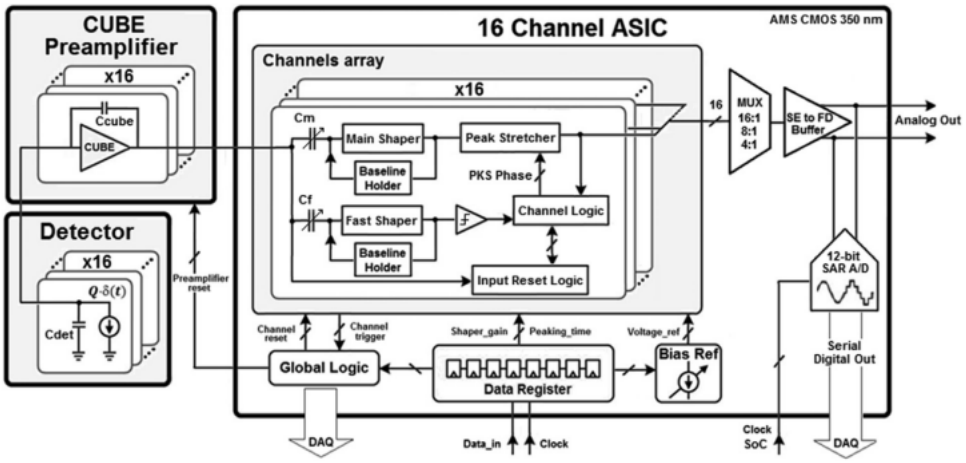

Figure 85: SDD read-out chain with SFERA block diagram. *From [82].*

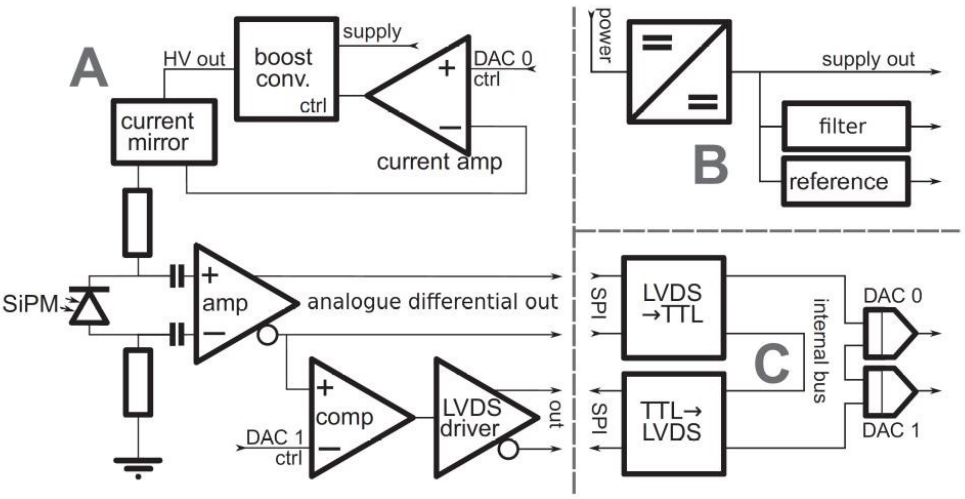

Figure 86: Block diagram for the constant current HV modules, providing the bias voltage for the Veto-2 SiPMs. *From [92].*

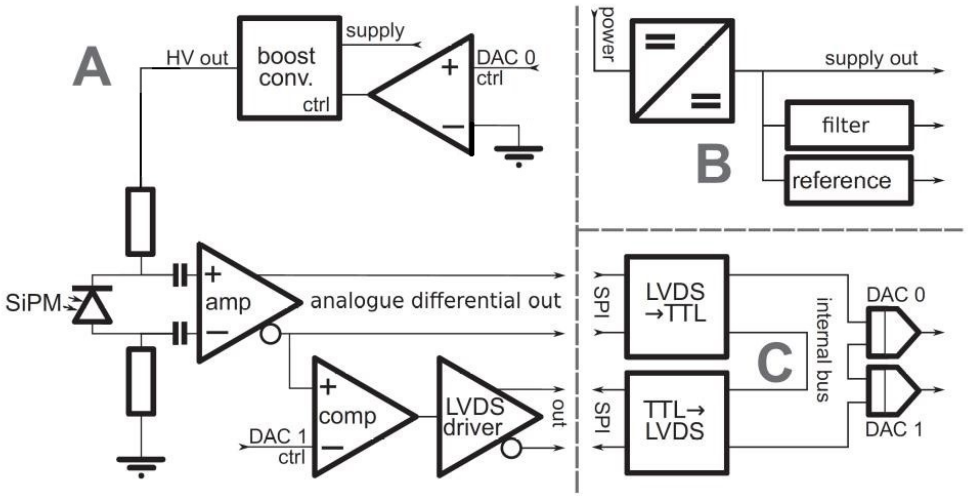

Figure 87: Modified HV modules, now providing a constant voltage output to the SiPMs, enabling their operation in spite of radiation damage. *[143], adapted from [92].*

B Appendix - Fit Functions

B.1 Kaonic Helium

The applied fit function for the kaonic helium-4 data consists of major components: the background function f_{back}, the kaonic helium-4 transition lines ($(3 \rightarrow 2)$ - $(10 \rightarrow 2)$ described by Voigtian functions and their tail components, and the remaining transitions from other kaonic atoms and fluorescence lines described by Gaussian functions and tail components. The free parameters of the fit function are listed as $p_i, i = 0, \ldots 41$. The background function has the following form:

$$f_{\text{back}}(E) = p_{0,\text{ const}} + p_{1,\text{ lin}} + p_{2,\text{ lin}}E + exp(p_{3,\text{ exp}} - p_{4,\text{ exp}} \cdot E). \tag{54}$$

The mean value $E_{\mu,\text{He}(3-2)}$ of the K^{-4}He $(3 \rightarrow 2)$ transition line is left as a free parameter. For the remaining K^{-4}He lines, the mean values are defined to be:

$$E_{\mu,\text{He}(i-2)} = E_{\text{ref,He}(i-2)} - E_{\text{ref,He}(3-2)} + E_{\mu,\text{He}(3-2)}, \tag{55}$$

with $i = 4, \ldots, 10$. $E_{\text{ref,He}(i-2)}$ denote the calculated reference values for the K^{-4}He transitions. The kaonic aluminium $(7 \rightarrow 6)$ mean value was left as a free parameter as well. For the remaining transition lines, the mean values are defined as

$$E_{\mu,\text{j}} = E_{\text{ref,j}} - p_9, \tag{56}$$

where p_9 denotes the global energy shift. j is a placeholder for the remaining transition lines listed in Tab. 15. The σs of the Gaussian and Voigtian functions are defined via Eq. 49:

$$\sigma_i = \epsilon \cdot \sqrt{\frac{E_{\mu,\text{j}}}{\epsilon} p_5 + p_6^2}, \tag{57}$$

with i describing all transition lines, ϵ being the ionisation energy in Si, p_5 the Fano factor, and p_6 the constant noise. The Voigtian function provided by the TMath library of ROOT was used, which is a convolution of a Gaussian

$$G(x) = \frac{1}{\sqrt{2\pi}\sigma} \cdot exp\left(\frac{(x - x_\mu)^2}{2\sigma^2}\right), \tag{58}$$

an a Lorentzian function

$$L(x) = \frac{1}{\pi} \cdot \frac{\frac{\Gamma}{2}}{(x - x_\mu)^2) + \frac{\Gamma^2}{4}}. \tag{59}$$

The Lorentzian linewidth Γ of the Voigtian functions was left free. The amplitudes of the $K^{-4}He$ $(3 \to 2)$ $A_{\mathrm{He}(3-2)}$, the $K^{-}C$ $(5 \to 4)$ $A_{\mathrm{KC}(5-4)}$, and the Ti $(2 \to 1)$ $A_{\mathrm{Ti}(2-1)}$ transitions are left free, while the amplitudes of the remaining transition lines ($A_{\mathrm{rel,i}}$) were related to those amplitudes. The definitions for the mean values and σ_{T} of the tail components for each transition line are analogous, with the mean values $E_{\mu,\mathrm{T,\,i}}$ shifted with respect to the main peaks by a global tail shift p_{27}:

$$E_{\mu,\mathrm{T,\,i}} = E_{\mu,\mathrm{i}} - p_{27} \tag{60}$$

$$\sigma_{\mathrm{T},i} = \epsilon \cdot \sqrt{\frac{E_{\mu,T,\mathrm{i}}}{\epsilon} p_5 + p_6^2}. \tag{61}$$

The tail components have a universal gain A_{T} and is normalised with the factor $n_{\mathrm{T},i}$, containing the universal tail slope β:

$$n_{\mathrm{T},i} = \frac{1}{2\beta\sigma_{T,i}} \cdot exp\left(\frac{1}{2\beta^2}\right). \tag{62}$$

The complete fit function $f_{\mathrm{He}}(E)$ for the $K^{-4}He$ data has the following form:

$$\begin{aligned}
&f_{\mathrm{He}}(E) = \\
&f_{\mathrm{back}}(E) + \\
&\quad + A_{\mathrm{He}(3-2)} \cdot \mathrm{Voigt}(E - E_{\mu,\mathrm{He}(3-2)}, \sigma_{\mathrm{He}(3-2)}, \Gamma, 4) + \\
&\quad + \sum_{i=4}^{10} A_{\mathrm{He}(3-2)} A_{\mathrm{rel,\,He}(i-2)} \cdot \mathrm{Voigt}(E - E_{\mu,\mathrm{He}(i-2)}, \sigma_{\mathrm{He}(i-2)}, \Gamma, 4) + \\
&\quad + A_{\mathrm{He}(3-2)} A_{\mathrm{T}} n_{\mathrm{T,\,He}(3-2)} \cdot \exp\left(\frac{E - E_{\mu,\mathrm{T,\,He}(3-2)}}{\sigma_{\mathrm{T,\,He}(3-2)}\beta}\right) \cdot \\
&\quad \cdot \mathrm{erfc}\left(\frac{E - E_{\mu,\mathrm{T,\,He}(3-2)}}{\sqrt{2}\sigma_{\mathrm{T,\,He}(3-2)}} + \frac{1}{\sqrt{2}\beta}\right) + \\
&\quad + \sum_{i=4}^{10} A_{\mathrm{He}(3-2)} A_{\mathrm{rel,\,He}(i-2)} A_{\mathrm{T}} n_{\mathrm{T,\,He}(i-2)} \cdot \exp\left(\frac{E - E_{\mu,\mathrm{T,\,He}(i-2)}}{\sigma_{\mathrm{T,\,He}(i-2)}\beta}\right) \cdot \\
&\quad \cdot \mathrm{erfc}\left(\frac{E - E_{\mu,\mathrm{T,\,He}(i-2)}}{\sqrt{2}\sigma_{\mathrm{T,\,He}(i-2)}} + \frac{1}{\sqrt{2}\beta}\right) + \\
&\quad + A_{\mathrm{KC}(5-4)} \cdot \exp\left(-\frac{(E - E_{\mu,\mathrm{KC}(5-4)})^2}{2\sigma_{\mathrm{KC}(5-4)}}\right) + \\
&\quad + A_{\mathrm{KC}(5-4)} A_{\mathrm{rel,\,KC}(7-5)} \cdot \exp\left(-\frac{(E - E_{\mu,\mathrm{KC}(7-5)})^2}{2\sigma_{\mathrm{KC}(7-5)}}\right) + \\
&\quad + A_{\mathrm{KC}(5-4)} A_{\mathrm{rel,\,KC}(6-5)} \cdot \exp\left(-\frac{(E - E_{\mu,\mathrm{KC}(6-5)})^2}{2\sigma_{\mathrm{KC}(6-5)}}\right) +
\end{aligned}$$

$$
\begin{aligned}
&+A_{\mathrm{KC}(5-4)}A_{\text{rel, KC}(6-4)}\cdot\exp\left(-\frac{(E-E_{\mu,\mathrm{KC}(6-4)})^2}{2\sigma_{\mathrm{KC}(6-4)}}\right)+\\
&+A_{\mathrm{KC}(5-4)}A_{\text{rel, KN}(5-4)}\cdot\exp\left(-\frac{(E-E_{\mu,\mathrm{KN}(5-4)})^2}{2\sigma_{\mathrm{KN}(5-4)}}\right)+\\
&+A_{\mathrm{KC}(5-4)}A_{\text{rel, KN}(5-4)}A_{\text{rel, KN}(6-5)}\cdot\exp\left(-\frac{(E-E_{\mu,\mathrm{KN}(6-5)})^2}{2\sigma_{\mathrm{KN}(6-5)}}\right)+\\
&+A_{\mathrm{KC}(5-4)}A_{\text{rel, KN}(7-6)}\cdot\exp\left(-\frac{(E-E_{\mu,\mathrm{KN}(7-6)})^2}{2\sigma_{\mathrm{KN}(7-6)}}\right)+\\
&+A_{\mathrm{KC}(5-4)}A_{\text{rel, KO}(6-5)}\cdot\exp\left(-\frac{(E-E_{\mu,\mathrm{KO}(6-5)})^2}{2\sigma_{\mathrm{KO}(6-5)}}\right)+\\
&+A_{\mathrm{KC}(5-4)}A_{\text{rel, KO}(6-5)}A_{\text{rel, KO}(7-6)}\cdot\exp\left(-\frac{(E-E_{\mu,\mathrm{KO}(6-5)})^2}{2\sigma_{\mathrm{KO}(6-5)}}\right)+\\
&+A_{\mathrm{KC}(5-4)}A_{\text{rel, KAl}(7-6)}\cdot\exp\left(-\frac{(E-E_{\mu,\mathrm{KAl}(7-6)})^2}{2\sigma_{\mathrm{KAl}(7-6)}}\right)+\\
&+A_{\mathrm{KC}(5-4)}A_{\text{rel, KAl}(8-7)}\cdot\exp\left(-\frac{(E-E_{\mu,\mathrm{KAl}(8-7)})^2}{2\sigma_{\mathrm{KAl}(8-7)}}\right)+\\
&+A_{\mathrm{KC}(5-4)}A_{\text{rel, KAl}(8-7)}A_{\text{rel, KAl}(9-8)}\cdot\exp\left(-\frac{(E-E_{\mu,\mathrm{KAl}(9-8)})^2}{2\sigma_{\mathrm{KAl}(9-8)}}\right)+\\
&+A_{\mathrm{KC}(5-4)}A_{\text{rel, KTi}(11-10)}\cdot\exp\left(-\frac{(E-E_{\mu,\mathrm{KTi}(11-10)})^2}{2\sigma_{\mathrm{KTi}(11-10)}}\right)+\\
&+A_{\mathrm{KC}(5-4)}A_{\text{rel, KTi}(11-10)}A_{\text{rel, KTi}(12-11)}\cdot\exp\left(-\frac{(E-E_{\mu,\mathrm{KTi}(11-10)})^2}{2\sigma_{\mathrm{KTi}(11-10)}}\right)+\\
&+A_{\mathrm{Ti}(2-1),1}\cdot\exp\left(-\frac{(E-E_{\mu,\mathrm{Ti}(2-1),1})^2}{2\sigma_{\mathrm{Ti}(2-1),1}}\right)+\\
&+A_{\mathrm{Ti}(2-1),1}A_{\text{rel, Ti}(2-1),2}\cdot\exp\left(-\frac{(E-E_{\mu,\mathrm{Ti}(2-1),2})^2}{2\sigma_{\mathrm{Ti}(2-1),2}}\right)+\\
&+A_{\mathrm{Ti}(2-1),1}A_{\text{rel, Ti}(3-1),1}\cdot\exp\left(-\frac{(E-E_{\mu,\mathrm{Ti}(3-1),1})^2}{2\sigma_{\mathrm{Ti}(3-1),1}}\right)+\\
&+A_{\mathrm{KC}(5-4)}A_{\mathrm{T}}n_{\text{T, KC}(5-4)}\cdot\exp\left(\frac{E-E_{\mu,\text{T, KC}(5-4)}}{\sigma_{\text{T, KC}(5-4)}\beta}\right)\cdot\\
&\cdot\mathrm{erfc}\left(\frac{E-E_{\mu,\text{T, KC}(5-4)}}{\sqrt{2}\sigma_{\text{T, KC}(5-4)}}+\frac{1}{\sqrt{2}\beta}\right)+\\
&+A_{\mathrm{KC}(5-4)}A_{\text{rel, KC}(7-5)}A_{\mathrm{T}}n_{\text{T, KC}(7-5)}\cdot\exp\left(\frac{E-E_{\mu,\text{T, KC}(7-5)}}{\sigma_{\text{T, KC}(7-5)}\beta}\right)\cdot\\
&\cdot\mathrm{erfc}\left(\frac{E-E_{\mu,\text{T, KC}(7-5)}}{\sqrt{2}\sigma_{\text{T, KC}(7-5)}}+\frac{1}{\sqrt{2}\beta}\right)+
\end{aligned}
$$

$$+A_{\mathrm{KC}(5-4)}A_{\mathrm{rel,\ KC}(6-5)}A_{\mathrm{T}}n_{\mathrm{T,\ KC}(6-5)}\cdot\exp\left(\frac{E-E_{\mu,\mathrm{T,\ KC}(6-5)}}{\sigma_{\mathrm{T,\ KC}(6-5)}\beta}\right)\cdot$$
$$\cdot\mathrm{erfc}\left(\frac{E-E_{\mu,\mathrm{T,\ KC}(6-5)}}{\sqrt{2}\sigma_{\mathrm{T,\ KC}(6-5)}}+\frac{1}{\sqrt{2}\beta}\right)+$$
$$+A_{\mathrm{KC}(5-4)}A_{\mathrm{rel,\ KC}(6-4)}A_{\mathrm{T}}n_{\mathrm{T,\ KC}(6-4)}\cdot\exp\left(\frac{E-E_{\mu,\mathrm{T,\ KC}(6-4)}}{\sigma_{\mathrm{T,\ KC}(6-4)}\beta}\right)\cdot$$
$$\cdot\mathrm{erfc}\left(\frac{E-E_{\mu,\mathrm{T,\ KC}(6-4)}}{\sqrt{2}\sigma_{\mathrm{T,\ KC}(6-4)}}+\frac{1}{\sqrt{2}\beta}\right)+$$
$$+A_{\mathrm{KC}(5-4)}A_{\mathrm{rel,\ KN}(5-4)}A_{\mathrm{T}}n_{\mathrm{T,\ KN}(5-4)}\cdot\exp\left(\frac{E-E_{\mu,\mathrm{T,\ KN}(5-4)}}{\sigma_{\mathrm{T,\ KN}(5-4)}\beta}\right)\cdot$$
$$\cdot\mathrm{erfc}\left(\frac{E-E_{\mu,\mathrm{T,\ KN}(5-4)}}{\sqrt{2}\sigma_{\mathrm{T,\ KN}(5-4)}}+\frac{1}{\sqrt{2}\beta}\right)+$$
$$+A_{\mathrm{KC}(5-4)}A_{\mathrm{rel,\ KN}(5-4)}A_{\mathrm{rel,\ KN}(6-5)}A_{\mathrm{T}}n_{\mathrm{T,\ KN}(6-5)}\cdot$$
$$\cdot\exp\left(\frac{E-E_{\mu,\mathrm{T,\ KN}(6-5)}}{\sigma_{\mathrm{T,\ KN}(6-5)}\beta}\right)\cdot\mathrm{erfc}\left(\frac{E-E_{\mu,\mathrm{T,\ KN}(6-5)}}{\sqrt{2}\sigma_{\mathrm{T,\ KN}(6-5)}}+\frac{1}{\sqrt{2}\beta}\right)+$$
$$+A_{\mathrm{KC}(5-4)}A_{\mathrm{rel,\ KN}(7-6)}A_{\mathrm{T}}n_{\mathrm{T,\ KN}(7-6)}\cdot\exp\left(\frac{E-E_{\mu,\mathrm{T,\ KN}(7-6)}}{\sigma_{\mathrm{T,\ KN}(7-6)}\beta}\right)\cdot$$
$$\cdot\mathrm{erfc}\left(\frac{E-E_{\mu,\mathrm{T,\ KN}(7-6)}}{\sqrt{2}\sigma_{\mathrm{T,\ KN}(7-6)}}+\frac{1}{\sqrt{2}\beta}\right)+$$
$$+A_{\mathrm{KC}(5-4)}A_{\mathrm{rel,\ KO}(6-5)}A_{\mathrm{T}}n_{\mathrm{T,\ KO}(6-5)}\cdot\exp\left(\frac{E-E_{\mu,\mathrm{T,\ KO}(6-5)}}{\sigma_{\mathrm{T,\ KO}(6-5)}\beta}\right)\cdot$$
$$\cdot\mathrm{erfc}\left(\frac{E-E_{\mu,\mathrm{T,\ KO}(6-5)}}{\sqrt{2}\sigma_{\mathrm{T,\ KO}(6-5)}}+\frac{1}{\sqrt{2}\beta}\right)+$$
$$+A_{\mathrm{KC}(5-4)}A_{\mathrm{rel,\ KO}(6-5)}A_{\mathrm{rel,\ KO}(7-6)}A_{\mathrm{T}}n_{\mathrm{T,\ KO}(7-6)}\cdot$$
$$\cdot\exp\left(\frac{E-E_{\mu,\mathrm{T,\ KO}(7-6)}}{\sigma_{\mathrm{T,\ KO}(7-6)}\beta}\right)\cdot\mathrm{erfc}\left(\frac{E-E_{\mu,\mathrm{T,\ KO}(7-6)}}{\sqrt{2}\sigma_{\mathrm{T,\ KO}(7-6)}}+\frac{1}{\sqrt{2}\beta}\right)+$$
$$+A_{\mathrm{KC}(5-4)}A_{\mathrm{rel,\ KAl}(7-6)}A_{\mathrm{T}}n_{\mathrm{T,\ KAl}(7-6)}\cdot\exp\left(\frac{E-E_{\mu,\mathrm{T,\ KAl}(7-6)}}{\sigma_{\mathrm{T,\ KAl}(7-6)}\beta}\right)\cdot$$
$$\cdot\mathrm{erfc}\left(\frac{E-E_{\mu,\mathrm{T,\ KAl}(7-6)}}{\sqrt{2}\sigma_{\mathrm{T,\ KAl}(7-6)}}+\frac{1}{\sqrt{2}\beta}\right)+$$
$$+A_{\mathrm{KC}(5-4)}A_{\mathrm{rel,\ KAl}(8-7)}A_{\mathrm{T}}n_{\mathrm{T,\ KAl}(8-7)}\cdot\exp\left(\frac{E-E_{\mu,\mathrm{T,\ KAl}(8-7)}}{\sigma_{\mathrm{T,\ KAl}(8-7)}\beta}\right)\cdot$$
$$\cdot\mathrm{erfc}\left(\frac{E-E_{\mu,\mathrm{T,\ KAl}(8-7)}}{\sqrt{2}\sigma_{\mathrm{T,\ KAl}(8-7)}}+\frac{1}{\sqrt{2}\beta}\right)+$$
$$+A_{\mathrm{KC}(5-4)}A_{\mathrm{rel,\ KAl}(8-7)}A_{\mathrm{rel,\ KAl}(9-8)}A_{\mathrm{T}}n_{\mathrm{T,\ KAl}(9-8)}\cdot$$

$$
\begin{aligned}
&\cdot\exp\left(\frac{E-E_{\mu,\mathrm{T,\ KAl(9-8)}}}{\sigma_{\mathrm{T,\ KAl(9-8)}}\beta}\right)\cdot\mathrm{erfc}\left(\frac{E-E_{\mu,\mathrm{T,\ KAl(9-8)}}}{\sqrt{2}\sigma_{\mathrm{T,\ KAl(9-8)}}}+\frac{1}{\sqrt{2}\beta}\right)+\\
&+A_{\mathrm{rel,\ Ti(2-1),1}}A_{\mathrm{T}}n_{\mathrm{T,\ Ti(2-1),1}}\cdot\exp\left(\frac{E-E_{\mu,\mathrm{T,\ Ti(2-1),1}}}{\sigma_{\mathrm{T,\ Ti(2-1),1}}\beta}\right)\cdot\\
&\cdot\mathrm{erfc}\left(\frac{E-E_{\mu,\mathrm{T,\ Ti(2-1),1}}}{\sqrt{2}\sigma_{\mathrm{T,\ Ti(2-1),1}}}+\frac{1}{\sqrt{2}\beta}\right)+\\
&+A_{\mathrm{rel,\ Ti(2-1),1}}A_{\mathrm{rel,\ Ti(2-1),2}}A_{\mathrm{T}}n_{\mathrm{T,\ Ti(2-1),2}}\cdot\exp\left(\frac{E-E_{\mu,\mathrm{T,\ Ti(2-1),2}}}{\sigma_{\mathrm{T,\ Ti(2-1),2}}\beta}\right)\cdot\\
&\cdot\mathrm{erfc}\left(\frac{E-E_{\mu,\mathrm{T,\ Ti(2-1),2}}}{\sqrt{2}\sigma_{\mathrm{T,\ Ti(2-1),2}}}+\frac{1}{\sqrt{2}\beta}\right)+\\
&+A_{\mathrm{rel,\ Ti(2-1),1}}A_{\mathrm{rel,\ Ti(3-1),1}}A_{\mathrm{T}}n_{\mathrm{T,\ Ti(3-1),1}}\cdot\exp\left(\frac{E-E_{\mu,\mathrm{T,\ Ti(3-1),1}}}{\sigma_{\mathrm{T,\ Ti(3-1),1}}\beta}\right)\cdot\\
&\cdot\mathrm{erfc}\left(\frac{E-E_{\mu,\mathrm{T,\ Ti(3-1),1}}}{\sqrt{2}\sigma_{\mathrm{T,\ Ti(3-1),1}}}+\frac{1}{\sqrt{2}\beta}\right). \qquad (63)
\end{aligned}
$$

B.2 Kaonic Deuterium

The fit function for the kaonic deuterium data was derived from the kaonic helium-4 fit function. The background function is the same as for the kaonic helium-4 data. The mean values and σ of the main peaks (both Gaussian and Voigtian) are defined analogously to the K^{-4}He function. Like before, the kaonic deuterium ($2\rightarrow1$), kaonic carbon ($5\rightarrow4$) and Ti ($2\rightarrow1$) transition mean values and amplitudes are left free. The amplitudes of the remaining transition lines are again defined as relative amplitudes to those transition amplitudes. The tail components are of the same form as for f_{He}. The complete fit function f_{D} for the kaonic deuterium data is defined as

$$
\begin{aligned}
&f_{\mathrm{D}}(E)=\\
&f_{\mathrm{back}}(E)+\\
&\quad+A_{\mathrm{D(2-1)}}\cdot\mathrm{Voigt}(E-E_{\mu,\mathrm{D(2-1)}},\sigma_{\mathrm{D(2-1)}},\Gamma,4)+\\
&\quad+\sum_{i=3}^{8}A_{\mathrm{D(2-1)}}A_{\mathrm{rel,\ D}(i-1)}\cdot\mathrm{Voigt}(E-E_{\mu,\mathrm{D}(i-1)},\sigma_{\mathrm{D}(i-1)},\Gamma,4)+\\
&\quad+A_{\mathrm{D(2-1)}}A_{\mathrm{T}}n_{\mathrm{T,\ D(2-1)}}\cdot\exp\left(\frac{E-E_{\mu,\mathrm{T,\ D(2-1)}}}{\sigma_{\mathrm{T,\ D(2-1)}}\beta}\right)\cdot\\
&\quad\cdot\mathrm{erfc}\left(\frac{E-E_{\mu,\mathrm{T,\ D(2-1)}}}{\sqrt{2}\sigma_{\mathrm{T,\ D(2-1)}}}+\frac{1}{\sqrt{2}\beta}\right)+
\end{aligned}
$$

$$+\sum_{i=3}^{8} A_{\mathrm{D}(2-1)} A_{\mathrm{rel,\ D}(i-1)} A_{\mathrm{T}} n_{\mathrm{T,\ D}(i-1)} \cdot \exp\left(\frac{E - E_{\mu,\mathrm{T,\ D}(i-1)}}{\sigma_{\mathrm{T,\ D}(i-1)}\beta}\right) \cdot$$

$$\cdot \mathrm{erfc}\left(\frac{E - E_{\mu,\mathrm{T,\ D}(i-1)}}{\sqrt{2}\sigma_{\mathrm{T,\ D}(i-1)}} + \frac{1}{\sqrt{2}\beta}\right) +$$

$$+A_{\mathrm{KC}(5-4)} \cdot exp\left(-\frac{(E - E_{\mu,\mathrm{KC}(5-4)})^2}{2\sigma_{\mathrm{KC}(5-4)}}\right) +$$

$$+A_{\mathrm{KC}(5-4)} A_{\mathrm{rel,\ KC}(7-5)} \cdot \exp\left(-\frac{(E - E_{\mu,\mathrm{KC}(7-5)})^2}{2\sigma_{\mathrm{KC}(7-5)}}\right) +$$

$$+A_{\mathrm{KC}(5-4)} A_{\mathrm{rel,\ KC}(6-5)} \cdot \exp\left(-\frac{(E - E_{\mu,\mathrm{KC}(6-5)})^2}{2\sigma_{\mathrm{KC}(6-5)}}\right) +$$

$$+A_{\mathrm{KC}(5-4)} A_{\mathrm{rel,\ KN}(6-5)} \cdot \exp\left(-\frac{(E - E_{\mu,\mathrm{KN}(6-5)})^2}{2\sigma_{\mathrm{KN}(6-5)}}\right) +$$

$$+A_{\mathrm{KC}(5-4)} A_{\mathrm{rel,\ KN}(7-6)} \cdot \exp\left(-\frac{(E - E_{\mu,\mathrm{KN}(7-6)})^2}{2\sigma_{\mathrm{KN}(7-6)}}\right) +$$

$$+A_{\mathrm{KC}(5-4)} A_{\mathrm{rel,\ KO}(6-5)} \cdot \exp\left(-\frac{(E - E_{\mu,\mathrm{KO}(6-5)})^2}{2\sigma_{\mathrm{KO}(6-5)}}\right) +$$

$$+A_{\mathrm{KC}(5-4)} A_{\mathrm{rel,\ KO}(6-5)} A_{\mathrm{rel,\ KO}(7-6)} \cdot \exp\left(-\frac{(E - E_{\mu,\mathrm{KO}(6-5)})^2}{2\sigma_{\mathrm{KO}(6-5)}}\right) +$$

$$+A_{\mathrm{KC}(5-4)} A_{\mathrm{rel,\ KAl}(7-6)} \cdot \exp\left(-\frac{(E - E_{\mu,\mathrm{KAl}(7-6)})^2}{2\sigma_{\mathrm{KAl}(7-6)}}\right) +$$

$$+A_{\mathrm{KC}(5-4)} A_{\mathrm{rel,\ KAl}(8-7)} \cdot \exp\left(-\frac{(E - E_{\mu,\mathrm{KAl}(8-7)})^2}{2\sigma_{\mathrm{KAl}(8-7)}}\right) +$$

$$+A_{\mathrm{KC}(5-4)} A_{\mathrm{rel,\ KAl}(8-7)} A_{\mathrm{rel,\ KAl}(9-8)} \cdot \exp\left(-\frac{(E - E_{\mu,\mathrm{KAl}(9-8)})^2}{2\sigma_{\mathrm{KAl}(9-8)}}\right) +$$

$$+A_{\mathrm{KC}(5-4)} A_{\mathrm{rel,\ KTi}(11-10)} \cdot \exp\left(-\frac{(E - E_{\mu,\mathrm{KTi}(11-10)})^2}{2\sigma_{\mathrm{KTi}(11-10)}}\right) +$$

$$+A_{\mathrm{KC}(5-4)} A_{\mathrm{rel,\ KTi}(11-10)} A_{\mathrm{rel,\ KTi}(12-11)} \cdot \exp\left(-\frac{(E - E_{\mu,\mathrm{KTi}(11-10)})^2}{2\sigma_{\mathrm{KTi}(11-10)}}\right) +$$

$$+A_{\mathrm{KC}(5-4)} A_{\mathrm{rel,\ KTi}(11-10)} A_{\mathrm{rel,\ KTi}(13-12)} \cdot \exp\left(-\frac{(E - E_{\mu,\mathrm{KTi}(13-12)})^2}{2\sigma_{\mathrm{KTi}(13-12)}}\right) +$$

$$+A_{\mathrm{Ti}(2-1),1} \cdot exp\left(-\frac{(E - E_{\mu,\mathrm{Ti}(2-1),1})^2}{2\sigma_{\mathrm{Ti}(2-1),1}}\right) +$$

$$+A_{\mathrm{Ti}(2-1),1} A_{\mathrm{rel,\ Ti}(2-1),2} \cdot \exp\left(-\frac{(E - E_{\mu,\mathrm{Ti}(2-1),2})^2}{2\sigma_{\mathrm{Ti}(2-1),2}}\right) +$$

$$+A_{\mathrm{Ti}(2-1),1} A_{\mathrm{rel,\ Ti}(3-1),1} \cdot \exp\left(-\frac{(E - E_{\mu,\mathrm{Ti}(3-1),1})^2}{2\sigma_{\mathrm{Ti}(3-1),1}}\right) +$$

$$+A_{\mathrm{KC(5-4)}}A_{\mathrm{T}}n_{\mathrm{T,\ KC(5-4)}}\cdot\exp\left(\frac{E-E_{\mu,\mathrm{T,\ KC(5-4)}}}{\sigma_{\mathrm{T,\ KC(5-4)}}\beta}\right)\cdot$$
$$\cdot\mathrm{erfc}\left(\frac{E-E_{\mu,\mathrm{T,\ KC(5-4)}}}{\sqrt{2}\sigma_{\mathrm{T,\ KC(5-4)}}}+\frac{1}{\sqrt{2}\beta}\right)+$$
$$+A_{\mathrm{KC(5-4)}}A_{\mathrm{rel,\ KC(7-5)}}A_{\mathrm{T}}n_{\mathrm{T,\ KC(7-5)}}\cdot\exp\left(\frac{E-E_{\mu,\mathrm{T,\ KC(7-5)}}}{\sigma_{\mathrm{T,\ KC(7-5)}}\beta}\right)\cdot$$
$$\cdot\mathrm{erfc}\left(\frac{E-E_{\mu,\mathrm{T,\ KC(7-5)}}}{\sqrt{2}\sigma_{\mathrm{T,\ KC(7-5)}}}+\frac{1}{\sqrt{2}\beta}\right)+$$
$$+A_{\mathrm{KC(5-4)}}A_{\mathrm{rel,\ KC(6-5)}}A_{\mathrm{T}}n_{\mathrm{T,\ KC(6-5)}}\cdot\exp\left(\frac{E-E_{\mu,\mathrm{T,\ KC(6-5)}}}{\sigma_{\mathrm{T,\ KC(6-5)}}\beta}\right)\cdot$$
$$\cdot\mathrm{erfc}\left(\frac{E-E_{\mu,\mathrm{T,\ KC(6-5)}}}{\sqrt{2}\sigma_{\mathrm{T,\ KC(6-5)}}}+\frac{1}{\sqrt{2}\beta}\right)+$$
$$+A_{\mathrm{KC(5-4)}}A_{\mathrm{rel,\ KN(6-5)}}A_{\mathrm{T}}n_{\mathrm{T,\ KN(6-5)}}\cdot\exp\left(\frac{E-E_{\mu,\mathrm{T,\ KN(6-5)}}}{\sigma_{\mathrm{T,\ KN(6-5)}}\beta}\right)\cdot$$
$$\cdot\mathrm{erfc}\left(\frac{E-E_{\mu,\mathrm{T,\ KN(6-5)}}}{\sqrt{2}\sigma_{\mathrm{T,\ KN(6-5)}}}+\frac{1}{\sqrt{2}\beta}\right)+$$
$$+A_{\mathrm{KC(5-4)}}A_{\mathrm{rel,\ KN(7-6)}}A_{\mathrm{T}}n_{\mathrm{T,\ KN(7-6)}}\cdot\exp\left(\frac{E-E_{\mu,\mathrm{T,\ KN(7-6)}}}{\sigma_{\mathrm{T,\ KN(7-6)}}\beta}\right)\cdot$$
$$\cdot\mathrm{erfc}\left(\frac{E-E_{\mu,\mathrm{T,\ KN(7-6)}}}{\sqrt{2}\sigma_{\mathrm{T,\ KN(7-6)}}}+\frac{1}{\sqrt{2}\beta}\right)+$$
$$+A_{\mathrm{KC(5-4)}}A_{\mathrm{rel,\ KO(6-5)}}A_{\mathrm{T}}n_{\mathrm{T,\ KO(6-5)}}\cdot\exp\left(\frac{E-E_{\mu,\mathrm{T,\ KO(6-5)}}}{\sigma_{\mathrm{T,\ KO(6-5)}}\beta}\right)\cdot$$
$$\cdot\mathrm{erfc}\left(\frac{E-E_{\mu,\mathrm{T,\ KO(6-5)}}}{\sqrt{2}\sigma_{\mathrm{T,\ KO(6-5)}}}+\frac{1}{\sqrt{2}\beta}\right)+$$
$$+A_{\mathrm{KC(5-4)}}A_{\mathrm{rel,\ KO(6-5)}}A_{\mathrm{rel,\ KO(7-6)}}A_{\mathrm{T}}n_{\mathrm{T,\ KO(7-6)}}\cdot$$
$$\cdot\exp\left(\frac{E-E_{\mu,\mathrm{T,\ KO(7-6)}}}{\sigma_{\mathrm{T,\ KO(7-6)}}\beta}\right)\cdot\mathrm{erfc}\left(\frac{E-E_{\mu,\mathrm{T,\ KO(7-6)}}}{\sqrt{2}\sigma_{\mathrm{T,\ KO(7-6)}}}+\frac{1}{\sqrt{2}\beta}\right)+$$
$$+A_{\mathrm{KC(5-4)}}A_{\mathrm{rel,\ KAl(7-6)}}A_{\mathrm{T}}n_{\mathrm{T,\ KAl(7-6)}}\cdot\exp\left(\frac{E-E_{\mu,\mathrm{T,\ KAl(7-6)}}}{\sigma_{\mathrm{T,\ KAl(7-6)}}\beta}\right)\cdot$$
$$\cdot\mathrm{erfc}\left(\frac{E-E_{\mu,\mathrm{T,\ KAl(7-6)}}}{\sqrt{2}\sigma_{\mathrm{T,\ KAl(7-6)}}}+\frac{1}{\sqrt{2}\beta}\right)+$$
$$+A_{\mathrm{KC(5-4)}}A_{\mathrm{rel,\ KAl(8-7)}}A_{\mathrm{T}}n_{\mathrm{T,\ KAl(8-7)}}\cdot\exp\left(\frac{E-E_{\mu,\mathrm{T,\ KAl(8-7)}}}{\sigma_{\mathrm{T,\ KAl(8-7)}}\beta}\right)\cdot$$
$$\cdot\mathrm{erfc}\left(\frac{E-E_{\mu,\mathrm{T,\ KAl(8-7)}}}{\sqrt{2}\sigma_{\mathrm{T,\ KAl(8-7)}}}+\frac{1}{\sqrt{2}\beta}\right)+$$

$$
\begin{aligned}
&+A_{\mathrm{KC(5-4)}}A_{\mathrm{rel,\ KAl(8-7)}}A_{\mathrm{rel,\ KAl(9-8)}}A_{\mathrm{T}}n_{\mathrm{T,\ KAl(9-8)}}\cdot \\
&\cdot\exp\left(\frac{E-E_{\mu,\mathrm{T,\ KAl(9-8)}}}{\sigma_{\mathrm{T,\ KAl(9-8)}}\beta}\right)\cdot\operatorname{erfc}\left(\frac{E-E_{\mu,\mathrm{T,\ KAl(9-8)}}}{\sqrt{2}\sigma_{\mathrm{T,\ KAl(9-8)}}}+\frac{1}{\sqrt{2}\beta}\right)+ \\
&+A_{\mathrm{rel,\ Ti(2-1),1}}A_{\mathrm{T}}n_{\mathrm{T,\ Ti(2-1),1}}\cdot\exp\left(\frac{E-E_{\mu,\mathrm{T,\ Ti(2-1),1}}}{\sigma_{\mathrm{T,\ Ti(2-1),1}}\beta}\right)\cdot \\
&\cdot\operatorname{erfc}\left(\frac{E-E_{\mu,\mathrm{T,\ Ti(2-1),1}}}{\sqrt{2}\sigma_{\mathrm{T,\ Ti(2-1),1}}}+\frac{1}{\sqrt{2}\beta}\right)+ \\
&+A_{\mathrm{rel,\ Ti(2-1),1}}A_{\mathrm{rel,\ Ti(2-1),2}}A_{\mathrm{T}}n_{\mathrm{T,\ Ti(2-1),2}}\cdot\exp\left(\frac{E-E_{\mu,\mathrm{T,\ Ti(2-1),2}}}{\sigma_{\mathrm{T,\ Ti(2-1),2}}\beta}\right)\cdot \\
&\cdot\operatorname{erfc}\left(\frac{E-E_{\mu,\mathrm{T,\ Ti(2-1),2}}}{\sqrt{2}\sigma_{\mathrm{T,\ Ti(2-1),2}}}+\frac{1}{\sqrt{2}\beta}\right)+ \\
&+A_{\mathrm{rel,\ Ti(2-1),1}}A_{\mathrm{rel,\ Ti(3-1),1}}A_{\mathrm{T}}n_{\mathrm{T,\ Ti(3-1),1}}\cdot\exp\left(\frac{E-E_{\mu,\mathrm{T,\ Ti(3-1),1}}}{\sigma_{\mathrm{T,\ Ti(3-1),1}}\beta}\right)\cdot \\
&\cdot\operatorname{erfc}\left(\frac{E-E_{\mu,\mathrm{T,\ Ti(3-1),1}}}{\sqrt{2}\sigma_{\mathrm{T,\ Ti(3-1),1}}}+\frac{1}{\sqrt{2}\beta}\right). \qquad (64)
\end{aligned}
$$

References

[1] Bazzi, M. et al. (SIDDHARTA collaboration), "Kaonic hydrogen X-ray measurement in SIDDHARTA", *Nucl. Phys. A*, vol. 881, pp. 88–97, 2012. DOI: 10.1016/j.nuclphysa.2011.12.008.

[2] Bazzi, M. et al. (SIDDHARTA collaboration), "Kaonic helium-4 X-ray measurement in SIDDHARTA", *Phys. Lett. B*, vol. 681, pp. 310–314, 2009. DOI: 10.1016/j.physletb.2009.10.052.

[3] Bazzi, M. et al. (SIDDHARTA collaboration), "Measurements of the strong-interaction widths of the kaonic ^{3}He and ^{4}He $2p$ levels", *Phys. Lett. B*, vol. 714, pp. 40–43, 2012. DOI: 10.1016/j.physletb.2012.06.071.

[4] Hashimoto, T. et al. (J-PARC E62 Collaboration), "Measurements of Strong-Interaction Effects in Kaonic Helium Isotopes at Sub-eV Precision with X-ray Microcalorimeters", *Phys. Rev. Lett.*, vol. 128, p. 112 503, 2022. DOI: 10.1103/PhysRevLett.128.112503.

[5] Workman, R.L. et al. (Particle Data Group), *Prog. Theor. Exp. Phys.*, 2022, 083C01 (2022).

[6] Gotta, D., "Precision spectroscopy of light exotic atoms", *Prog. Part. Nucl. Phys.*, vol. 52, pp. 133–195, 2004. DOI: 10.1016/j.ppnp.2003.09.003.

[7] Bethe, H.A., and Salpeter, E.E. Springer Berlin, 1957.

[8] Friedman, E., Gal, A., and Batty, C. J., "Density dependent K^- nuclear optical potentials from kaonic atoms", *Nucl. Phys. A*, vol. 579, pp. 518–538, 1994. DOI: 10.1016/0375-9474(94)90921-0.

[9] Kaiser, N., Siegel, P.B., and Weise, W., "Chiral dynamics and the low-energy kaon-nucleon interaction", *Nucl. Phys. A*, vol. 594, pp. 325–345, 1995. DOI: 10.1016/0375-9474(95)00362-5.

[10] Seki, R. and Wiegand, C.E., "Kaonic and other exotic atoms", *Annu. Rev. Nucl. Sci.*, vol. 25, pp. 241–281, 1975. DOI: 10.1146/annurev.ns.25.120175.001325.

[11] Jido, D. et al., "Chiral dynamics of the two $\Lambda(1405)$ states", *Nucl. Phys. A*, vol. 725, pp. 181–200, 2003. DOI: 10.1016/S0375-9474(03)01598-7.

[12] Hyodo, T. and Weise, W., "Effective $\bar{K}N$ interaction based on chiral SU(3) dynamics", *Phys. Rev. C*, vol. 77, p. 035 204, 2008. DOI: 10.1103/PhysRevC.77.035204.

[13] Hyodo, T., and Jido, D., "The nature of the $\Lambda(1405)$ resonance in chiral dynamics", *Prog. Part. Nucl. Phys.*, vol. 67, pp. 55–98, 2012. DOI: 10.1016/j.ppnp.2011.07.002.

[14] Ohnishi, S. et al., "Structure of the $\Lambda(1405)$ and the $K^- d \to \pi\Sigma n$ reaction", *Phys. Rev. C*, vol. 93, p. 025 207, 2016. DOI: 10.1103/PhysRevC.93.025207.

[15] Aikawa, S. et al., "Pole position of $\Lambda(1405)$ measured in d(K^-,n)$\pi\Sigma$ reactions", *Phys. Lett. B*, vol. 837, p. 137 637, 2023. DOI: 10.1016/j.physletb.2022.137637.

[16] Gasser, J., Sainio, M.E., and Švarc, A., "Nucleons with chiral loops", *Nucl. Phys. B*, vol. 307, p. 779, 1988. DOI: 10.1016/0550-3213(88)90108-3.

[17] Batty, C.J., "Optical-model analysis of exotic atom data: (I). Kaonic atoms", *Nucl. Phys. A*, vol. 372, pp. 418–432, 1981. DOI: 10.1016/0375-9474(81)90044-0.

[18] Moore, M., *Introduction to Scattering Theory*. Michigan State University, 2008, pp. 1–11, Last access: 25.04.2023. [Online]. Available: %7B%5Curl%7Bhttps://web.pa.msu.edu/people/mmoore/852scattering.pdf%7D%7D.

[19] Dreizler, R.M. Kirchner, T. and Lüdde, C.S., "Elastische Streuung: Stationäre Formulierung - Integralgleichungen", in *Streutheorie in der nichtrelativistischen Quantenmechanik: Eine Einführung*. Springer Berlin Heidelberg, 2018, pp. 53–78, ISBN: 978-3-662-57897-1. DOI: 10.1007/978-3-662-57897-1_2.

[20] Nolting, W., "Streutheorie", in *Grundkurs Theoretische Physik 5/2: Quantenmechanik - Methoden und Anwendungen*. Springer Berlin Heidelberg, 2012, pp. 321–381, ISBN: 978-3-642-24421-6. DOI: 10.1007/978-3-642-24421-6_5.

[21] Reinhardt, H., "25. Streutheorie", in *Band 2 Pfadintegralformulierung und Operatorformalismus*. Berlin, Boston: De Gruyter Oldenbourg, 2020, pp. 52–120, ISBN: 9783110586077. DOI: 10.1515/9783110586077-003.

[22] Dalitz, R.H., and Tuan, S.F., "The phenomenological representation of k-nucleon scattering and reaction amplitudes", *Ann. Phys.*, vol. 10, pp. 307–351, 1960. DOI: 10.1016/0003-4916(60)90001-4.

[23] Ross, M.H., and Shaw, G.L., "Scattering length and effective range theory for multichannel processes", *Ann. Phys.*, vol. 9, pp. 391–415, 1960. DOI: 10.1016/0003-4916(60)90040-3.

[24] Basu, D., Biswas, S. N., and Datta, K., "Complex $\bar{K}N$ Scattering Lengths and Current Algebra", *Phys. Rev.*, vol. 176, pp. 1835–1841, 1968. DOI: 10.1103/PhysRev.176.1835.

[25] Cieplý, A. et al., "On the pole content of coupled channels chiral approaches used for the $\bar{K}N$ system", *Nucl. Phys. A*, vol. 954, pp. 17–40, 2016. DOI: 10.1016/j.nuclphysa.2016.04.031.

[26] Weinberg, S., "Pion scattering lengths", *Phys. Rev. Lett.*, vol. 17, pp. 616–621, 1966. DOI: 10.1103/PhysRevLett.17.616.

[27] Tomozawa, Y., "Axial-Vector Coupling Constant Renormalization and the Meson-Baryon Scattering Lengths", *Nuovo Cim.*, vol. 46, pp. 707–717, 1966. DOI: 10.1007/BF02857517.

[28] Ikeda, Y., Hyodo, T. and Weise, W., "Chiral SU(3) theory of antikaon–nucleon interactions with improved threshold constraints", *Nucl. Phys. A*, vol. 881, pp. 98–114, 2012. DOI: 10.1016/j.nuclphysa.2012.01.029.

[29] Deser, S., Goldberger, M. L., Baumann, K., and Thirring, W., "Energy level displacements in pi-mesonic atoms", *Phys. Rev.*, vol. 96, pp. 774–776, 1954. DOI: 10.1103/PhysRev.96.774.

[30] Meißner, U.G., Raha, U. and Rusetsky, A., "Spectrum and decays of kaonic hydrogen", *Eur. Phys. J. C*, vol. 35, pp. 349–357, 2004. DOI: 10.1140/epjc/s2004-01859-4.

[31] Meißner, U.G., Raha, U. and Rusetsky, A., "Kaon–nucleon scattering lengths from kaonic deuterium experiments", *Eur. Phys. J. C*, vol. 47, pp. 473–480, 2006. DOI: 10.1140/epjc/s2006-02578-6.

[32] Miyahara, K., and Hyodo, T., "Structure of $\Lambda(1405)$ and construction of $\overline{K}N$ local potential based on chiral su(3) dynamics", *Phys. Rev. C*, vol. 93, p. 015 201, 2016. DOI: 10.1103/PhysRevC.93.015201.

[33] Hoshino, T. et al., "Constraining the $\overline{K}N$ interaction from the $1S$ level shift of kaonic deuterium", *Phys. Rev. C*, vol. 96, p. 045 204, 2017. DOI: 10.1103/PhysRevC.96.045204.

[34] Cieplý, A. and Smejkal, J., "Chirally motivated $\overline{K}N$ amplitudes for in-medium applications", *Nucl. Phys. A*, vol. 881, pp. 115–126, 2012. DOI: 10.1016/j.nuclphysa.2012.01.028.

[35] Mai, M. and Meißner, U.G., "Constraints on the chiral unitary $\overline{K}N$ amplitude from $\pi\Sigma K^+$ photoproduction data", *Europ. Phys. J. A: Hadrons and Nuclei*, vol. 51, p. 30, 2015. DOI: 10.1140/epja/i2015-15030-3.

[36] Feijoo, A. and Magas, V. and Ramos, A., "$S = -1$ meson-baryon interaction and the role of isospin filtering processes", *Phys. Rev. C*, vol. 99, p. 035 211, 2013. DOI: 10.1103/PhysRevC.99.035211.

[37] Guo, Z.H. and Oller, J. A., "Meson-baryon reactions with strangeness -1 within a chiral framework", *Phys. Rev. C*, vol. 87, p. 035 202, 2013. DOI: 10.1103/PhysRevC.87.035202.

[38] Cieplý, A., Hrtánková, J., Mareš, J. et al., "From K^-N interactions to K^--nuclear quasi-bound states", *AIP Conference Proceedings*, vol. 2249, p. 030 014, 2020. DOI: 10.1063/5.0008968.

[39] Dover, C.B., Hüfner, J. and Lemmer, R.H., "Pions in nuclear matter—an approach to the pion-nucleus optical potential", *Ann. Phys.*, vol. 66, pp. 248–292, 1971. DOI: 10.1016/0003-4916(71)90189-8.

[40] Bardeen, W.A. and Torigoe, E.W., "Strong-interaction effects in K-mesonic atoms", *Phys. Rev. C*, vol. 3, pp. 1785–1797, 1971. DOI: 10.1103/PhysRevC.3.1785.

[41] Gal, A., "On the Scattering Length of the K^-d System", *Int. J. Mod. Phys. A*, vol. 22, pp. 226–233, 2007. DOI: 10.1142/S0217751X07035379.

[42] Döring, M. and Meißner, U.G., "Kaon–nucleon scattering lengths from kaonic deuterium experiments revisited", *Phys. Lett. B*, vol. 704, pp. 663–666, 2011. DOI: 10.1016/j.physletb.2011.09.099.

[43] Shevchenko, N.V., "Near-threshold K^-d scattering and properties of kaonic deuterium", *Nucl. Phys. A*, vol. 890-891, pp. 50–61, 2012. DOI: 10.1016/j.nuclphysa.2012.07.010.

[44] Mizutani, T., "Faddeev-chiral unitary approach to the K^-d scattering length", *Phys. Rev. C*, vol. 87, p. 035 201, 2013. DOI: 10.1103/PhysRevC.87.035201.

[45] Liu, Z.-W. et al., "Kaonic hydrogen and deuterium in Hamiltonian effective field theory", *Phys. Lett. B*, vol. 808, p. 135 652, 2020. DOI: 10.1016/j.physletb.2020.135652.

[46] Biscari, C., and Sgamma, F., *Installation and Alignment of the DAΦNE Accelerators*, 1998. [Online]. Available: https://accelconf.web.cern.ch/e98/PAPERS/TUP08G.PDF.

[47] Raimondi, P., Shatilov, D. N. and Zobov, M., *Beam-Beam Issues for Colliding Schemes with Large Piwinski Angle and Crabbed Waist*, 2007. DOI: 10.48550/ARXIV.PHYSICS/0702033. [Online]. Available: https://arxiv.org/abs/physics/0702033.

[48] Milardi, C. et al., "Present Status of the DAΦNE Upgrade and Perspectives", *International Journal of Modern Physics A*, vol. 24, pp. 360–368, 2009. DOI: 10.1142/S0217751X09043687.

[49] Zobov, M. et al., "Test of "Crab-Waist" Collisions at the DAΦNE Φ Factory", *Phys. Rev. Lett.*, vol. 104, p. 174 801, 2010. DOI: 10.1103/PhysRevLett.104.174801.

[50] Zyla, P.A. et al. (Particle Data Group), *Prog. Theor. Exp. Phys.*, 2020, 083C01 (2020) and 2021 Update.

[51] Curceanu, C. et al., "The modern era of light kaonic atom experiments", *Rev. Mod. Phys.*, vol. 91, p. 025 006, 2019. DOI: 10.1103/RevModPhys.91.025006.

[52] Iwasaki, M. et al., "Observation of kaonic hydrogen K_α X rays", *Phys. Rev. Lett.*, vol. 78, pp. 3067–3069, 1997. DOI: 10.1103/PhysRevLett.78.3067.

[53] Davies, J.D. et al., "Observation of kaonic hydrogen atom X-rays", *Phys. Lett. B*, vol. 83, pp. 55–58, 1979. DOI: 10.1016/0370-2693(79)90887-6.

[54] Izycki, M. et al, "Results of the search forK-series X-rays from kaonic hydrogen", *Z Physik A*, vol. 297, pp. 11–15, 1980. DOI: 10.1007/BF01414238.

[55] Bird, P.M. et al., "Kaonic Hydrogen atom X-rays", *Nucl. Phys. A*, vol. 404, pp. 482–494, 1983. DOI: 10.1016/0375-9474(83)90272-5.

[56] Martin, A.D, "Kaon-nucleon parameters", *Nucl. Phys. B*, vol. 179, pp. 33–48, 1981. DOI: 10.1016/0550-3213(81)90247-9.

[57] Kim, J.K., "Low-Energy $K^- - p$ Interaction and Interpretation of the 1405-MeV $Y_0{}^*$ Resonance as a $\overline{K}N$ Bound State", *Phys. Rev. Lett.*, vol. 14, pp. 29–30, 1965. DOI: 10.1103/PhysRevLett.14.29.

[58] Sakitt, M. et al., "Low-Energy K^--Meson Interactions in Hydrogen", *Phys. Rev.*, vol. 139, B719–B728, 1965. DOI: 10.1103/PhysRev.139.B719.

[59] Wiegand, C.E. and Pehl, R.H., " Measurement of Kaonic X Rays from He-4", *Phys. Rev. Lett.*, vol. 27, pp. 1410–1412, 1971. DOI: 10.1103/PhysRevLett.27.1410.

[60] Batty, C.J. et al., "Measurement of kaonic and pionic X-rays from liquid helium", *Nucl. Phys. A*, vol. 326, pp. 455–462, 1979. DOI: 10.1016/0375-9474(79)90403-2.

[61] Baird, S. et al., "Measurements on Exotic Atoms of Helium", *Nucl. Phys. A*, vol. 392, pp. 297–310, 1983. DOI: 10.1016/0375-9474(83)90127-6.

[62] Batty, C.J., "Light kaonic and antiprotonic atoms", *Nucl. Phys. A*, vol. 508, pp. 89–98, 1990. DOI: 10.1016/0375-9474(90)90465-X.

[63] Hirenzaki, S. et al., "Chiral unitary model for the kaonic atom", *Phys. Rev. C*, vol. 61, p. 055 205, 2000. DOI: 10.1103/PhysRevC.61.055205.

[64] Okada, S. et al., "Precision measurement of the $3d \to 2p$ x-ray energy in kaonic ^{4}He", *Phys. Lett. B*, vol. 653, pp. 387–391, 2007. DOI: 10.1016/j.physletb.2007.08.032.

[65] Beer, G. et al., "Measurement of the Kaonic Hydrogen X-Ray Spectrum", *Phys. Rev. Lett.*, vol. 94, p. 212 302, 2005. DOI: \linebreak10.1103/PhysRevLett.94.212302.

[66] Bazzi, M. et al. (SIDDHARTA collaboration), "A new measurement of kaonic hydrogen X-rays", *Phys. Lett. B*, vol. 704, pp. 113–117, 2011. DOI: 10.1016/j.physletb.2011.09.011.

[67] Bazzi, M. et al. (SIDDHARTA collaboration), "First measurement of kaonic helium-3 X-rays", *Phys. Lett. B*, vol. 697, pp. 199–202, 2011. DOI: 10.1016/j.physletb.2011.02.001.

[68] Bazzi, M. et al. (SIDDHARTA collaboration), "Preliminary study of kaonic deuterium X-rays by the SIDDHARTA experiment at DAΦNE ", *Nucl. Phys. A*, vol. 907, pp. 69–77, 2013. DOI: 10.1016/j.nuclphysa.2013.03.001.

[69] Bazzi, M. et al. (SIDDHARTA collaboration), "K-series x-ray yield measurement of kaonic hydrogen atoms in a gaseous target", *Nucl. Phys. A*, vol. 954, pp. 7–16, 2016. DOI: 10.1016/j.nuclphysa.2016.03.047.

[70] Faber, M. et al., "Energy-level displacement of excited np states of kaonic deuterium in a Faddeev-equation approach", *Phys. Rev. C*, vol. 84, p. 064 314, 2011. DOI: 10.1103/PhysRevC.84.064314.

[71] Koike, T., Harada, T., and Akaishi, Y., "Cascade calculation of K^--p and K^--d atoms", *Phys. Rev. C*, vol. 53, pp. 79–87, 1996. DOI: 10.1103/PhysRevC.53.79.

[72] Capoccia, C., private communication.

[73] Skurzok, M. et al., "Characterization of the SIDDHARTA-2 luminosity monitor", *J. Inst.*, vol. 15, P10010, 2020. DOI: 10.1088/1748-0221/15/10/p10010.

[74] Weber, G., *X-Ray attenuation & absorption calculator*, https://web-docs.gsi.de/~stoe_exp/web_programs/x_ray_absorption/index.php.

[75] Jensen, T., "ATOMIC CASCADE IN KAONIC HYDROGEN AND DEUTERIUM", *DAFNE 2004: Physics at meson factories*, 2004. [Online]. Available: %7B%5Curl%7Bhttps://hal.science/hal-00003765/document%7D%7D.

[76] Pristauz-Telsnigg, D., private communication.

[77] Lechner, E. et al., "Silicon drift detectors for high count rate X-ray spectroscopy at room temperature", *Nucl. Instrum. Methods Phys. Res. A*, vol. 458, pp. 281–287, 2001. DOI: 10.1016/S0168-9002(00)00872-X.

[78] Gatti, E. and Rehak, P., "Semiconductor drift chamber — An application of a novel charge transport scheme", *Nucl. Instrum. Methods Phys. Res.*, vol. 225, pp. 608–614, 1984. DOI: 10.1016/0167-5087(84)90113-3.

[79] Lechner, E. et al., "Silicon drift detectors for high resolution room temperature X-ray spectroscopy", *Nucl. Instrum. Methods Phys. Res. A*, vol. 377, pp. 346–351, 1996. DOI: 10.1016/0168-9002(96)00210-0.

[80] Bertuccio, G. et al., "A Silicon Drift Detector-CMOS front-end system for high resolution X-ray spectroscopy up to room temperature", *J. Inst.*, vol. 10, P01002, 2015. DOI: 10.1088/1748-0221/10/01/p01002.

[81] Miliucci, M. et al., "Large area silicon drift detectors system for high precision timed x-ray spectroscopy", *Meas. Sci. Technol.*, vol. 33, 095502, 2022. DOI: 10.1088/1361-6501/ac777a.

[82] Quaglia, R. et al., "Development of arrays of Silicon Drift Detectors and readout ASIC for the SIDDHARTA experiment", *Nucl. Instrum. Methods Phys. Res. A*, vol. 824, pp. 449–451, 2016. DOI: 10.1088/1361-6501/ac777a.

[83] Bazzi, M. et al., "Characterization of the SIDDHARTA-2 second level trigger detector prototype based on scintillators coupled to a prism reflector light guide", *J. Inst.*, vol. 8, T11003, 2013. DOI: 10.1088/1748-0221/8/11/T11003.

[84] Vander Velde-Wilquet, C. et al., "Determination of the branching fractions for K^--meson absorptions at rest in carbon nuclei", *Nuov. Cim. A*, vol. 39, pp. 538–547, 1977. DOI: 10.1007/BF02771028.

[85] Vander Velde-Wilquet, C. et al., "K^--meson absorptions at rest in carbon nuclei leading to final states containing a Λ-hyperon", *Nuov. Cim. A*, vol. 38, pp. 178–190, 1977. DOI: 10.1007/BF02724540.

[86] Vander Velde-Wilquet, C. et al., "The conversion probability and emission ratio of charged Σ-hyperons following k^- meson capture at rest in carbon", *Nucl. Phys. A*, vol. 241, pp. 511–523, 1975. DOI: 10.1016/0375-9474(75)90401-7.

[87] Eljen Technology, *General Purpose Plastic Scintillator EJ-200, EJ-204, EJ-208, EJ-212*, Jul. 2021.

[88] AdvanSiD Advanced Silicon Detectors, *NUV SiPMs Chip Scale Package (CSP)*, version Rev. 9, May 2015, p. 2.

[89] Kingbright, *1.6X0.8mm SMD CHIP LED LAMP*, Rev. V.20B, May 2015.

[90] Renker, D., "Geiger-mode avalanche photodiodes, history, properties and problems", *Nucl. Instrum. Methods Phys. Res. A*, vol. 567, pp. 48–56, 2006. DOI: 10.1016/j.nima.2006.05.060.

[91] Piemonte, C., "Silicon Photomultipliers: Properties, Latest Developments at FBK and Applications.", *Microsc. Microanal.*, vol. 22, pp. 592–593, Suppl. 3 2016. DOI: 10.1017/S1431927616003810.

[92] Sauerzopf, C. et al., "Intelligent Front-end Electronics for Silicon photodetectors (IFES)", *Nucl. Instrum. Meth. Phys. Res. A*, vol. 819, pp. 163–166, 2016. DOI: 10.1016/j.nima.2016.02.098.

[93] Foyer, L., *Instructions to Program the SIDDHARTA-2 Amplification Boards*, 2022.

[94] Tüchler, M., "A Charged Particle Veto Detection System for Kaonic Deuterium Measurements at DAΦNE ", M.S. thesis, University of Vienna, 2019.

[95] Tüchler, M., Zmeskal, J. et al., "A charged particle veto detector for kaonic deuterium measurements at DAΦNE ", *IOP Conf. Series: Journal of Physics: Conf. Series*, vol. 1138, p. 012 012, 2018. DOI: 10.1088/1742-6596/1138/1/0120.

[96] Brun, R. and Rademakers, F., "ROOT - An object oriented data analysis framework", *Nucl. Instrum. Methods Phys. Res. A*, vol. 389, pp. 81–86, 1997. DOI: 10.1016/S0168-9002(97)00048-X.

[97] ROOT team, *ROOT: analyzing petabytes of data, scientifically.* https://root.cern/, Last access: 26.09.2022, 2021.

[98] Garutti, E. and Musienko, Y., "Radiation damage of SiPMs", *Nucl. Instrum. Methods Phys. Res. A*, vol. 926, pp. 69–84, 2019. DOI: 10.1016/j.nima.2018.10.191.

[99] Safari, M.J., "Differentiation method for Compton edge characterization in organic scintillation detectors", *Radiation Physics and Engineering*, vol. 1, pp. 9–16, 2020. DOI: 10.1088/1742-6596/1138/1/0120.

[100] Tsang, T. et al., "Neutron radiation damage and recovery studies of SiPMs", *J. Inst.*, vol. 11, P12002, 2016. DOI: 10.1088/1748-0221/11/12/P12002.

[101] Cargnelli, M., private communication.

[102] Keysight Technologies, *Keysight 81150A and 81160A Pulse Function Arbitrary Noise Generators*, Aug. 2018.

[103] Goto, S., "Response functions of a Si(Li) detector for photon energies from 1 to 10 keV", *Nucl. Instrum. Methods Phys. Res. A*, vol. 333, pp. 452–457, 1993. DOI: 10.1016/0168-9002(93)91191-O.

[104] Campbell, J.L. et al., "A quantitative explanation of low-energy tailing features of Si(Li) and Ge X-ray detectors, using synchrotron radiation", *Nucl. Instrum. Methods Phys. Res. A*, vol. 418, pp. 394–404, 1998. DOI: 10.1016/S0168-9002(98)00889-4.

[105] Maxwell, J.A., Teesdale, W.J. and Campbell, J.L., "Compensation schemes for peak-tailing uncertainties in PIXE spectra, using the GUPIX code", *Nucl. Instrum. Methods Phys. Res. B*, vol. 94, pp. 172–179, 1994. DOI: 10.1016/0168-583X(94)95671-5.

[106] Campbell, J.L., "X-ray spectrometers for PIXE", *Nucl. Instrum. Methods Phys. Res. B*, vol. 49, pp. 115–125, 1990. DOI: 10.1016/0168-583X(90)90227-L.

[107] Campbell, J.L. et al., "Analytic fitting of monoenergetic peaks from Si(Li) x-ray spectrometers", *Nucl. Instrum. Methods Phys. Res. B*, vol. 9, pp. 71–79, 1985. DOI: 10.1016/0168-583X(85)90780-3.

[108] Leo, W.R., *Techniques for Nuclear and Particle Physics Experiments, A How-to Approach*. Springer-Verlag Berlin Heidelberg New York, 1994, pp. 118–119, ISBN: 3-540-57280-5.

[109] Kortright, J. and Thompson, A.C., *X-Ray Data Booklet*, Lawrence Berkeley National Laboratory, Third edition, Sep. 2009.

[110] Sgaramella, F., "The SIDDHARTA-2 calibration method for high precision kaonic atoms x-ray spectroscopy measurements", *Phys. Scr.*, vol. 97, p. 114 002, 2022. DOI: 10.1088/1402-4896/ac95da.

[111] Miliucci, M., "Silicon drift detectors system for high-precision light kaonic atoms spectroscopy", *Meas. Sci. Technol.*, vol. 32, p. 095 501, 2021. DOI: 10.1088/1361-6501/abeea9.

[112] Bernardini, C. et al., "Lifetime and Beam Size in a Storage Ring", *Phys. Rev. Lett.*, vol. 10, pp. 407–409, 1963. DOI: 10.1103/PhysRevLett.10.407.

[113] Santos, J.P. et al., "X-ray energies of circular transitions and electron screening in kaonic atoms", *Phys. Rev. A*, vol. 71, p. 032 501, 2005. DOI: 10.1103/PhysRevA.71.032501.

[114] Koike, T., private communication.

[115] Okada, S., private communication.

[116] Sirghi, D. et al., "A new kaonic helium measurement in gas by SIDDHARTINO at the DAΦNE collider", *J. Phys. G: Nucl. Part. Phys*, vol. 49, p. 055 106, 2022. DOI: 10.1088/1361-6471/ac5dac.

[117] Akaisihi, Y., "Kaonic helium atoms in relation to kaonic nuclear bound states", *Proceedings of EXA*, 45–53, 2005.

[118] Batty, C.J. et al., "Measurement of kaonic X-rays from Li, LiH AND Be", *Nucl. Phys. A*, vol. 282, pp. 487–492, 1977. DOI: 10.1016/0375-9474(77)90072-0.

[119] Backenstoss, G. et al., "K- mass and K- polarizability from kaonic atoms", *Phys. Lett. B*, vol. 43, pp. 431–436, 1973. DOI: 10.1016/0370-2693(73)90391-2.

[120] Backenstoss, G. et al., "Intensities and strong interaction attenuation of kaonic X-rays", *Nucl. Phys. B*, vol. 73, pp. 189–201, 1974. DOI: 10.1016/0550-3213(74)90014-5.

[121] Batty, C.J. et al., "Measurement of strong interaction effects in kaonic atoms", *Nucl. Phys. A*, vol. 329, pp. 407–428, 1979. DOI: 10.1016/0375-9474(79)90384-1.

[122] Barnes, P.D. et al., "Measurement of kaonic X-rays from Al, Si, Ni and Cu", *Nucl. Phys. A*, vol. 231, pp. 477–492, 1974. DOI: 10.1016/0375-9474(74)90511-9.

[123] Wiegand, C.E. and Godfrey, G.L., "Measurements of x rays and γ rays from stopped kaons", *Phys. Rev. A*, vol. 9, p. 2282, 1974. DOI: 10.1103/PhysRevA.9.2282.

[124] Kunselman, R., "Kaon mass measurement from kaonic atom x-ray energies; the 4f-3d kaonic transition in chlorine", *Phys. Lett. B*, vol. 34, pp. 485–487, 1971. DOI: 10.1016/0370-2693(71)90660-5.

[125] Kunselman, R., "Negative - kaon mass", *Phys. Rev. C*, vol. 9, p. 2469, 1974. DOI: 10.1103/PhysRevC.9.2469.

[126] Batty, C. et al., "Nuclear quadrupole deformation effects on pionic and kaonic X-rays", *Nucl. Phys. A*, vol. 355, pp. 383–402, 1981. DOI: 10.1016/0375-9474(81)90534-0.

[127] Cheng, S.C. et al., "K- mass from kaonic atoms", *Nucl. Phys. A*, vol. 254, pp. 381–395, 1975. DOI: 10.1016/0375-9474(75)90224-9.

[128] Batty, C.J., Friedman, E., and Gal, A., "Strong interaction physics from hadronic atoms", *Physics Reports*, vol. 287, pp. 385–445, 1997. DOI: 10.1016/S0370-1573(97)00011-2.

[129] Sgaramella, F., Tüchler, M. et al., "Measurements of high-n transitions in intermediate-mass kaonic atoms by SIDDHARTA-2 at DAΦNE ", *Eur. Phys. J. A*, vol. 59, p. 56, 2023.

[130] Pilkuhn, H., and Schlaile, H.G., "Tables of vacuum polarization of excited states of light mesic atoms", *Z. Phys. D - Atoms, Molecules and Clusters*, vol. 15, pp. 321–325, 1990. DOI: 10.1007/BF01437175.

[131] Karshenboim, S. G., Korzinin, E. Y., and Ivanov, V. G., "The Uehling correction to the energy levels in a pionic atom", *Can. J. Phys.*, vol. 84, pp. 107–113, 2006. DOI: 10.1139/P06-010.

[132] Karshenboim, S., Ivanov, V. and Korzinin, E., "Vacuum polarization in muonic atoms: the Lamb shift at low and medium", *Z. Eur. Phys. J. D*, vol. 39, pp. 351–358, 2006. DOI: 10.1140/epjd/e2006-00133-0.

[133] Koike, T., and Akaishi, Y., "Stark mixing in the exotic helium atom cascade process", *Nucl. Phys. A*, vol. 639, p. 521, 1998. DOI: 10.1016/S0375-9474(98)00320-0.

[134] Wycech, S., and Loiseau, B., "An Advantage of "Upper Levels"", *Acta Phys. Polon. B*, vol. 51, p. 109, 2020. DOI: 10.5506/APhysPolB.51.109.

[135] Friedman, E, Gal, A. and Hrtánková, J., "Studies of kaonic atoms and nuclei", *AIP Conference Proceedings*, vol. 2130, p. 020 013, 2019. DOI: 10.1063/1.5118381.

[136] Iliescu, M. and Sirghi, D., private communication.

[137] Napolitano, F., private communication.

[138] Wilks, S.S., "The Large-Sample Distribution of the Likelihood Ratio for Testing Composite Hypotheses", *Ann. Math. Statist.*, vol. 9, pp. 60–62, 1938. DOI: 10.1214/aoms/1177732360.

[139] Sherazi, T.A., *Ultrahigh Molecular Weight Polyethylene*. Springer Berlin Heidelberg, 2014. DOI: 10.1007/978-3-642-40872-4_591-2.

[140] Broadcom, *AFBR-S4N44C013 NUV-HD Single Silicon Photo Multiplier Data Sheet*, Jan. 2022.

[141] Curceanu, C. et al., "Kaonic Atoms Measurements at DAΦNE: SIDDHARTA-2 and Future Perspectives", *Few-Body Syst.*, vol. 62, p. 83, 2021. DOI: 10.1007/s00601-021-01666-5.

[142] Curceanu, C. et al., "Fundamental physics at the strangeness frontier at DAΦNE. Outline of a proposal for future measurements.", Apr. 2021. DOI: arXiv:2104.06076v2.

[143] Schneider, H., private communication.